EFFICIENT SAMPLING IN STOCHASTIC BIOLOGICAL MODELS

by

Rory Donovan-Maiye

M.S., University of Washington, 2005

B.A., Reed College, 2004

Submitted to the Graduate Faculty of

the Department of Computational Biology in partial fulfillment

of the requirements for the degree of

Doctor of Philosophy

University of Pittsburgh

2016

UNIVERSITY OF PITTSBURGH

SCHOOL OF MEDICINE

This dissertation was presented

by

Rory Donovan-Maiye

It was defended on

May 31, 2016

and approved by

Daniel Zuckerman, Department of Computational and Systems Biology

James Faeder, Department of Computational and Systems Biology

Jeremy Berg, Department of Computational and Systems Biology

Christopher Langmead, Computational Biology Department, CMU

John Woolford, Biology Department, CMU

Dissertation Director: Daniel Zuckerman, Department of Computational and Systems Biology

EFFICIENT SAMPLING IN STOCHASTIC BIOLOGICAL MODELS

Rory Donovan-Maiye, PhD

University of Pittsburgh, 2016

Even when the underlying dynamics are known, studying the emergent behavior of stochastic biological systems *in silico* can be computationally intractable, due to the difficulty of comprehensively sampling these models. This thesis presents the study of two techniques for efficiently sampling models of complex biological systems. First, the weighted ensemble enhanced sampling technique is adapted for use in sampling chemical kinetics simulations, as well as spatially resolved stochastic reaction-diffusion kinetics. The technique is shown to scale to large, cell-scale simulations, and to accelerate the sampling of observables by orders of magnitude in some cases. Second, I study the free energy estimates of peptides and proteins using Markov random fields. These graphical models are constructed from physics-based forcefields, uniformly sampled at different densities in dihedral angle space, and free energy estimates are computed using loopy belief propagation. The effect of sample density on the free energy estimates provided by loopy belief propagation is assessed, and it is found that in most cases a modest increase in sample density leads to significant improvement in convergence. Additionally, the approximate free energies from loopy belief propagation are compared to statistically exact computations and are confirmed to be both accurate and orders of magnitude faster than traditional methods in the models assessed.

TABLE OF CONTENTS

LIST OF FIGURES

1.0 INTRODUCTION

A common dilemma one faces in constructing computational models of biological systems is a trade-off between model complexity and the tractability of simulating or sampling said model. While there is merit in keeping models as simple as possible, when one is interested in studying multi-scale behavior in complex systems, it is not always obvious which model ingredients are essential and which are superfluous. As data accumulation accelerates, model ingredients proliferate, and larger, more complete models of biological systems become possible to construct at multiple scales, it behooves us to concern ourselves with how to sample ever larger models.

This dissertation focusses on this question in two different settings: the cellular scale and the molecular scale. In the first chapter I study how the weighted ensemble methodology can accelerate the sampling of rare events in stochastic chemical kinetics models. In the second chapter I examine how the same formalism can aid in sampling spatially resolved cellular simulations. The third chapter departs from the cellular scale to focus on molecular systems, and there I examine how sampling density affects the accuracy of loopy belief propagation free energy estimates of peptides and proteins.

1.1 WEIGHTED ENSEMBLE IN NON-SPATIAL SYSTEMS

My coworkers and I applied the "weighted ensemble" resampling technique to stochastic chemical kinetics systems biology models. Using the weighted ensemble framework, we were able to observe rare events with orders of magnitude greater precision than a brute-force approach, and were able to out-preform the state of the art technique (wSSA) on models of anything greater than trivial complexity [1].

Stochastic behavior is an essential facet of biological processes such as mRNA expression, protein expression, and epigenetic processes [2, 3, 4, 5, 6, 7, 8, 9, 10, 11, 12, 13, 14, 15]. Stochastic chemical kinetics simulations are often used to study systems biology models of such processes [16, 17, 18]. One of the more common stochastic approaches, and the one employed in the present study, is the stochastic simulation algorithm (SSA), also known as the Gillespie algorithm [19, 20, 16].

As stochastic systems biology models approach the true complexity of the systems being modeled, it quickly becomes intractable to investigate rare behaviors using naïve ("brute-force") simulation approaches. By their very nature, rare events occur infrequently; confoundingly, rare events are often those of most interest. For example, the switching of a bistable system from one state to another may happen so infrequently that running a stochastic simulation long enough to see transitions is (extremely) computationally prohibitive [21]. This impediment only grows as model complexity increases, and as such it poses a serious hurdle for systems models as they grow more intricate.

Several approaches to speeding up the simulation of rare events in stochastic chemical kinetic systems exist. A variety of "leaping" methods can, by taking advantage of approximate time-scale separation, accelerate the SSA itself [22, 23, 24, 25, 26, 27, 28, 29]. Kuwahara and Mura's weighted stochastic simulation (wSSA) method [30] was refined by Gillespie and Petzold et al. [31, 32, 33, 34], and is based on importance sampling. The forward flux sampling method of ten Wolde et al. [21, 35, 36, 37] uses a series of interfaces in state-space to reduce computational effort, as does the non-equilibrium umbrella sampling approach [38, 39].

Rare event sampling is also an active topic in the field of molecular dynamics simulations, and many approaches have been proposed. Of the approaches that do not irreversibly modify the free energy landscape of the system, some notable methods include dynamic importance sampling [40], milestoning [41], transition path sampling [42], transition interface sampling [43], forward flux sampling [37], non-equilibrium umbrella sampling [39], and weighted ensemble sampling [44, 45, 46, 47, 48, 49, 50, 51]. For a summary of these methods, see [52]. Many of the ideas behind these techniques are not exclusive to molecular dynamics simulations, and can be adapted to studying stochastic chemical kinetic models. For example, dynamic importance sampling seems to be closely related to wSSA.

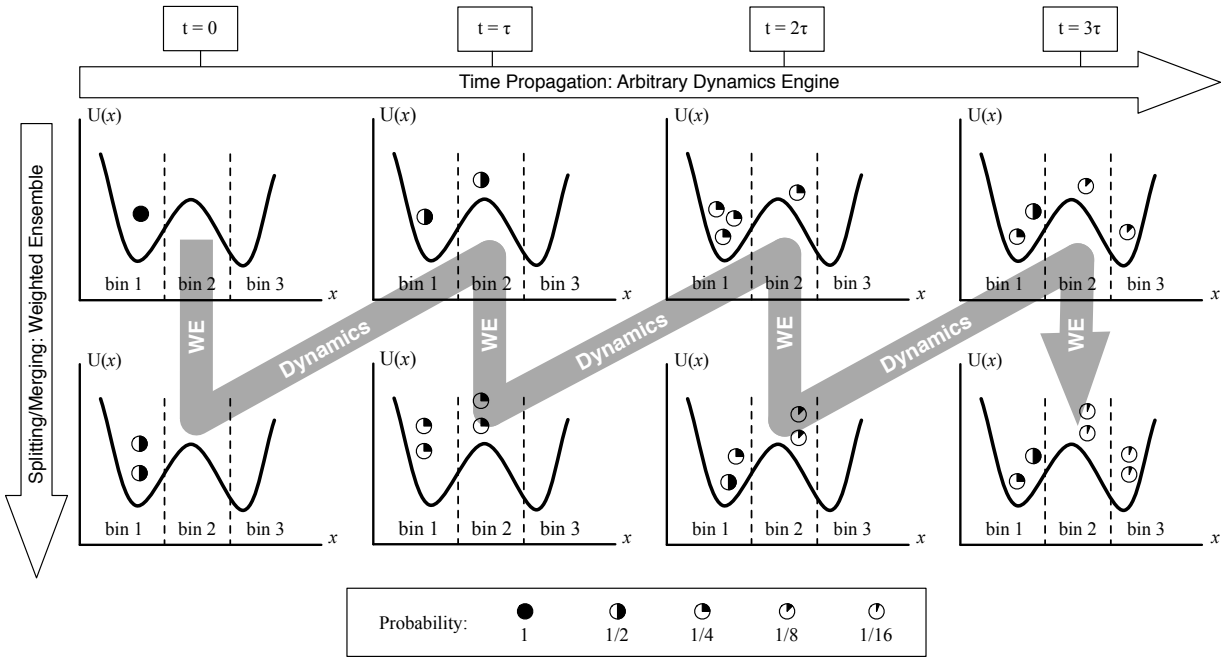

Figure 1: Weighted ensemble (WE) simulation depicted for a configuration/state-space divided into bins. Multiple trajectories are run using any dynamics software (here we use the SSA in BioNetGen) and checked every τ for bin location. Trajectories are assigned weights (symbols – see legend) that sum to one and are split and combined according to statistical rules that preserve unbiased kinetic behavior.

Because of its relative simplicity of implementation, and promise for sampling rare events, we applied one of these methods, the weighted ensemble algorithm (WE) to well-established model systems of stochastic kinetic chemical reactions. These models range in complexity from one species and two reactions, to 354 species and 3680 reactions. For the systems studied, WE proves many orders of magnitude faster than SSA simulation alone, offers linear parallel scaling, returns full distributions of desired species at arbitrary times, and can yield mean first passage times (MFPTs) via the setup of a feedback steady-state.

WE's strategy of statistical natural selection or statistical ratcheting is schematized in Fig. 1. First, the space is divided/classified into non-overlapping "bins" which are typically static, although dynamic and adaptive tessellations are possible [46]. A target number of trajectories, M_{targ}, is set for each bin. Multiple trajectories are initiated and each is assigned a weight so that the sum of weights is one. Trajectories are then simulated independently according to the desired dynamics (e.g., molecular dynamics or SSA) and checked intermittently (every τ units of time) for their location. If a trajectory of weight w is found to occupy a previously unoccupied bin, that trajectory is replicated to obtain the target number of copies, M_{targ}, for the bin. Daughter trajectories' weights are set to w/M_{targ}, to sum to the weight of the parent trajectory. If a bin is occupied by more than the target number, trajectories must be pruned in a statistical fashion maintaining the sum of weights. Specifically, the two lowest weight trajectories are "merged" by randomly selecting one of them to survive, with probability proportional to their weights, and the surviving trajectory absorbs the weight of the pruned one. This process is repeated as needed, and maintains an exact statistical representation of the evolving distribution of trajectories [46].

In particular, we applied the weighted ensemble (WE) [44, 45, 46, 47, 48, 49, 50, 51] approach to systems-biology models of stochastic chemical kinetics equations, implemented in BioNetGen [18, 53]. Increases in computational efficiency on the order of 10^{20} were attained for a simple system of biological relevance (the enzymatic futile cycle), and on the order of 10^{12} for a large systems-biology model (FcεRI), with 354 species and 3680 reactions. An example of our results is illustrated in Fig. 8.

The weighted ensemble approach is easy to understand and implement, statistically exact [46], and easy to parallelize. It can yield long-timescale information such as mean first passage times (MFPTs) from simulations of much shorter length, and offers perfect (linear) parallel scaling. It

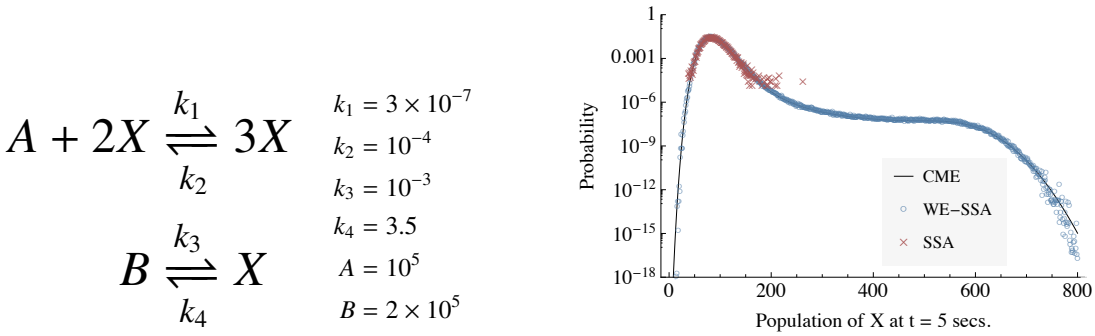

(a) (b)

Figure 2: (a) The Schlögl reactions. (b) The probability distribution of X in the Schlögl system, at $t = 5$ seconds, when initialized from a delta function at $X = 82$. The exact solution from the chemical master equation is compared to data obtained using the SSA in a weighted ensemble run (WE-SSA), and to ordinary SSA, when each is given equal computational time.

appears that WE holds significant promise as a tool for the investigation of complex stochastic systems.

1.2 WEIGHTED ENSEMBLE IN SPATIAL SYSTEMS

I continued to investigate the utility of applying the weighted ensemble method to stochastic biological models by integrating it with the MCell simulation package. Because MCell models chemical reactions with explicit spatial resolution, and hence diffusion plays a role in reaction rates, the potential speed-up over brute force in characterizing rare events is even greater than before, yielding efficiency gains of hundreds of dozens of magnitude over brute force in toy models.

To explore the utility of weighted ensemble sampling, I investigated three MCell systems, the simplest of which was a toy model of binding and diffusion, containing (on the order of) thousands of molecules, shown in Fig. 3.

The efficiency gains of weighted ensemble in this context are not restricted to only toy mod-

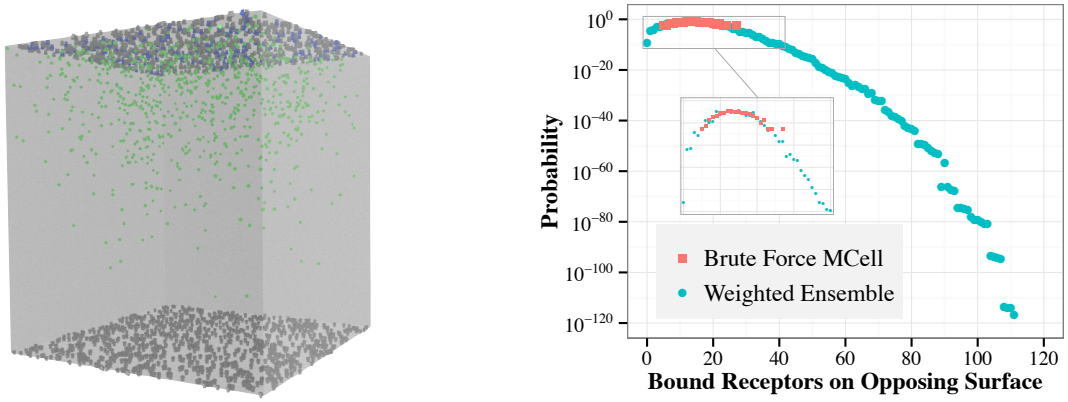

(a) (b)

Figure 3: (a) Toy MCell model, in which ligands are initially bound to receptors at top, and are free to unbind and diffuse to bind at the bottom. (b) The probability density for the number of ligands bound to receptors at the bottom after 1/100 of a second. Both weighted ensemble and brute force sampling are given equal computational time.

els. To demonstrate the utility of the approach in complex systems, we collaborated with Markus Dittrich and Jun Ma on sampling their model of the frog neuromuscular junction, which contains hundreds of thousands of molecules. In experimentally relevant low calcium regimes, sampling the output of their model is difficult, because millions of brute force simulations are needed to see a handful of successful synaptotagmin vesicle releases. This model posed some challenges for us, because the rate constants in the dynamics are not in fact constant, and are changed over time to simulate an action potential. Nevertheless, we were able to demonstrate the utility of weighted ensemble sampling sampling for the model, and it proved to be a useful exploration of how well weighted ensemble sampling performs in adverse conditions.

To assess the confounding effects of time-dependent rate constants from size of the model, I also applied the weighted ensemble approach to sampling a similarly large model with simpler dynamics. The Faeder lab, the Murphy lab, and the MCell developers have constructed a pipeline for generating three dimensional cellular models of biochemical signaling. The model I investigated employs hundreds of thousands of diffusing molecules and hundreds of different biochemical reactions to model signal transduction from the extracellular matrix to the nucleus. Besides being a convenient system for demonstrating the ability of weighted ensemble sampling to scale to very large systems, integrating WE into this modeling pipeline provides a crucial aid in sampling the incredible complex and taxing simulations that result from such detailed three-dimensional models.

1.3 STUDYING THE EFFECTS OF SAMPLING DENSITY IN GRAPHICAL MODELS OF PEPTIDES AND PROTEINS

Over the past decade, the foundational work of Langmead and coworkers has established the use of graphical models as key tools in the computational study of protein structure [54, 55, 56, 57, 58, 59, 60, 61]. Inspired by that work, the last chapter of my thesis is a departure from the weighted ensemble formalism applied and cellular-scale models of the first two chapters; instead, I focus on molecular scale phenomena: the free energies of biomolecules such as peptides and proteins. While the scale and methodology I investigate changes significantly, the underlying theme remains

the same, that of efficient sampling of complex biological systems.

Estimating free energies is crucial to accurately characterizing binding affinities; unfortunately, these estimates require immense computational effort using traditional simulation-based approaches such as molecular dynamics [62, 63]. Kamisetty et al. [54, 57] demonstrated the ability of graphical models (specifically, using loopy belief propagation on Markov random fields) to predict accurate binding free energies using orders of magnitude less computation than simulation-based methods. Prior work by Kamisetty et al. also provided bounds on the error in the free energies due to the approximate nature of the belief propagation algorithm on graphs containing loops [55].

Motivated by these impressive results, I take a close look at the behavior of BP estimates of the free energy of peptides and proteins as the state space of the model becomes more densely sampled. While there is much prior work on the accuracy of loopy belief propagation, both in the general context of loopy graphs [64, 65, 66, 67] and in the particular domain of graphs of proteins [55], that work focuses on the relative performance of BP to exact methods on fixed Markov random fields. Here, I examine how the BP estimates of free energy change as the state-space of the Markov random fields more densely sample the configurational space of the underlying physics. In the examples I investigate, I find that even a modest increase in the sampling density of the side-chain dihedral degrees of freedom appears to help the free energy estimate converge to a stable value.

The performance of loopy belief propagation has been found to be startlingly good in a variety of settings, but there are few guarantees of its accuracy in arbitrarily connected and parameterized Markov random fields [68, 67]. As noted above, useful bounds on the error due to belief propagation can be obtained to constrain the worst-case performance of BP [55]. Since I generate Markov random fields from scratch using a forcefield and states of my choosing, I also take the opportunity to assess the accuracy of BP methods by comparing them to statistically exact free energy estimates. Neither this opportunity nor the idea of making such a comparison is unique to my study, and it may not be surprising that in the models I investigate, I find that BP is a very accurate approximation even though it has no guarantee to be so, as it has proven to be for many other models. Nevertheless, since a skeptic would demand that the accuracy of BP estimates be verified in some manner, I do so by performing comparisons to standard free energy methods, with the thought that this specific methodology might prove useful in communicating the utility of BP

methods to an audience more familiar with the physical sciences literature, and less familiar with the computer science and machine learning literature.

Finally, I note some of the important caveats to the work I present in Chapter 4. While the BP calculations complete in a matter of seconds, the comparison to traditional free-energy estimates such as polymer growth is so computationally intense (requiring days to weeks of computation) that the models I consider are somewhat limited in size and scope. An additional constraint on the size of the models I investigate is that the constructions of the graphs themselves becomes a bottleneck as the sampling of state-space becomes dense. Although I do use a fully atomic representation of the peptides and proteins, I employ only a simple dielectric solvent model. I also only consider side-chain dihedral degrees of freedom as variables in the model; notably, this freezes out the flexibility of the backbone, and thus global conformational changes in the structure. While these are strong limitations, working within such constraints allows me to quantify the effect that the state-space sampling density has on these models, while maintaining a rigorous comparison of the BP results to exact methods.

Below, I provide an introduction to Markov random fields for those unfamiliar with their formalism, though the reader is encouraged to consult the many excellent books that do a far more thorough job of explaining the subject [69, 70, 71, 72]. The work of Langmead and coworkers is also a valuable expository resource on this topic [54, 55, 56, 57, 58, 59, 60, 61].

1.3.1 Introduction to discrete Markov random fields

Pairwise discrete Markov random fields are undirected graphs whose nodes can take on a discrete number of states, and which interact with each other in a pairwise fashion via potential functions on the edges in the graph. In the context of peptides and proteins, a Markov random field can be constructed by mapping each residue in the structure to be a node in the graph. Each node takes on a finite set of conformational states, and edges in the graph capture the relevant interactions between the states each residue can take. An example of such a graph is shown in Fig. 4.

Markov random fields are a subclass of graphical models that are of particular relevance in structural biology [54, 57]. Since Markov random fields (MRFs) were introduced as a generalization of the Ising model [73], perhaps looking at a simple Ising model formulated as a Markov

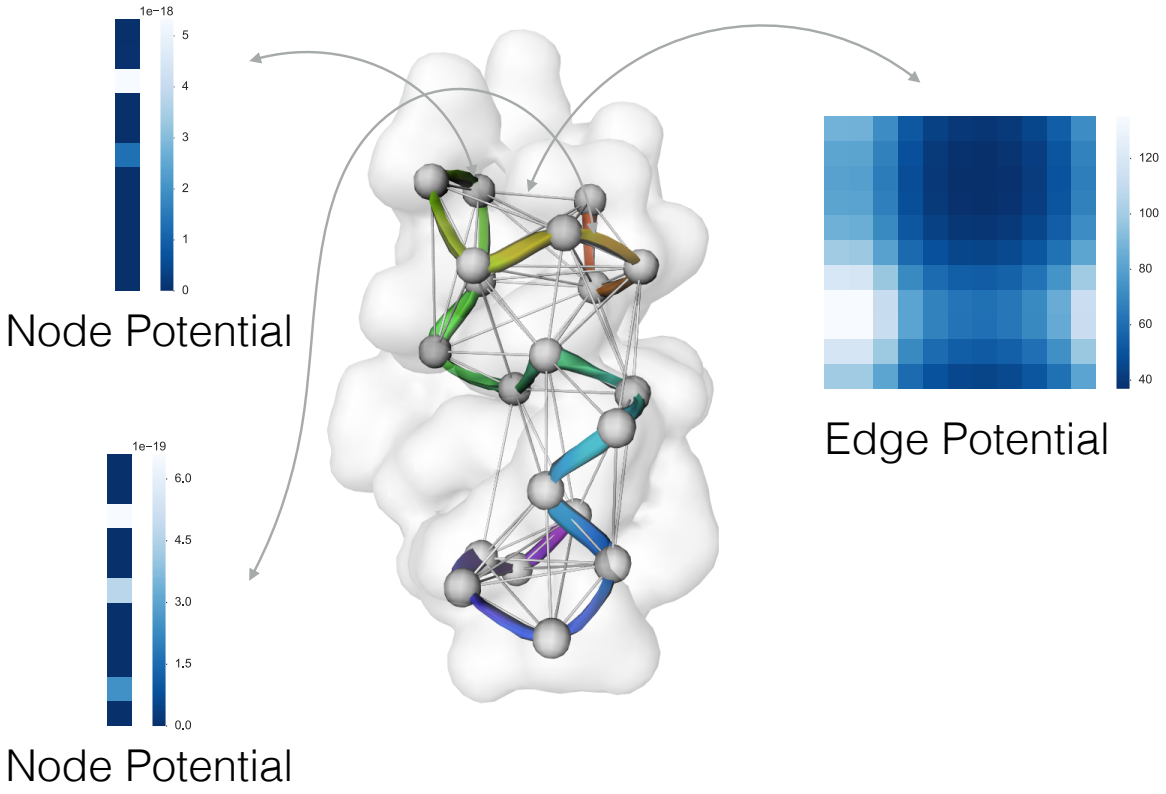

Figure 4: An example of a graph induced on an atomic model of a peptide. The graph is constructed from a PDB structure, using a cutoff distance to determine which edges are included. The nodes and edges are then populated with potential functions, indexing the single (nodes) and pairwise (edges) preferences for the nodes to be in particular states. Using nodes that have 11 states each, one example of an edge potential is shown, along with the node potentials for the nodes it connects. The potentials are dimensionless numbers which depend exponentially on the energy of the system, while the different orders of magnitude in the node and edge potentials reflect that in this case, the intra-residue energies of the node potentials are much stronger that the inter-residue interactions of characterized by the edge potential. While not shown, each edge and node would similarly possess such potential functions.

random field would be a good introduction to how the formalism works.

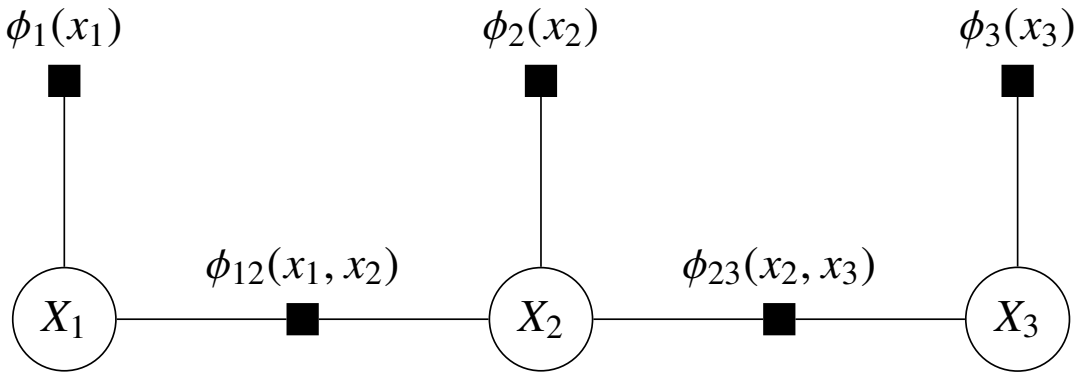

Figure 5: Factor graph representation of a Markov random field for an Ising model with three sites in an external magnetic field. Variables are in circles, and factors are black squares.

The graph in Fig. 5 consists of two types of nodes: variables, which can take on different values (circles) and factors, which are functions of the variables (squares). In this type of graph, variables only connect to factors and vice versa. The factors are functions of any variable that they are connected to, and the probability of the system to be in a specific state is proportional to the product of all the factors in the graph:

$$P = \frac{1}{Z}\prod_{ij}\phi_{ij}(x_i, x_j)\prod_{k}\phi_k(x_k) = \frac{1}{Z}\phi_{12}(x_1, x_2)\phi_{23}(x_2, x_3)\phi_1(x_1)\phi_2(x_2)\phi_3(x_3) \tag{1.1}$$

In an Ising model, where each variable is a spin that can be either "up" or "down", the values for all of the variables x_i can be either $\{-1, 1\}$. The factors tell us how the states of the individual variables combine to affect the disposition of the system to be in a certain global configuration. The factors that connect to only one node, $\phi_i(x_i) = e^{mx_i/kT}$, represents the coupling of individual spins to the external magnetic field, and are also known as "node potentials". The factors that connect two neighboring nodes, $\phi_{ij}(x_i, x_j) = e^{Jx_ix_j/kT}$ represents the coupling of neighboring spins, and are known as "edge potentials".

The normalization constant, or partition function in equation 1.1 is a sum over every possible configuration of the system:

$$Z = \sum_{x}\prod_{ij}\phi_{ij}(x_i, x_j)\prod_{k}\phi_k(x_k) = \sum_{x_i\in\{-1,1\}}\phi_{12}(x_1, x_2)\phi_{23}(x_2, x_3)\phi_1(x_1)\phi_2(x_2)\phi_3(x_3) \tag{1.2}$$

It is this sum that is often of interest, due to its deep connection to the free energy of the system, but it is usually extremely difficult to compute. As we will see, belief propagation offers an attractive approximation to this sum which can be computed efficiently.

In theory, many nodes can be connected to one factor, if we wished to encode a complicated interaction that displays no underlying structure. In practice, we will allow a factor to connect to at most two nodes; MRFs following this restriction are known as pairwise Markov random fields. I will employ pairwise MRFs exclusively in my work.

One of the great utilities of representing a probability distribution as a pairwise Markov random field is that it permits a visual intuition of statistical properties such as covariance and independence. As a reminder, we usually say that two variables are statistically independent if and only if $P(A, B) = P(A)P(B)$; that is, the value of A is unaffected by the value of B. Inspecting the above Ising model we see that none of the variables are statistically independent: the ϕ_{ij} terms do not allow any such factorization. Even though X_1 and X_3 are not directly coupled, their behavior is correlated because they are both coupled to X_2.

The graphical representation of the distribution allows us to take advantage of *conditional* independencies in the distribution. All variables do not co-vary equally – there is something fundamentally different about the interaction between X_1 and X_2, and between X_1 and X_3. X_1 and X_3 do not directly interact; X_2 separates them. In fact if we know the value of X_2, then the values of X_1 and X_3 are no longer correlated, that is, the values of X_1 and X_3 are independent, conditioned on the value of X_2. This is a general property of Markov random fields, that there is a subset of the graph that we can condition on (or "know the value of") that would render two nodes that are not directly connected statistically independent, or disconnected. In a pairwise MRF, two nodes are conditionally independent if there is no factor, or edge, connecting them.

Additionally, graphical models let us encode the distribution of states of the system more efficiently. Naïvely, to tabulate the energetics of the system, we would need a table that is the size of the number of values a variable can take (say, k), raised to the number of variables (say, N), i.e k^N, which in our example is 2^3. Instead, given the structure of the graph, with E edges and N nodes, we can use E tables of size k^2 and N tables of size k to store the possible states of the network. In a small graph such as our three node example, this "efficient encoding" is actually worse, but as the size of the graph increases, and the number of states a variable can take increases, the efficiency

gain scales exponentially. For instance, the gain for an Ising chain of length 10 is about a factor of 10, and for length 100 is a factor of about 10^{27}. The formalism I've described for the Ising chain generalizes straightforwardly to arbitrarily connected graphs where each node in the graph takes on one of a certain set of discrete values.

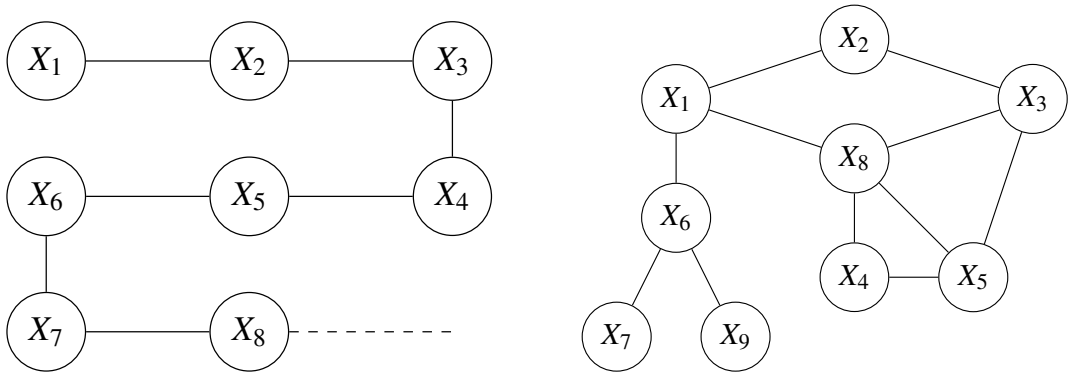

Figure 6: More complicated graphs for pairwise Markov random fields. (a) Ising chain Markov random field with N sites. Variables are in circles, with node potentials implied. Edge-potential factors are implied to be along the edges that are present. (b) Arbitrarily connected Markov random field. Variables are in circles, with node potentials implied. Edge-potential factors are implied to exist along the edges that are present.

One of the most computationally taxing aspects of using graphical models is computing the normalization constant, or partition function Z, in equation 1.2. For example, in an Ising model with 100 nodes, a naïve computation of the partition function entails a sum over 2^{100} terms. Due to this exponential scaling, for any but a small class of simple graphs an exact calculation is computationally intractable. However, approximation schemes exist that run in reasonable times and often yield results that are quite close to the exact computation.

In particular, an approximation known as loopy belief propagation can quickly produce approximations to the partition function that are startlingly good [64, 74]. As discussed above, for arbitrary MRFs, loopy belief propagation is not guaranteed to converge to an answer, and even if it does, that answer is not guaranteed to be within a given tolerance of the exact result.

2.0 WEIGHTED ENSEMBLE IN NON-SPATIAL SYSTEMS

2.1 INTRODUCTION

As discussed in Chapter 1, there is significant interest in accelerating the sampling of stochastic systems biology models. There are many approaches to this challenging problem, ranging from methods that accelerate the dynamics themselves using approximations [22, 23, 24, 25, 26, 27, 28, 29], to importance sampling methods [30, 31, 32, 33, 34], to forward flux-based methods and umbrella sampling methods[21, 35, 36, 37, 75, 76, 39, 38].

The approach we take here, of weighted ensemble sampling, originally found application in the field of structural biology simulation [44, 45, 46, 47, 48, 49, 50, 51], and is most similar in spirit to the forward flux forward flux sampling [37] and non-equilibrium umbrella sampling [39] methods, though many related approaches exist [40, 41, 42, 43].

The weighted ensemble approach distinguishes itself in its combination of relative simplicity and potential flexibility in sampling rare events. Here we apply it to study rare events in model systems of stochastic kinetic chemical reactions. These models range in complexity from one species and two reactions, to 354 species and 3680 reactions. For the systems studied, WE proves many orders of magnitude faster than SSA simulation alone, offers linear parallel scaling, returns full distributions of desired species at arbitrary times, and can yield mean first passage times (MFPTs) via the setup of a feedback steady-state.

2.2 METHODOLOGY

The methods employed are described immediately below, while the models are specified in Sec. 2.3.

2.2.1 Stochastic Chemical Kinetics & BioNetGen

Stochastic chemical kinetics occupies a middle-ground in the realm of chemical simulation, between very explicit, and costly, molecular dynamics (MD) simulations and the deterministic formalism of reaction rate equations (RRE). Stochastic chemical kinetics attempts to account for the randomness inherent in chemical reactions, without trying to explicitly model the spatial structure of the reacting species. It is many orders of magnitude faster than MD simulations, but much slower than the RRE approach. It is an ideal method to use for modeling the effects of low concentrations (or copy numbers) of chemical reactants, while ignoring the effects of specific spatial distribution.

Stochastic chemical kinetics models can be solved exactly for sufficiently simple systems using the Chemical Master Equation (CME), and approximately (for all systems) using Gillespie's direct stochastic simulation algorithm (SSA) [19, 20, 16]. The SSA samples the CME exact solution by modeling stochastic chemical kinetics in a straightforward manner, and yields trajectories of species concentrations that converge to the RRE method in the limit of large amounts of reactants. In brief, the SSA iteratively and stochastically determines which reaction fires at what time by sampling from the exponential distribution of waiting times between reactions. For a detailed explanation of the SSA, see [16].

We employ the rule-based modeling and simulation package BioNetGen [53] to simulate both our toy and complex models. Rule-based modeling languages allow the specification of biochemical networks based on molecular interactions. Rules that describe those interactions can be used to generate a reaction network that can be simulated either as RREs or using the SSA, or the rules can be used directly to drive stochastic chemical kinetics simulations. BioNetGen has been applied to a variety of systems, such as the aggregation of membrane proteins by cytosolic cross-linkers in the LAT-Grb2-SOS1 system [77], the single-cell quantification of IL-2 response by effector and

regulatory T cells [78], the analysis and verification of the HMGB1 signaling pathway [79], the role of scaffold number in yeast signaling systems [80], and the analysis of the roles of Lyn and Fyn in early events in B cell antigen receptor signaling [81]. We employ BioNetGen's implementation of the direct SSA to propagate the dynamics in our systems.

2.2.2 Weighted Ensemble (WE)

WE is a general-purpose protocol used in molecular dynamics simulations [45, 46, 47, 49, 50, 51] that we adapt here to the efficient sampling of dynamics generated by chemical kinetic models. In brief, WE employs a strategy of "statistical natural selection" using quasi-independent parallel simulations which are coupled by the intermittent exchange of information. The intermittency leads directly to linear parallel scaling. Importantly, the simulations are coupled via configuration space (essentially the "phase space" of the system in physics language or the "state-space" in cell and population modeling). This type of coupling permits both efficiency and a large degree of scale independence. The efficiency results from distributing trajectories to typically under-sampled parts of the space, while scale independence is afforded because every type of system has a configuration or state-space.

WE's strategy of statistical natural selection or statistical ratcheting is schematized in Fig. 1. A detailed heuristic description of the algorithm is provided in Chapter 1, while pseudocode is listed below. It is worth emphasizing that the iterative resampling upon which the algorithm is based is statistically exact, guaranteeing an unbiased estimate of the probability distributions for a broad class of stochastic processes [46].

The weighted ensemble algorithm can be outlined fairly concisely. Let M_{targ} be the target number of segments in each bin, N_{bins} the number of bins, whose geometry are defined by the grid G_{grid}, τ the time-step of an iteration of WE, and N_{iters} the total number of iterations of WE. The WE procedure also requires an initial state of the system, $\mathbf{x}_0$, which in our case is a list of the concentrations of all the chemical species in the system.

procedure WE($N_{\text{iters}}, \tau, G_{\text{grid}}, M_{\text{targ}}, \mathbf{x}_0$)
  for $i = 1 \ldots N_{\text{iters}}$ **do**
    for each populated bin in G_{grid} **do**

propagate dynamics for all trajectories

update bin populations

for each bin in G_{grid} **do**

if bin population = 0 or M_{targ} **then**

do nothing

else if bin population < M_{targ} **then**

replicate trajectories until bin pop. = M_{targ}

maintain sum of weights in each bin

else if bin population > M_{targ} **then**

merge trajectories until bin pop. = M_{targ}

maintain sum of weights in each bin

save coordinates and weights of each trajectory

return trajectory coordinates & weights for each iter.

The replicating and merging of trajectories in the above algorithm are done randomly, according to the weight of each trajectory segment in a given bin, which has been shown not to bias the dynamics of the ensemble [44, 47].

Setting up a WE simulation requires selection of state-space binning, trajectory multiplicity, and timing parameters. In our simulations, we chose to divide the state-space of an N-dimensional system into one- or two-dimensional regular grids of non-overlapping bins. It is possible to use non-Cartesian bins, and to adaptively change the bins during simulation [46, 49], but for simplicity we did not pursue any such optimization. Specific parameter choices for each model are given in Sec. 2.3.

When WE is used to manage an ensemble of trajectories, there are two time-scales of immediate concern: the period at which trajectory coordinates are saved, and the period τ at which ensemble operations are performed. These two time-scales can be different, but for simplicity we set them to be the same, and select τ such that it is greater than the inverse of the average event firing rate for the SSA. When we refer to the time-step, or iteration of a process, we are referring to the τ of Fig. 1.

WE can be employed in a variety of modes to address different questions. Originally developed

to monitor the time evolution of arbitrary initial probability distributions [44], i.e. non-stationary non-equilibrium systems, WE was generalized to efficiently simulate both equilibrium and non-equilibrium steady-states [47]. In steady-state mode, mean first passage times (MFPTs) can be estimated rapidly based on simulations much shorter than the MFPT using a simple rigorous relation between the flux and MFPT [47]. Steady-states can be attained rapidly, avoiding long relaxation times, by using the inter-bin rates computed during a simulation to estimate bin probabilities appropriate to the desired steady-state; trajectories are then reweighted to conform to the steady-state bin probabilities [47]. Both of these methods are described in more detail below.

2.2.2.1 Basic WE: Probability Distribution Evolving in Time Perhaps the simplest use of a weighted ensemble of trajectories is to better sample rare states as a system evolves in time, specifically the states corresponding to extreme values of the binning coordinate. The SSA itself samples the exact distribution, but its sampling is concentrated about the mode(s) of the distribution. The SSA naturally – and correctly – samples rare states infrequently. By using WE to split up the state-space, however, one can resample the distribution at every time step τ, selecting those trajectories that advance along a progress coordinate for more detailed study, but doing so without applying any forces or biasing the trajectories or the distribution. Essentially, WE appropriates much of the effort that brute-force SSA devotes to sampling the central component of the distribution, repurposing it to obtain better estimates of the tails.

This basic use of WE requires none of the "tricks" we apply in later sections, such as using reweighting techniques to accelerate obtaining a steady-state. We apply basic WE to some of our systems – particularly, but not exclusively, to those that are not bistable.

2.2.2.2 Steady-State The mean first passage time (MFPT) from state A to state B is a key observable. It is equal to the inverse of the flux (of probability density) from state A to state B in steady-state [82],

$$\mathrm{MFPT}_{A\to B} = \frac{1}{\mathrm{Flux}_{ss}(A \to B)} \,. \tag{2.1}$$

This relation provides the weighted ensemble approach the ability to calculate MFPTs in a straightforward manner. During a WE run, when any trajectories (and their associated weights) reach a designated target area of state-space (or "state B"), they are removed and placed back in the initial

state ("state A"). Eventually, such a process will result in a steady-state flow of probability from state A to state B that does not change in time (other than with stochastic noise).

Reweighting. The waiting time to obtain a steady-state constrains the efficiency of obtaining a MFPT by measuring fluxes via equation 2.1. This waiting time can vary from the relatively short time scale of intra-state equilibration for simple systems, to much longer time-scales, on the order of the MFPT itself for more complicated systems. To reduce this waiting time, we use the steady-state reweighting procedure of Bhatt et al. [47]. This method measures the fluxes between bins to obtain a rate-matrix for transitions between bins, and uses a Markov formulation to infer a steady-state distribution from the (noisy) data available.

For instance, let $\{w_i\}$ be the set of bin weights (i.e the sum of the weights of the trajectories in each bin), and let $\{w_i^{ss}\}$ be the set of steady-state values of the bin weights. If f_{ij} is the flux of weight into bin i from bin j, then in steady-state, since the flux out of a bin is equal to the flux into it,

$$\frac{\mathrm{d}w_i^{ss}}{\mathrm{d}t} = \sum_j \left(f_{ij}^{ss} - f_{ji}^{ss}\right) = \sum_j \left(k_{ij}w_j^{ss} - k_{ji}w_i^{ss}\right) = 0\ . \tag{2.2}$$

Since the flux of weight into bin i from bin j is the product of a (constant) rate and the (current) weight in a bin, i.e. $f_{ij} = k_{ij}\, w_j$ (true for both steady state and not), we can use Eq. 2.2 to find the inter-bin rates. By measuring the inter-bin fluxes and the bin weights, we can approximately infer the transition rates, and then find a set of weights that satisfy Eq. 2.2. Once the set of bin weights is found, the weights of the individual trajectories in the bins are rescaled commensurately. This reweighting process should not be confused with a resampling process (such as basic WE splitting and merging) which does not change the distribution.

The steady-state distribution of weights thus inferred is not necessarily the true steady-state of the system, but tends to be closer to it than the distribution was prior to reweighting, and an iterative application of this procedure can converge to the true distribution fairly rapidly. In practice it has been shown to accelerate the system's evolution to a true steady-state by orders of magnitude in some cases [47].

2.2.3 Estimation of Computational Efficiency

Since it is important to assess new approaches quantitatively, we compare the speedup in computing time from weighted ensemble to a brute-force simulation, (i.e. SSA). For a given observable (e.g., the fraction of probability in a specified tail of the distribution) and a desired precision, we estimate the efficiency using the ratio:

$$E := \frac{\text{dynamics time in brute-force SSA}}{\text{dynamics time in WE-SSA}} \tag{2.3}$$

Since both WE and brute-force use the same dynamics engine/software, we can estimate the speedup of WE over brute-force by just keeping track of how much total "dynamics time" was simulated in each. We employ this measure when estimating the advantage of using WE to investigate the tails of probability distributions, as well as for finding MFPTs in bistable systems.

Another measure of efficiency we employ for MFPT estimation gauges how fast WE attains a result that is within 50% of the true result (determined from exact or extensive brute-force calculation):

$$E_{50\%} := \frac{\text{dynamics time in brute-force SSA to get } \pm 50\% \text{ exact}}{\text{dynamics time in WE-SSA to get } \pm 50\% \text{ exact}} . \tag{2.4}$$

This is an assessment of how well WE can extract rough estimates of long time-scale behavior from simulations that are much shorter than those timescales.

Brute-force SSA simulations can be run for long times without seeing a transition from one macro-state to another. To take account of the brute-force simulations where no transitions occurred we use a maximum likelihood estimator for the transition time, based on an exponential distribution of waiting times [83], which is a valid approximation for the one-dimensional and two-state systems studied below:

$$\begin{aligned} \mu_{MLE} &= \left(1 - \frac{n}{N}\right) T + \frac{1}{n} \sum_{i=1}^{n} t_i \\ \sigma_{\mu} &= \frac{\mu_{MLE}}{\sqrt{n}} \end{aligned} \tag{2.5}$$

where T is the length of the brute-force simulations, N is the number of these simulations performed, n is the number of these simulations in which a transition from one state to another is observed, and t_i are the times at which the transition is observed.

2.2.4 Limitations of Our Implementation

We used two different implementations of the weighted ensemble framework: WESTPA, written in Python, is the most feature-rich and stable [51], which will be available at http://chong.chem.pitt.edu/WESTPA. Another, written by Bin Zhang [45] and modified by us, is written in C, and is faster though less robust, and is available at http://donovanr.github.com/WE_git_code.

Weighted ensemble (WE), as a scripting-level approach, inherently adds some unavoidable overhead to the runtime of the dynamics. This overhead, in theory, is quite minimal: stopping, starting, merging, and splitting trajectories are not computationally costly operations. A key issue in practical implementations, though, is how long the algorithm actually takes to run, i.e the wall-clock running-time for dynamics (here, the SSA).

In practice, overhead can be significant for very simple systems, for the sole reason that reading and writing to disk takes so much time compared to how long it takes to run the dynamics of small models. In our implementation, data is passed from the dynamics engine to WE by reading and writing files to disk. This handicap is an artifact of our interface, which could, with minimal work, be modified to something more efficient. As a proof-of-principle, the version of WE written in C was modified, for the Schlögl reactions and the futile cycle, to contain hard-coded versions of the Gillespie direct algorithm for those systems, so as to obviate the I/O between WE and BNG. With these modifications, it was difficult to ascertain any significant overhead costs at all, and our runs completed in a matter of seconds. We also note that as model complexity increases and more time is devoted to dynamics, the overhead problem becomes negligible. Practical applications of WE will, by nature, target models where dynamics are expensive, rather than toy models, where they are cheap.

2.3 MODELS & RESULTS

We study four different models, ranging in complexity from two chemical reactions governing one chemical species, to 3680 reactions governing 354 species. The models we employ are coupled stochastic chemical reactions, which we implement and simulate in BioNetGen using the SSA [19,

20, 16]. As depicted in Fig. 1, these simulations are, in turn, managed by a weighted ensemble procedure.

2.3.1 Enzymatic Futile Cycle

2.3.1.1 Model The enzymatic futile cycle is a simple and robust model that can, in certain parameter regimes, exhibit qualitatively different behavior due to stochastic noise [84, 85]. This signaling motif can be seen in biological systems including GTPase cycles, MAPK cascades, and glucose mobilization [84, 86, 87].

The enzymatic futile cycle studied here is modeled by:

$$\begin{aligned} E_1 + S_1 &\underset{k_f}{\overset{k_f}{\rightleftharpoons}} B_1 \xrightarrow{k_s} E_1 + S_2 \\ E_2 + S_2 &\underset{k_f}{\overset{k_f}{\rightleftharpoons}} B_2 \xrightarrow{k_s} E_2 + S_1 \end{aligned} \tag{2.6}$$

where $k_f = 1.0$ and $k_s = 0.1$. Here S_1 can bind to its enzyme E_1, and in the bound form, B_1, (i.e. $B_1 = E_1 \cdot S_1$), it can be converted to S_2, and then dissociate (and similarly for $S_2 \to S_1$). The total amount of substrate, $S_1 + S_2$, is conserved, as are the amounts of the different enzymes E_1 and E_2, of which is supplied only one of each kind, thus $(S_1 + B_1) + (S_2 + B_2) = 100$. Following Kuwahara and Mura [30], in the specific system we look at, we set $S_1 + S_2 = 100$ and $E_1 + B_1 = E_2 + B_2 = 1$.

Thus constrained, the above system of reactions can be solved by an approximately 400-state chemical master equation (CME), to obtain an exact probability density for all times when initialized from an arbitrary starting point. We start the system at $S_1 = S_2 = 50$ and $E_1 = E_2 = 1$, and are interested in the probability distribution of S_1 after 100 seconds, that is, $P(S_1 = x, t = 100)$.

2.3.1.2 WE Parameters The WE data was generated using 101 bins of unit width on the coordinate S_1. We employed 100 trajectory segments per bin that were run for 100 iterations of a $\tau = 1$ s time-step, with no reweighting events. The brute-force data is from 10,200 100-second runs, which is an equivalent amount of dynamics to compute as the single WE run, if all the bins were full all the time. However, since the bins take some time to fill up, the WE run employed only 840,000 one-second segments, which makes the comparison to brute-force SSA more than fair.

2.3.1.3 Results Fig. 7 shows that the brute-force SSA is unable to sample values of S_1 much outside the range $30 < S_1 < 70$, whereas the WE method is able to accurately sample the entire distribution. Waiting for the brute-force approach to sample the tails would take $\sim 1/P(\text{tail}) \sim 1/10^{-23} \sim 10^{23}$ brute-force runs. With a conservative estimate of $\sim 10^4$ runs per second, it would take $\sim 10^{19}$ seconds, or many times the age of the universe, for brute-force SSA to sample the tails at all. WE takes 2–3 seconds to sample them (note the comparison to exact distribution provided by the CME), for an approximate efficiency increase $E \sim 10^{18}$.

For the sake of clarity, error-bars were omitted from Fig. 7. Over most of the data range, the error is too small to see on the plot. In the tails (of both SSA and WE-SSA) the error is not computable from a single run, since there are plot points comprised of only a single trajectory. The error in the estimate of the distribution can be inferred visually from the data's departure from the CME exact solution. For SSA, however, generating uncertainties far all values is essentially impossible. When computing quantitative observables reported below, we employ multiple independent runs to procure standard errors in our estimate.

From the distribution, we are able to read off useful statistics. For instance, in the spirit of Kuwahara and Mura [30], and Petzold and Gillespie et al. [31], one might desire to know the probability of the futile cycle to have a value of $S_1 > 90$ at $\Delta t = 100$, which we will denote as $p_{>90}$. Since WE gives an accurate estimate of $P(x,t)$ on an arbitrarily precise spatio-temporal grid, all that is required to find $p_{>90}$ is to sum up the area under the state of interest: we find $p_{>90} = 2.47 \times 10^{-18} \pm 3.4 \times 10^{-19}$ at one standard error, as computed from ten replicates of the single WE run plotted in Fig. 7. The CME gives an exact value of 2.72×10^{-18}. Following Gillespie et al. in [31], the approximate number of normal SSA runs needed to estimate this observable with comparable error is $n^{\text{SSA}}_{p_{>90}} = p_{>90}/(\sigma_{p_{>90}})^2 = 2.72 \times 10^{-18}/(3.4 \times 10^{-19})^2 = 2.4 \times 10^{19}$ SSA runs. Using ten replicate runs, WE is able to sample it using a total of 8,317,000 trajectory segments, which is computationally equivalent to 83,170 brute-force trajectories, resulting in an increase in sampling efficiency by a factor of $E \sim 2.4 \times 10^{19}/83,170 \sim 3 \times 10^{14}$ for this observable at this level of accuracy.

Since WE gives the full distribution, from the same data we can also find other rare event statistics. For example, we might also wish to compute the probability that $S_1 \leq 25$ at $\Delta t = 100$, which we will call $p_{\leq 25}$. From the same data described in the preceding paragraph, we can find

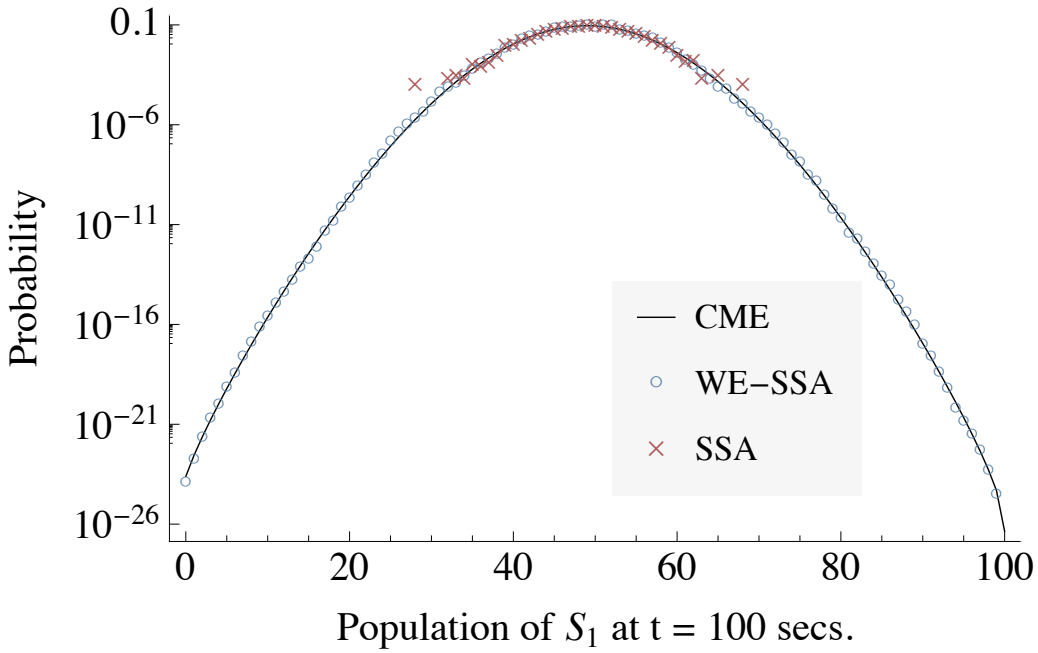

Figure 7: The probability distribution of S_1 in the Enzymatic Futile Cycle System, after $t = 100$ seconds, when initialized from a delta function at $S_1 = 50$, $E_1 = E_2 = 1$ at $t = 0$. The exact solution, procured via the chemical master equation (CME), is compared to data obtained using the SSA in a weighted ensemble run (WE-SSA), and to ordinary SSA, when each are given equal computation time. WE data is from a single run. Error bars are not plotted; for a discussion of uncertainties, see Sec. 2.3.1.3. The noise in the tail of the SSA points and gap in coverage is indicative of the high variance of SSA for rare events.

$p_{\leq 25} = 1.35 \times 10^{-7} \pm 1.5 \times 10^{-8}$ at one standard error. The CME gives an exact value of 1.26×10^{-7}. Again, estimating the number of SSA runs necessary to determine the same observable with similar accuracy as in [31], we find $n^{\mathrm{SSA}}_{p_{\leq 25}} = p_{\leq 25}/(\sigma_{p_{\leq 25}})^2 = 1.26 \times 10^{-7}/(1.5 \times 10^{-8})^2 = 6.0 \times 10^8$ SSA runs. Our weighted ensemble calculation used the computational equivalent of 83,170 brute-force trajectories, resulting in an increase in sampling efficiency by a factor of $E \sim 6.0 \times 10^8/83,170 \sim 7 \times 10^3$ for this observable at this level of accuracy.

Kuwahara and Mura [30], and Petzold and Gillespie et al. [31] define a quantity closely related to those computed above: the probability of a system to pass from one state to another in a certain time: $P(x_i \rightarrow x_f|\Delta t)$ [30, 31, 32, 33, 34]. This is subtly different than just measuring areas under a distribution, since a trajectory is terminated, and removed from the ensemble, if it successfully reaches the target. To make a direct comparison to this statistic, we implemented in WE an absorbing boundary condition at the target state $S_1 = 25$. Using ten WE runs, we find that the probability of reaching the $S_1 = 25$ within 100 seconds, which we call $p_{\mathrm{abs}(25)}$, is $1.61 \times 10^{-7} \pm 1.93 \times 10^{-8}$ at one standard error. The CME with an absorbing boundary condition at $S_1 = 25$ gives an exact value of 1.738×10^{-7}. As above, we estimate the number of brute-force SSA runs needed to attain a comparable estimate as $n^{\mathrm{SSA}}_{p_{\mathrm{abs}(25)}} = p_{\mathrm{abs}(25)}/(\sigma_{p_{\mathrm{abs}(25)}})^2 = 1.738 \times 10^{-7}/(1.93 \times 10^{-8})^2 = 4.66 \times 10^8$ SSA runs. In total, the ten WE runs used 6,342,600 trajectory segments, which is computationally equivalent to 63,426 brute-force trajectories. This yields an increase in efficiency of $E \sim 4.66 \times 10^8/63,426 \sim 7 \times 10^3$ for this observable at this level of accuracy.

For the above statistic, Gillespie et al. report an efficiency gain of 7.76×10^5 over brute-force SSA[31]. Direct comparisons of efficiency gain between wSSA and WE are difficult, even when focussing on the same observable in the same system. Many factors contribute to this, notably that WE is not optimized in a target-specific manner, as wSSA historically has been. Further, in its simplest form, WE yields a full space/time distribution of trajectories, from which it is possible to calculate rare event statistics for arbitrary states, which need not be specified in advance.

2.3.2 Schlögl Reactions

2.3.2.1 Model The Schlögl reactions are a classic toy-model for benchmarking stochastic simulations of bistable systems [88, 89, 90]. They are two coupled reactions with one dynamic species,

X:

$$A + 2X \underset{k_2}{\overset{k_1}{\rightleftharpoons}} 3X$$
$$B \underset{k_4}{\overset{k_3}{\rightleftharpoons}} X \tag{2.7}$$

where $k_1 = 3 \times 10^{-7}$, $k_2 = 10^{-4}$, $k_3 = 10^{-3}$, $k_4 = 3.5$, $A = 10^5$, and $B = 2 \times 10^5$. The species A and B are assumed to be in abundance, and are held constant. Both the mean first passage times and the time-evolution of arbitrary probability distributions can be computed exactly [89].

2.3.2.2 WE Parameters The WE data in Fig. 8 was generated using 802 bins of unit width, 100 trajectory segments per bin, a time-step $\tau = 0.05$ s, and run for 100 iterations of that time-step, with no reweighting events. The brute-force data is from 80,200 5-second runs, which is an equivalent amount of dynamics as a single WE run, if all bins are always full. Were that the case, the WE run would compute dynamics for 8,020,000 trajectory segments; in our case the WE simulation ran 7,047,300 trajectory segments, which makes the comparison to brute-force more than fair.

The WE data in Fig. 9 was generated using 80 bins of width 10, with 32 trajectory segments per bin, a time-step $\tau = 0.1$ s, run for 500 iterations of that time-step. Reweighting events (see Sec. 2.2.2.2) were applied every 100, 5, and 2 iterations for the data labeled "RW-100", "RW-5", and "RW-2", respectively.

2.3.2.3 Results Fig. 8 shows how the results of both a brute-force (BF) approach, and the WE approach compare to the exact solution [89], when each employs the same amount of dynamics time. We start the Schlögl system with $X = 82$, i.e. the PDF is initially a delta function at $X = 82$. To investigate rare transitions, we study the PDF at time $t = 5$ s. WE is able to accurately sample almost the entire distributions, even over the potential barrier near $X = 250$, while the BF approach is limited to sampling only high probability states. The Schlögl system is bistable, with states centered at $X = 82$ and $X = 563$, and a potential barrier between them, peaked at $X = 256$. The brute-force approach is unable to accurately sample values outside of the initial state, and cannot detect bistability in the model.

For the sake of clarity, error-bars were omitted from Fig. 8. Over most of the data range, the error is too small to see on the plot. In the tails (of both SSA and WE-SSA) the error is not

computable from a single run, since there are plot points comprised of only a single trajectory. Multiple runs are consistent with the data shown. The error in the estimate of the distribution can be inferred visually from the data's departure from the CME exact solution. When computing quantitative observables below, we employ multiple independent runs to procure standard errors in our estimate.

WE yields the full, unbiased probability distribution, but we again examine an observable in the spirit of that investigated by Petzold, Gillespie, and coworkers[30, 31, 32, 33, 34], i.e. the probability that the progress coordinate is beyond a certain threshold at a specified time, which is a simple summation of the distribution over the state of interest. From ten replicates of the Schlögl run plotted in Fig. 8, the probability that $X \geq 700$ at $t = 5$ seconds, i.e. $P(X \geq 700,\ t = 5\ \text{s})$, which we call $p_{\geq 700}$, is $1.143 \times 10^{-9} \pm 4.7 \times 10^{-11}$ at one standard error. The CME exact value is 1.148×10^{-9}. Following [31], we can estimate the number of brute-force SSA runs that would be needed to find $p_{\geq 700}$ at a similar level of accuracy as $n^{\text{SSA}}_{p_{\geq 700}} = p_{\geq 700}/(\sigma_{p_{\geq 700}})^2 = 1.148 \times 10^{-9}/(4.7 \times 10^{-11})^2 = 5.3 \times 10^{11}$ SSA runs. We can then estimate an improvement in efficiency of using WE over brute-force of $E \sim 5.3 \times 10^{11}/802,000 \sim 7 \times 10^5$ for this observable at this level of accuracy.

We also estimate the mean first passage time (MFPT) of the Schlögl system, which can be computed exactly [89]. Weighted ensemble can estimate the MFPT using Eq. 2.1 when the system is put into a steady-state. For the run that was reweighted every 100 iterations, Fig. 9 shows the WE estimates of the flux from the initial state ($X = 82$) to the final state ($X \geq 563$) converge to the exact value in about 100 iterations of weighted ensemble splittings and mergings, which is when the system relaxes from its delta-function initialization to a steady-state. The attainment of steady-state is accelerated by more frequent reweighting (see Sec. 2.2.2.2 on reweighting), as is shown in Fig. 9 in the runs that are reweighted every 2 and 5 iterations. These more frequently reweighted runs yield fluxes close to the exact value within about 30 iterations.

To quantify WE's improvement over brute-force in the estimate of the MFPT, we use the measure $E_{50\%}$ defined in Sec. 2.2.3. A brute-force estimate of the MFPT would require, optimistically, computing an amount of dynamics on the order of the MFPT itself (approximately 5×10^4 seconds). Since transitions in this system follow an exponential distribution, the standard deviation of the first passage times is equal to the mean of them. WE's estimate of the MFPT is within 50%

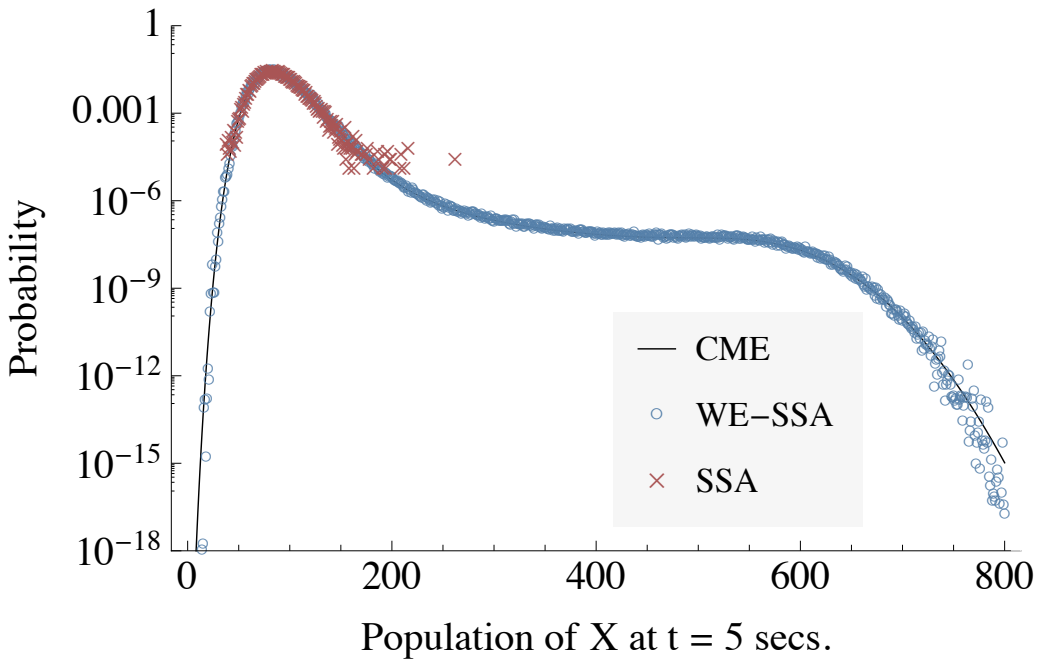

Figure 8: The probability distribution of X in the Schlögl system, at $t = 5$ seconds, when initialized from a delta function at $X = 82$. The exact solution from the chemical master equation is compared to data obtained using the SSA in a weighted ensemble run (WE-SSA), and to ordinary SSA. WE data is from a single run. For a discussion of uncertainties, see Sec. 2.3.2.3. The noise in the tail of the SSA points and gap in coverage is indicative of the high variance of SSA for rare events.

of the exact value after about 30 iterations of WE simulation, at which point about 1100 trajectory segments have been propagated, which is equivalent to propagating about 110 seconds of brute-force dynamics. Thus we find $E_{50\%} \sim 5 \times 10^4/110 \approx 500$. As can be seen in Fig. 9, this value is about a 3–5 fold increase over the WE results when reweighting very infrequently (every 100 iterations).

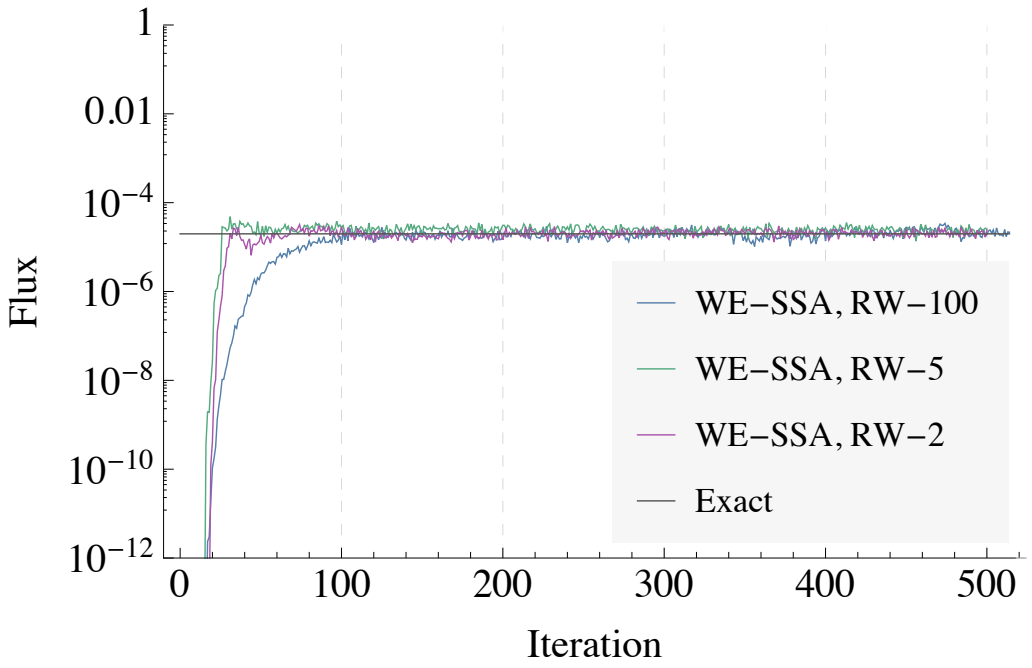

Figure 9: The flux of probability into the target state ($X \geq 563$) for the Schlögl system. The exact value is compared to WE results, for reweighting periods of every 100, 5, and 2 iterations. The inverse of the flux gives the mean first passage time by Eq. 2.1.

2.3.3 Yeast Polarization

To extend our comparison to existing methods, we also implemented and benchmarked against a modified yeast polarization model. This system has been previously studied using different variants of wSSA [32, 34], and presents an opportunity to compare performance gains over brute-force on a small-to-medium sized reaction network of non-trivial complexity.

2.3.3.1 Model This modified yeast polarization model[32] consists of six dynamical species (note that in the reactions below, L never changes) and eight reactions:

$$\begin{aligned}
\mathrm{R}_1: &\quad \varnothing \xrightarrow{k_1} R, && k_1 = 0.0038 \\
\mathrm{R}_2: &\quad R \xrightarrow{k_2} \varnothing, && k_2 = 0.0004 \\
\mathrm{R}_3: &\quad R + L \xrightarrow{k_3} RL + L, && k_3 = 0.042 \\
\mathrm{R}_4: &\quad RL \xrightarrow{k_4} R, && k_4 = 0.010 \\
\mathrm{R}_5: &\quad RL + G \xrightarrow{k_5} G_a + G_{bg}, && k_5 = 0.011 \\
\mathrm{R}_6: &\quad G_a \xrightarrow{k_6} G_d, && k_6 = 0.100 \\
\mathrm{R}_7: &\quad G_{bg} + G_d \xrightarrow{k_7} G, && k_7 = 1050 \\
\mathrm{R}_8: &\quad \varnothing \xrightarrow{k_8} RL, && k_8 = 3.21
\end{aligned} \tag{2.8}$$

All reaction propensities are in numbers of particles per second. The system is initialized at $t = 0$ with species counts $[R, L, RL, G, G_a, G_{bg}, G_d] = [50, 2, 0, 50, 0, 0, 0]$. That is, we start with 50 molecules each of R and G, and 2 of L, and no others.

This system does not reach equilibrium[32]; additionally, the rare event measured has no well-defined states, but is merely a measure of an unusually fast accumulation of G_{bg}.

2.3.3.2 WE Parameters The rare event statistics presented below were measured using 50 bins on the interval $[0, 49]$, with an absorbing boundary condition at 50. We used 100 trajectory segments per bin, a time-step $\tau = 0.125$ s, and we run for 160 iterations of that time-step. We note that in situations like these the measurement of rare events with an absorbing boundary condition can be somewhat sensitive to trajectory "bounce-out" from the target state as the time-step is varied. This effect is intrinsic to SSA and not particular to weighted ensemble or other sampling methods.

2.3.3.3 Results Our measurement of $P(G_{bg} \to 50 \mid 20\text{s})$, i.e. the probability of the population of G_{bg} reaching 50 within 20 seconds, was $1.20 \times 10^{-6} \pm 0.04 \times 10^{-6}$ at one standard error. We used 100 replicate weighted ensemble runs to estimate the uncertainty.

To check these results, we also performed 80 million brute-force SSA trajectories, which yielded 108 trajectories that successfully reached a G_{bg} population of 50 within 20 seconds. This

brute-force data gives an estimate for the rare event probability of $1.35 \times 10^{-6} \pm 0.13 \times 10^{-6}$ at one standard error, which corroborates the weighted ensemble result.

To estimate WE efficiency, again following Gillespie et al.[31] we can estimate the number of brute-force SSA runs that would be needed to find $P(G_{bg} \rightarrow 50 \mid 20\text{s})$ at a similar level of accuracy as the weighted ensemble result above: $N_{BF} = P(G_{bg} \rightarrow 50 \mid 20\text{s})/\sigma^2_{P(G_{bg}\rightarrow 50|20\text{s})} = 1.20\times10^{-6}/(0.04\times10^{-6})^2 = 7.3\times10^8$. In total, the 100 replicate WE runs in our measurement used 7.205×10^7 trajectory segments, which is equivalent to running $7.205 \times 10^7/160 = 4.5 \times 10^5$ brute force trajectories. This yields a speed-up of WE over brute-force SSA of $E \sim (7.3 \times 10^8)/(4.5 \times 10^5) \sim 1.6 \times 10^3$.

Petzold, Gillespie, and coworkers report values for this same rare event of $1.23\times10^6\pm0.05\times10^6$ and $1.202\times10^6\pm0.014\times10^6$ at two standard errors using two variants of wSSA [32], with speed-ups over brute-force of 20 and 250 respectively.

2.3.4 Epigenetic Switch

2.3.4.1 Model This model consists of two genes that repress each other's expression. Once expressed, each protein can bind particular DNA sites upstream of the gene which codes for the other protein, thereby repressing its transcription [91]. If we denote the ith protein concentration by g_i, the deterministic system is described by the equations:

$$\begin{aligned} \frac{\mathrm{d}g_1}{\mathrm{d}t} &= \frac{a_1}{1 + (g_2/K_2)^n} - \frac{g_1}{\tau} \\ \frac{\mathrm{d}g_2}{\mathrm{d}t} &= \frac{a_2}{1 + (g_1/K_1)^m} - \frac{g_2}{\tau} \end{aligned} \tag{2.9}$$

where $a_1 = 156$, $a_2 = 30$, $n = 3$, $m = 1$, $K_1 = 1$, $K_2 = 1$, $\tau = 1$. In our stochastic model, our chemical reactions take the form of a birth-death process, the propensity functions of which are taken from the above differential equations:

$$\begin{aligned} \varnothing &\xrightarrow{k_1(g_2)} g_1 \xrightarrow{k_0} \varnothing \\ \varnothing &\xrightarrow{k_2(g_1)} g_2 \xrightarrow{k_0} \varnothing \end{aligned} \tag{2.10}$$

where $k_0 = 1/\tau$, $k_1(g_2) = a_1/[1 + (g_2/K_2)^n]$, $k_2(g_1) = a_2/[1 + (g_1/K_1)^m]$.

For this system we define a target state and an initial configuration. The system is initially set to have $g_1 = 30$ and $g_2 = 0$, and we look for transitions to a target state, which we define as having both $g_1 \leq 20$ and $g_2 \geq 3$. This target state definition was chosen so that the rate was insensitive to small perturbations in the threshold values chosen for g_1 and g_2.

2.3.4.2 WE Parameters For this system we implemented 2-dimensional bins: 15 along g_1 and 31 along g_2, for a total of 465 bins. The bins along the g_1 coordinate were of unit width on the interval $[0, 10]$, and then of width 10 on the interval $[10, 50]$, with one additional bin on $[50, \infty]$. The bins along the g_2 coordinate were of unit width on the interval [0,30], with one additional bin on $[30, \infty]$.

The WE data in Fig. 10 was generated using 16 trajectory segments per bin, a time-step $\tau = 0.1$ s, and run for 500 iterations of that time-step, with reweighting events applied every 100 iterations. Fig. 10 shows six independent simulations using these parameters, as well as MLE statistics from our brute-force computations. Were all the bins full at all iterations, WE would compute, for each of the six runs, 3,720,000 trajectory segments of length 0.1 seconds each, which is equivalent in cost to running 372,000 seconds of brute-force dynamics. In our case, most of the bins never get populated; we computed dynamics for 148,855, 149,516, 148,940, 147,351, 146,804, and 149,765 segments in the six different runs. In toto, this is equivalent to 89,123.1 seconds of brute-force dynamics.

2.3.4.3 Results Even the state-space of this two-species stochastic system is too large to solve exactly, necessitating the use of brute-force simulation as a baseline comparison. A brute-force computation was performed using the SSA as implemented in BNG. 753 simulations of 10^6 seconds each were run, and using an exponential distribution of MFPTs, the MLE (see Eq. 2.5) of the mean and standard error of the mean, μ_{MLE} and σ_μ, were found to be 1.3×10^6 seconds and 6.5×10^4 seconds respectively for transitions from the initial configuration to the target state.

The WE results are plotted against the brute-force values in Fig. 10, where we have used the relation MFPT = 1/flux (Eq. 2.1) to plot the steady-state flux that brute-force predicts. We plot the net flux entering the target state as the simulation progresses, because this is what WE measures directly; we can infer the MFPT using the above relation. Taking the mean of each of the six

WE runs after the simulation is in steady-state (we discard the first 100 iterations), and treating each of these means as an independent data point, WE gives a combined estimate for the MFPT of $1.3 \times 10^6 \pm 3 \times 10^4$ seconds at 1-σ for transitions from the initial configuration to the target state.

WE is able to find an estimate of the MFPT with greater precision than brute-force, using the equivalent of 89,123.1 seconds of brute-force dynamics. The brute-force estimate uses 753×10^6 seconds of dynamics, yielding a speedup by a factor of $E \sim 10^4$ when using WE compared to brute-force.

WE is also able to quickly attain an efficient rough estimate of the MFPT. A brute-force estimate of the MFPT would require, optimistically, computing an amount of dynamics on the order of the MFPT itself ($\sim 10^6$s). In the six different simulations, WE's estimate of the MFPT is within 50% of the brute-force value after $\{52, 44, 37, 40, 43, 42\}$ iterations of WE simulation, at which point $\{10238, 8400, 6177, 6819, 7141, 7750\}$ trajectory segments have been propagated, which is equivalent to propagating $\{1023.8, 840.0, 617.7, 681.9, 714.1, 775.0\}$ seconds of brute-force dynamics, the mean of which is approximately 775. Thus we find a mean $E_{50\%} \approx 1.3 \times 10^6/775 \approx 1725$.

2.3.5 FcεRI-Mediated Signaling

2.3.5.1 Model To demonstrate the flexibility of the WE approach, we applied it to a signaling model that is, to our knowledge, considerably more complex than any other biochemical system to which rare event sampling techniques have been applied. The reaction network in this model [92] contains 354 chemical species and 3680 chemical reactions [93].

This model describes association, dissociation, and phosphorylation reactions among four components: the receptor FcεRI, a bivalent ligand that aggregates receptors into dimers, and the protein tyrosine kinases Lyn and Syk. The model also includes dephosphorylation reactions mediated by a pool of protein tyrosine phosphatases. These reactions generate a network of 354 distinct molecular species. The model predicts levels of association and phosphorylation of molecular complexes as they vary with time, ligand concentration, concentrations of signaling components, and genetic modifications of the interacting proteins.

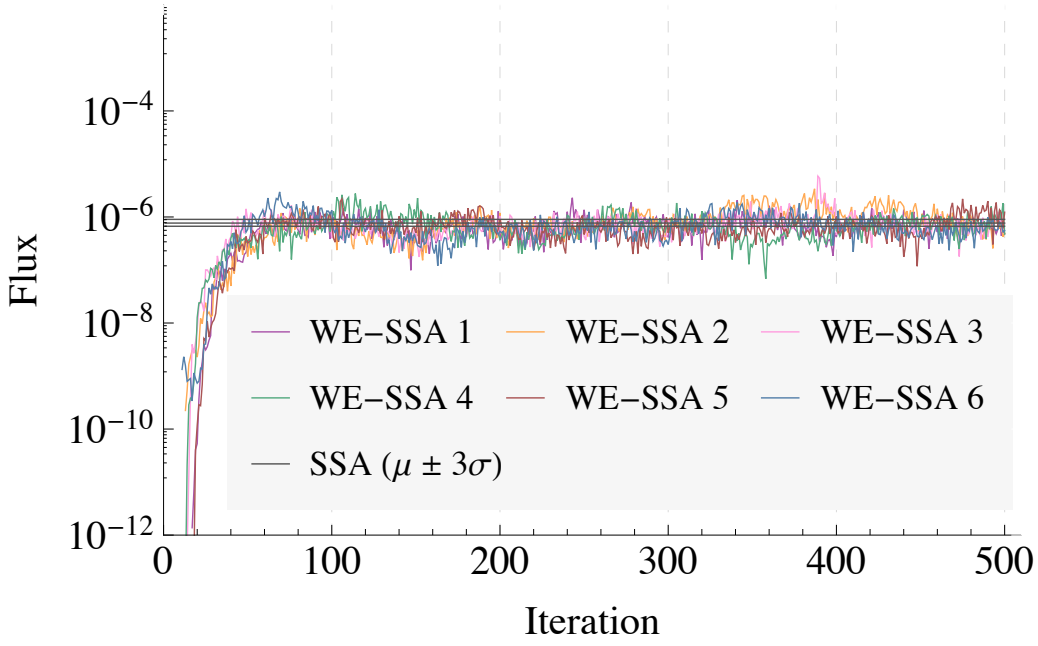

Figure 10: Measurements of probability flux into the target state for the epigenetic switch system. Six independent WE simulations are plotted, as well as the 3-σ confidence interval for the brute-force data, which is from 753 trajectories of 10^6 seconds each. The inverse of the flux gives the mean first passage time by Eq. 2.1.

2.3.5.2 WE Parameters The WE data in Fig. 11 was generated using 60 bins of unit width, 100 trajectory segments per bin, a time-step $\tau = 0.6$ s, and run for 100 iterations of that time-step, with no reweighting events. The brute-force data is from 1484 brute-force runs of 60 seconds each, which is equivalent to the dynamics time employed in attaining a single run of WE data. No attempt was made to optimize sampling times or bin widths in WE.

2.3.5.3 Results Fig. 11 shows the probability distribution of activated receptors in the FcεRI-Mediated Signaling model at time $t = 60$ s. The brute-force SSA approach is unable to sample out to likelihoods much below $\sim 10^{-3}$, while WE gets relatively clean statistics for likelihood values down to $\sim 10^{-8}$, for an estimated improvement in efficiency $E \sim 10^5$.

2.4 DISCUSSION

We applied the weighted ensemble (WE) [44, 45, 46, 47, 48, 49, 50, 51] approach to systems-biology models of stochastic chemical kinetics equations, implemented in BioNetGen [18, 53]. Increases in computational efficiency on the order of 10^{18} were attained for a simple system of biological relevance (the enzymatic futile cycle), and on the order of 10^5 for a large systems-biology model (FcεRI), with 354 species and 3680 reactions.

WE is easy to understand and implement, statistically exact [46], and easy to parallelize. It can yield long-timescale information such as mean first passage times (MFPTs) from simulations of much shorter length. As in prior molecular simulations [47, 45], WE has been demonstrated to increase computational efficiency by orders of magnitude for models of non-trivial complexity, and offers perfect (linear) parallel scaling. It appears that WE holds significant promise as a tool for the investigation of complex stochastic systems.

Nevertheless, a number of additional points, including limitations of WE and related procedures, merit further discussion.

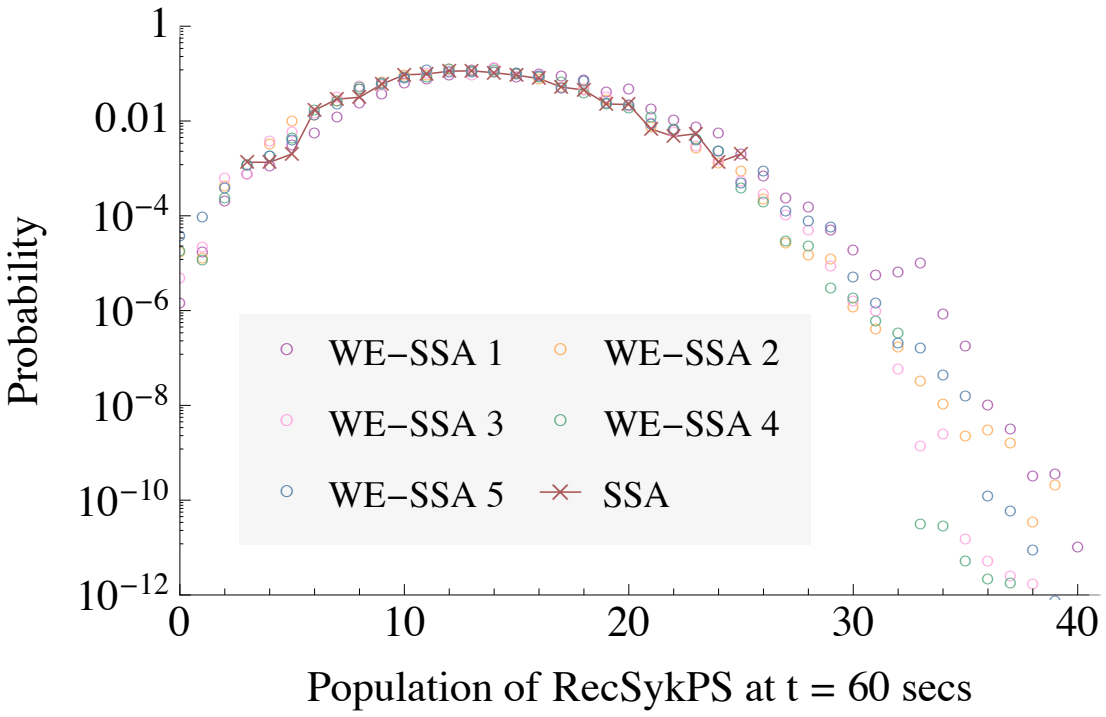

Figure 11: Comparison of WE and SSA for the FcεRI signaling model, which has 354 reactions and 3680 chemical species. The probability distribution is shown for the system reaching a specified level of Syk activation (the output of the model, which is a sum of 164 species concentrations) within one minute of system time after stimulation. Results of 1484 SSA simulations of one minute duration are compared with five independent WE runs, each generated with an equivalent computational effort as that of the brute-force SSA (several CPU hours in each case).

2.4.1 Strengths of WE

Beyond the efficiency observed for the systems studied here, the WE approach has other significant strengths. Weighted ensemble is easy to implement: it examines trajectories at fixed time-intervals, and its implementation as scripting-level code makes it amenable to using any stochastic dynamics engine to propagate trajectories. WE also parallelizes well, and can take advantage of multiple cores on a single machine, or across many machines on a cluster; Zwier et al. have successfully performed a WE computation on more than 2,000 cores on the Ranger supercomputer [51]. Additionally, WE trajectories are unbiased in the sense that they always follow the natural dynamics of the system – there is no need to engage in the potentially quite challenging process of adjusting the internal dynamics of the simulation to encourage rare events. WE also yields full probability distributions, and can find mean first passage times (MFPTs) and equilibrium properties of systems.

Is there a curse of dimensionality? In other words, for successful WE, does one need to know (and cut into bins) all slow coordinates? The short answer is that one only needs to sub-divide independent/uncorrelated slow coordinates: other, correlated coordinates, by definition, come along for the ride. Recall that WE does not apply forces to coordinates, but only "replicates success." As evidenced by the FcεRI model in Sec. 2.3.5, WE can accurately and efficiently sample rare events for a system of hundreds of degrees of freedom by binning on only the coordinate of interest, without worrying about any intermediate degrees of freedom.

For molecular systems, conventional biophysical wisdom holds that functional transitions are dominated by relatively low-dimensional "tubes" of configuration space [94, 95]. In colloquial terms, for biological systems to function in real time, there is a limit to the "functional dimensionality" of the configuration space that can be explored, echoing the resolution of Levinthal's paradox [96, 97]. Nevertheless, the ultimate answer to the issue of dimensionality in systems biology must await more exploration and may well be system dependent.

2.4.2 Comparison to Other Approaches

WE is most similar in spirit to recent versions of forward flux sampling (FFS) [37, 76, 75] and non-equilibrium umbrella sampling (NEUS) [38]. All of these methods divide up state-space into

different regions, and are able to merge and split trajectories so as to enhance the sampling of rare regions of state-space. These approaches differ slightly in the way the splitting and merging of trajectories is performed. WE also differs from FFS in that WE does not have to catch trajectories in the act of crossing a bin boundary; instead WE checks, at a prescribed time step, in which bin a trajectory resides. Though WE and FFS should be expected to perform comparably, this subtle difference can be advantageous in that no low-level interaction with the dynamics engine/software is required in WE, which makes an implementation of the WE algorithm more flexible and easy to apply to diverse systems.

The central hurdle to improving efficiency using accelerating sampling techniques such as WE, FFS, and NEUS, is to adequately divide that state-space by selecting reaction coordinates that are both important to the dynamics of interest, and that are slowly sampled by brute-force approaches. Optimally and automatically dividing and binning the state-space is, to our knowledge, an open problem, and one that, for complex systems, where a target state is unknown, is not always a straightforward one to solve, though adaptive strategies have been suggested [46, 49, 98].

The wSSA method [30] differs from the above procedures. It does not use a state-space approach, but rather uses importance sampling to bias and then unbias the reaction rates in a manner that yields an unbiased estimation of the desired observable. WE exhibits comparable or better performance to wSSA for systems to which both can be applied. Of the two models we ran for side-by-side comparisons, wSSA outperformed WE by a factor of about 100 for the simple futile-cycle model, while WE outperformed wSSA by a factor of about 6-7 on the somewhat more complex yeast polarization model. Since wSSA biases/unbiases reaction rates, while WE divides state-space, the advantage of one over the other may be situation-dependent. For instance, as noted by the wSSA authors[31], when a reaction network is finely tuned and exhibits qualitatively different behavior outside a narrow range of parameter space (e.g. the Schlögl reactions), employing a strategy that changes the rates of reactions can be very challenging. The ease of implementation of the WE framework, which does not require the potentially challenging task of biasing and reweighting multi-dimensional dynamics, would appear to scale better with model complexity than current versions of wSSA; however, for very small models such as the futile cycle, wSSA may outperform WE in measuring select observables.

A limitation which would appear to be common to accelerated sampling techniques employed

to estimate non-equilibrium observables is the system-intrinsic timescale: "t_b", or the "event duration" time [99, 100]. This timescale represents the time it takes for realistic (unbiased) trajectories to "walk" from one state to another, excluding the waiting time prior to the event. The event duration is often only a fraction of the MFPT, since it is the *likelihood* of walking this path that is low; the time to actually walk the path is often quite moderate. WE excels at overcoming the low likelihood of a transition, but it would appear difficult if not impossible for any technique which generates transition trajectories to overcome t_b, which is the intrinsic timescale of transition events.

Finally, it should be noted that all state-space methods that branch trajectories, including WE, typically produce correlated trajectories, due to the splitting/merging events. For example, the presence of 10 trajectories in a bin does not imply 10 statistically independent samples. While such correlations do not appear to have impeded the application of WE to the systems investigated here, future work will aim to quantify their effects and reduce their potential impact. The present work accounted for correlations by analyzing multiple fully independent WE runs.

2.4.3 Future Applications

Beyond potential applications to more complex stochastic chemical kinetics models, the weighted ensemble formalism could be applied to spatially heterogeneous systems. WE should be able to accelerate the sampling of models such as those generated by MCell [101, 102, 103] or Smoldyn [104], perhaps using three-dimensional spatial bins.

It may be possible to integrate WE with other methods. We note that the state-space dividing approaches of a number of methods (forward flux [21, 35, 36, 37], non-equilibrium umbrella sampling [38, 39], and weighted ensemble [44, 45, 46, 47, 48, 49, 50, 51]), since they are dynamics-agnostic, could be combined with other methods that accelerate the dynamics engine itself, such as the τ-leaping modification of Gillespie's SSA and its many variants and improvements [105, 106, 107, 108], to yield multiplicative increases in runtime speedup.

More speculatively, WE could be combined with parallel tempering methods [109, 110, 111]. WE accelerates the exploration of the free-energy landscape at a given temperature, and since it does not bias dynamics, the trajectories it propagates could be suitable for replica exchange schemes.

For complex models where exploring the state-space via brute-force is prohibitively expensive, WE could also be employed to search for bistability, or in a model-checking capacity [112, 113, 114] to search for pathological states.

2.5 ACKNOWLEDGMENTS

We gratefully acknowledge funding from NSF grant MCB-1119091, NIH grant P41 GM103712, NIH grant T32 EB009403, and NSF Expeditions in Computing Grant (award 0926181). We thank Steve Lettieri, Ernesto Suarez, and Justin Hogg for helpful discussions.

3.0 WEIGHTED ENSEMBLE IN SPATIAL SYSTEMS

3.1 INTRODUCTION

Stochastic effects are of crucial importance in many biological processes, from protein dynamics [115], to gene expression [10], to phenotypic heterogeneity [116]. Unfortunately, due to the high computational cost of simulating complex stochastic biological systems, the effects of stochasticity on system response remain under-studied in realistic biological models.

From molecular to cellular scales, simulations of biological systems push the limits of our computational resources [117, 118]. Compromising between sampling power and model complexity will be a trade-off for the foreseeable future; for example, at atomistic resolution even the most powerful, specially designed supercomputers can simulate only modestly sized proteins at timescales that approach sufficiency for adequate sampling [119]. Similarly, models of cellular processes, though they omit entirely molecular-level details, are also constrained in complexity and realism by the need to perform adequate amounts of simulation in order to gather useful statistics [120]. Mixing scales in a simulation, though perhaps necessary for capturing the coupling across multi-scale networks, only makes this problem worse.

Enhanced sampling algorithms offer an attractive proposition: instead of compromising on model complexity in order to achieve well-sampled results, rather use simulation resources more effectively and extract more information given the same resources. Not surprisingly, there has been significant interest in sampling algorithms in the field of atomistic protein simulation, including umbrella and histogram sampling [121, 122, 123], path sampling methods, [124, 37, 44, 42, 41, 39, 46], and various flavors of replica exchange [125, 109, 110, 126]. Arguably, such approaches have transformed the field of molecular simulation [127, 128, 119].

The essence of the present study is the extension of one successful enhanced sampling strat-

egy for molecular simulation to spatially resolved cell-scale systems. Specifically, the weighted ensemble approach is a scale-agnostic method that is able to facilitate the enhanced sampling of a wide spectrum of stochastic simulations and non-Markovian processes [46], including Brownian dynamics [44], molecular dynamics [48], Monte-Carlo simulations of atomistic and coarse-grained protein dynamics [45, 129], chemical reaction networks [1], and as we demonstrate here, the spatially resolved stochastic reaction-diffusion processes used to simulate cellular processes. Weighted ensemble achieves its enhanced sampling by dividing up a model's state-space into bins and maintaining an ensemble of trajectories with different weights that evenly sample these bins. This weighted ensemble is created by resampling the distribution of trajectories at fixed time intervals, spawning new simulations from trajectories that have wandered into unexplored regions and pruning them away if a region is overpopulated, in order to maintain even coverage of the space. This resampling process is exact, in the sense that it induces no bias in the estimates of equilibrium and non-equilibrium observables [46, 130]. Resampling at fixed time intervals lends the method some key benefits: it is trivially parallelizable, since trajectories run independently aside from interacting infrequently during resampling, and it is modular, needing no "under the hood" interaction with the underlying dynamics, rather requiring only intermittent reports of a progress coordinate.

Spatial heterogeneity can be crucial to accurately capturing the behavior of cell-scale biological systems, for instance in models of neuromuscular junction dynamics studied below [131]. Although simple models of biological signaling, where the molecules of interest are spatially homogeneous, or "well-mixed" are very common [16, 132], the assumption of spatial homogeneity may not always be justified; certain biological systems, while suitable for ignoring molecular structure, are not amenable to being modeled as spatially homogenous. Indeed, high resolution microscopy images of single cells show distinct patterns of localization for a wide variety of biomolecules [133, 134, 135], leading one to speculate if the well-mixed regime is the exception rather than the rule.

Here, we apply the weighted ensemble sampling procedure to decrease the cost of simulating spatial stochastic systems. After introducing our methodology, we present results for a toy diffusive binding system and two more complex systems: a cross-compartmental signal transduction model in a realistic cellular geometry and a model of an active zone in a frog neuromuscular junction.

The flexibility and power of the WE method make it ideally suited for enhancing the sampling of these three diverse models.

3.2 METHODS

We employ the weighted ensemble sampling algorithm to manage multiple instances of particle-based kinetic Monte Carlo simulations of a given spatially resolved model of cellular signaling. We make use of a variety of software packages in our work, all of which are freely available via MMBioS.org.

3.2.1 Weighted Ensemble

The weighted ensemble sampling strategy achieves enhanced sampling by maintaining an ensemble of simulations running in parallel, distributed evenly across the configuration or state space of a system. To do this, the configuration space of the system is typically divided into different region, or "bins", according to the values of some progress coordinate(s). The parallel ensemble of simulations is periodically paused, and each simulation is inspected to ascertain which bin it inhabits. Simulations in overpopulated bins are pruned away until a desired population is reached, and simulations in underpopulated bins are duplicated until a sufficient population is reached. After this brief resampling process, the ensemble of trajectories is restarted, and the native dynamics of the system continues, until it comes time to pause and resample again. By assigning each trajectory a statistical weight and conserving this weight during pruning and cloning operations, the ensemble remains unbiased, while efficiently sampling otherwise difficult to reach regions of configurations space [44].

The essence of the weighted ensemble sampling procedure is encapsulated in Fig. 1, where we have chosen to divide the example system along one coordinate into three bins, and have a target number of two trajectories in each bin. Before the simulation begins, the configuration space of the system must be considered, and typically a progress coordinate (or more than one) along which a trajectory can be tracked is selected. Although automated binning procedures have been developed

[46, 49], we do not use them in the studies reported here. The configuration space of the system is divided into non-overlapping bins of the selected progress coordinate(s) that completely cover the configuration space. This division is usually done ahead of time, but "on the fly" modifications are also permitted [46]. In Fig. 1, a one-dimensional projection of a system is shown, and the space is divided into three bins, which remain the same throughout the simulation. For efficient sampling, the progress coordinates chosen should be associated with a set of slowly varying and uncorrelated processes; additional progress coordinates tend to increase computing cost without a sufficient "payoff" in sampling. Additional slowly varying progress coordinates can speed up sampling of slow/rare processes in the system, but choosing progress coordinates that are uncorrelated is also important, because correlated coordinates are redundant in the variation of the system that they capture. The expense of maintaining bins full of trajectories increases drastically with the number of progress coordinates used, making it essential to use additional progress coordinates only when they are crucial to capturing new information about the system.

In the basic weighted ensemble procedure, a number of replicate trajectories are initiated from a chosen initial state, with weights summing to one, and are simulated for a short time τ. After that short time, the simulations are paused and inspected for progress along the chosen progress coordinates. If a trajectory has wandered into a new, previously unpopulated bin, that trajectory is replicated, and the statistical weight of that trajectory is divided among these "daughter" trajectories. If a bin becomes over-populated, trajectories are pruned and their weights are reassigned. After this pause in dynamics for resampling, the trajectories are restarted, and the entire process is iterated as desired.

The resampling strategy of WE is exact for arbitrary types of stochastic dynamics in any number of dimensions [46, 130]. Typically, when we divide the configuration space of the system into bins, we set a target number of trajectories for each bin; if, during one of the intermittent resampling events, the number of trajectories in that bin is greater or less than the target (but nonzero), we either up- or down-sample the trajectories in the bin to reach the target number, always accounting for the statistical weights of each trajectory. "Up-sampling" connotes spawning new trajectories, identical to the original but with the original trajectory's statistical weight now split between the new and old trajectories. For instance, during the $t = \tau$ resampling event in Fig. 1, the trajectory in bin 2, initially possessing a weight of $1/2$, spawns an identical copy of itself, and the weight

of the original trajectory is evenly divided so that the two resultant trajectories each have a weight of 1/4. "Down-sampling" is a pruning process, whereby trajectories are compared in a pairwise fashion and one is deleted based on a random process, with a likelihood of survival proportional to the statistical weight of the trajectory. For instance, during the $t = 2\tau$ resampling event in Fig. 1, the three trajectories in bin 1 all have weight 1/4, so two of them are selected, and a random number draw (evenly weighted, since both trajectories have the same weight) decides which one remains. By these two simple processes, an ensemble of trajectories is created that evenly samples the state space of the system without bias [46].

The resampling process adds a small amount of computational overhead to the overall cost of sampling. This expense, however, is a small fraction of the total cost, provided that either the dynamics of the system are expensive to simulate, or the resampling interval is long compared to the timescale of the internal dynamics of the simulation, which we find is almost always the case in systems of interest. For instance, when using weighted ensemble to run simulations of molecular dynamics [48], large chemical kinetics networks [1], or the spatially resolved stochastic chemical kinetics studied here, the trajectories will typically run for a wall-clock time on the order of minutes or hours before being paused for resampling, while the resampling operation itself takes on the order of seconds. Indeed, the resampling arithmetic itself is trivial in complexity compared to the stochastic dynamics of the trajectories themselves, and most of the time spent during resampling is actually spent reading and writing to disk and starting and stopping trajectories (if the data are too large to store in memory). Like any enhanced sampling method, WE is worthwhile only for complex models exhibiting a wide variety of timescales.

The benefit of this resampling process is that it facilitates the efficient, exact sampling of the system along the binned progress coordinates. As illustrated schematically in Fig. 12, in a naïve "brute-force" approach, where a number of independent trajectories are simulated and then compiled into a histograms of outcomes, the sampling power of the ensemble is concentrated about the peak of the distribution.

By definition, the peak contains the most probable events. Thus, certain parts of the configuration space are destined to be poorly sampled; if the true probability of a state being occupied is less than the inverse of the number of trajectories simulated, it is unlikely to be sampled even once. On the other hand, weighted ensemble decouples the number of trajectories in a region of

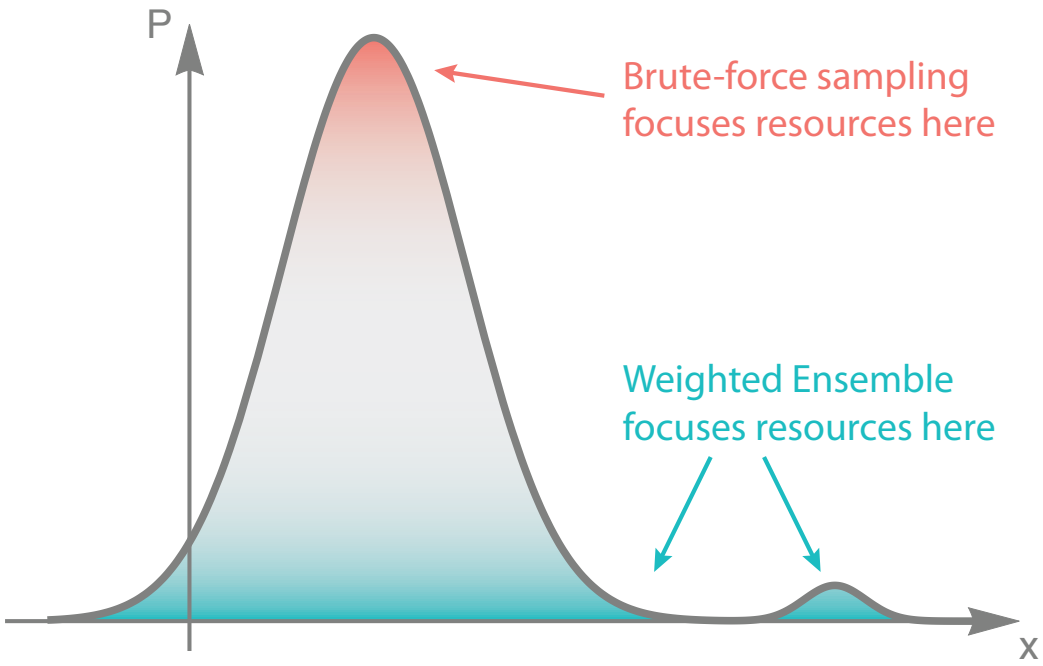

Figure 12: **Distribution of Sampling Power.** Brute-force sampling, by definition, concentrates sampling power on the most probable events. By contrast, weighted ensemble samples a distribution more evenly, and compared to brute-force it applies more resources to hard-to-sample regions of interest.

configuration space from the probability of a trajectory to be there, and allows for a more even coverage of all regions of the underlying distribution. It should be noted that an even coverage of configuration space lends itself to efficient sampling only if the coordinate(s) along which this coverage is distributed are useful in characterizing the observables of interest [46]. That is, the payoff of using weighted ensemble sampling depends on one's choice of progress coordinate and bins, and efficiently sampling certain regions of configuration space may prove unrewarding.

The efficient sampling of low-probability regions of the (time-dependent) probability distribution of a stochastic system can be leveraged to extract unbiased estimates of long-timescale information about the system. Specifically, the Hill relation [82] provides a link between the mean first passage time (MFPT) between two states A and B, and the steady-state flux of probability (flow per unit time) between them:

$$\mathrm{MFPT}(A \to B) = \frac{1}{\mathrm{Flux}(A \to B)} \quad , \tag{3.1}$$

where $\mathrm{Flux}(A \to B)$ here refers to the probability (per unit time) that a trajectory, which at some point in the past originated in A, arrives at B for the first time. This relationship is exact (up to statistical noise) when the system exhibits a steady-state flow of probability from A to B. These two states A and B can be single micro-states, or large states composed of many smaller sub-states (e.g. weighted ensemble bins); they can also be arbitrarily defined independent of the WE bin boundaries.

A steady-state is achieved when the probability distribution of the system is constant in time. That is, for each sub-state i in the system, in a given time period the total flow of probability into i from the other sub-states is equal to the flow of probability out of i into other sub-states. In terms of the steady-state probabilities p_i of each sub-state, and the transition probabilities k_{ij} between sub-states (in an arbitrary, but fixed, time interval), the steady-state condition is given by

$$\forall i : \sum_j k_{ji} p_j = \sum_j k_{ij} p_i \ . \tag{3.2}$$

The conditional probabilities k_{ij} can be estimated from WE, and the p_i values can then be inferred by solving the linear system in Eqn. 3.2. The $\mathrm{Flux}(A \to B)$ needed for the MFPT in Eqn. 3.1 is obtained by summing over all steady-state probability flow into B:

$$\mathrm{Flux}(A \to B) = \sum_{i \notin B} \sum_{j \in B} p_i k_{ij} \quad , \tag{3.3}$$

where the k_{ij} and p_i values are obtained solely from trajectories originating in A [130].

To accommodate a steady state, the boundary conditions of the weighted ensemble simulation described above must be slightly adjusted to induce a steady-state flow of probability from the initial state to the target state. This is accomplished by removing a trajectory from the ensemble whenever it enters the target state, and re-starting a new trajectory from the initial state with the same probabilistic weight as the one just removed. After a sufficient amount of time the system will relax into a steady flow of probability from one state to another, with probabilities in each bin maintained at a steady value. After this "burn-in" period, the Hill relation can be employed to estimate the MFPT.

Although not used in this report, we note that since the transition rates between bins can often be estimated accurately even before the probability distribution has relaxed to a steady state, a Markov-like transition matrix can be constructed and solved to infer long-timescale properties of the system, including the mean first passage time [130]. This approach is more efficient than waiting for the system to relax into a steady state when the probability mass itself is slow to relax, so long as there are sufficient transitions between bins, and the degrees of freedom orthogonal to the bins are either well-sampled or unimportant.

Throughout this work, we use the WESTPA [136] implementation of the weighted ensemble algorithm, which is freely available and open source (github.com/WESTPA). This implementation is flexible and adaptable for use with any stochastic dynamics engine, and supports plugins for extended methods such as the steady-state approach noted above. Interfaces currently exist for use with Gromacs, NAMD, AMBER, BioNetGen, and the present work provides one for MCell [136].

In order to simplify the process of using weighted ensemble sampling techniques with systems biology models, we have constructed an automated service to convert MCell models into ready-to-go WESTPA simulations, available at weightedensemblizer.csb.pitt.edu).

There are different ways to characterize the gain in efficiency from using weighted ensemble instead of brute-force sampling. We find that a useful approach to evaluating efficiency, which is independent of specific computational architecture, is to take the sum of the simulated dynamics time in the weighted ensemble approach, and compare those results to simulating the same amount of dynamics in brute-force simulations. For instance, the single weighted ensemble run for the toy diffusive binding model presented in the Results section spawned a total of 610,704 trajectory

segments in its 1000 iterations; as such, it is equivalent to simulating 610,704/1000 = 610.704 brute-force trajectories. Thus, always rounding up to give brute-force the benefit, we compare the weighted ensemble results to the results of running 611 brute-force simulations. The statistical precision exhibited by each method can then be compared on the basis of equal time spent simulating dynamics. As mentioned above, the overhead imposed by weighted ensemble resampling is very small compared to the time spent simulating dynamics for most systems of interest, so for models of even moderate complexity, we find this to be a fair comparison of efficiency.

Because WE trajectories, and hence observables, exhibit correlation within a single simulation, it can be important to perform multiple, independent weighted ensemble runs to ensure uncorrelated estimates of observables. When comparing the performance of brute-force sampling to multiple independent weighted ensemble runs, for each WE run we construct a brute-force ensemble of equivalent cost to each independent WE run, as described above. We can then compare the results of the multiple brute-force ensembles to the multiple independent WE runs on equal footing.

3.2.2 Kinetic Monte Carlo for spatial behavior of biochemically active species: MCell

All simulations in this report employ spatially resolved particle-based kinetic Monte Carlo dynamics, implemented in the MCell software package. MCell (Monte Carlo Cell) is an open source program (MCell.org) that uses spatially realistic 3D cellular models and specialized Monte Carlo algorithms to simulate the movements and reactions of molecules within and between cells, or what is referred to as "cellular microphysiology" [102]. MCell has been used to study a wide range of neuroscience questions such as neurotransmitter diffusion in the brain [137], the structure and function of synapses in the central [138] and peripheral [131] nervous system, and the effect of drugs on nervous system function [139]. MCell has also been employed to investigate general cellular phenomena such as calcium signaling [140] and the role of diffusion in cellular transport [141].

MCell combines rigorously validated and highly optimized stochastic Monte Carlo algorithms, particle-based random walk diffusion of (point particle) molecules in space and on surfaces, and stochastic biochemical state transitions. MCell models can contain arbitrarily complex 3D mesh geometries representing the biological system under consideration. These geometries are typi-

cally derived from reconstructions of biological tissue (typically from electron microscopy data) [142], or created in silico based on average geometries [131], e.g. via CellBlender software (github.com/mcellteam/cellblender) [143]. MCell features a flexible model description language and has the ability to checkpoint simulation trajectories at arbitrary output intervals or times.

MCell is a *kinetic* Monte Carlo scheme, in the sense that the time evolution of the system is explicitly modeled. The Monte Carlo moves that the system makes are not arbitrary trial moves, but are rather chosen according to the reaction and diffusion rates of the molecules being simulated. A constant time-step is employed in these simulations, during which the likelihood of reaction and diffusion processes are computed and stochastically sampled; by using appropriate time-steps, the dynamics of the underlying processes are faithfully recapitulated (for further details, see [103, 101, 102]).

3.2.3 Complex model construction: CellOrganizer and BioNetGen

The construction of large, complex spatial models is facilitated by a combination of software that specializes in separate aspects of this task.

One of the limiting factors in performing spatially realistic cell simulations is the difficulty of obtaining cell geometries. This limitation can be addressed by learning generative models of cell organization directly from microscope images; these can be used to synthesize an unlimited number of realistic geometries. For instance, in the complex model in a realistic cellular geometry studied below, biochemical reaction networks, with corresponding compartments for organelles, are constructed using BioNetGen software [53, 144], combined with cell geometry models generated by CellOrganizer software [145, 146, 147, 148, 149, 150, 151, 152, 153] using CellBlender [143] to create the MCell spatial simulations [154]. More information about this process of generating cellular instances with realistic cellular and subcellular organizations/morphologies is given below. The WESTPA software in turn manages ensembles of the MCell simulations, for either weighted ensemble or brute-force sampling.

CellOrganizer (CellOrganizer.org) is an open source tool for learning conditional generative models of cellular organization from images [145, 146, 147, 148, 149, 150, 151, 152, 153]. From these models, new cellular geometries can be generated from different parts of the "shape space"

of the system. Currently CellOrganizer supports models for cell shape, nuclear shape, vesicle frequency, location and size, and microtubule length, number and distribution. Important for this work is CellOrganizer's ability to produce realistic geometric instances of cells and subcellular components for use in modeling using the experimental spatial extension of the Systems Biology Markup Language (SBML) [155].

Biochemical reaction networks in our model of signaling in a realistic cellular geometry are built with the BioNetGen software package (BioNetGen.org), which is a framework for specifying and simulating rule-based models of biochemical kinetics [53]. The rule-based approach allows combinatorially large chemical reaction networks to be compactly described using a small set of rules that define the underlying molecular interactions [144]. Indirect simulation of rule-based models requires automated generation of the reaction network implied by the rule set. The generated reaction network can then be simulated using a variety of approaches including ordinary differential equations and stochastic simulation. BioNetGen has previously been used to model a wide range of processes including signal transduction, metabolic pathways, and genetic regulatory networks [144]. BioNetGen enables the cellular topology to be defined via compartments [156], but it does not provide for the specification of more detailed geometric information about these compartments or molecule locations. An automated process converts these rules to an exhaustive network of chemical reactions representing the chemical kinetics of the system (see Fig. 13).

The reaction network from BioNetGen is fed into CellOrganizer to obtain an appropriate cellular geometry, and the network and geometry are combined using the CellBlender package. In CellBlender, the reactions and geometry are merged, and exported to MCell. The system is then simulated as usual in MCell, either using weighted ensemble to manage the trajectories, or via brute-force.

3.3 MODELS

We investigate three spatial models of cellular function: (1) a toy model of diffusive binding, (2) an idealized model of cellular signaling, and (3) a realistic model of a neuromuscular junction. All three particle-based kinetic Monte Carlo models are simulated in MCell (version 3.2.1), and are

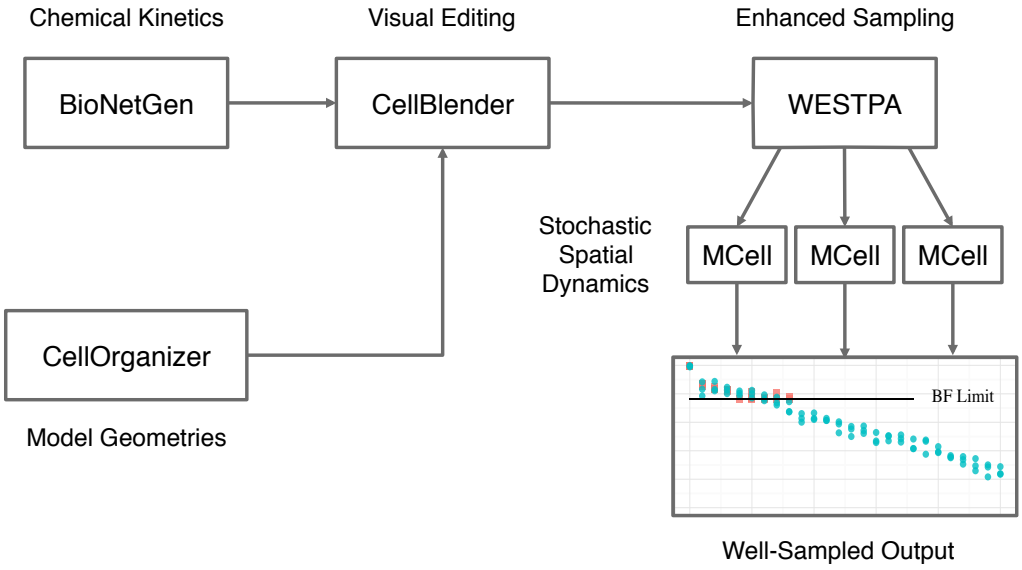

Figure 13: **Software Pipeline for realistic cell geometry simulations.** Geometries are learned from images by CellOrganizer. Chemical reaction networks are generated from rule-based models in BioNetGen. Geometries and reaction networks are imported to MCell via the CellBlender visual editor. The spatial stochastic model is then simulated in MCell, with WESTPA managing a weighted ensemble of MCell trajectories.

available in the supporting information.

3.3.1 Toy Diffusive Binding Model

A highly simplified model of diffusive binding was constructed as an initial test of the utility of weighted ensemble sampling in a spatial system. The model geometry is depicted in Fig. 14.

In this toy model of diffusive binding, we define a cubical volume, of side length 2 microns, on the top of which 1000 ligands are initially bound to 1000 receptors at time $t = 0$. The volume also contains 1000 receptors at the bottom of the cube that are initially unbound. The ligands are then free to unbind (with a constant of 10^3/sec), diffuse around the volume (with a diffusion constant of 10^{-6}cm^2/sec), and re-bind to receptors at the top, or to receptors at the bottom (with a constant of 10^8/M/sec). We examine the probability density for the number of receptors at the bottom of the volume bound by ligands after simulating 10 milliseconds of dynamics.

The toy model has an internal time step of 10 microseconds, and we perform weighted ensemble resampling at an interval that exactly coincides with the internal time step, or every 10 microseconds. We simulate the model for 10 milliseconds, or 1000 weighted ensemble iterations. The progress coordinate we use is the number of receptors bound at the bottom of the cube, with bins on this coordinate at integers on [0,1000], and we simulate 16 trajectory segments in each bin.

3.3.2 Complex Model in Realistic Cellular Geometry

There is significant interest in the variation of cellular morphology and its association with cell fate/function[157, 158, 159, 160, 161, 154], and here we employ a model that is a prototype for computationally investigating the effect of a specific geometry upon biological function. The system models protein production in response to an extracellular signal and highlights interesting aspects of signal transduction through different subcellular components, such as transport across membranes and feedback between molecules in different subcellular locations [154]. The model contains on the order of 10^5 reactive molecules, situated in a realistic cellular geometry. Because creating robust, high-quality complex models of cells is itself a challenging endeavor, we employ the model generation pipeline through BioNetGen and CellOrganizer described in the Methods section and Sullivan et al. [154].

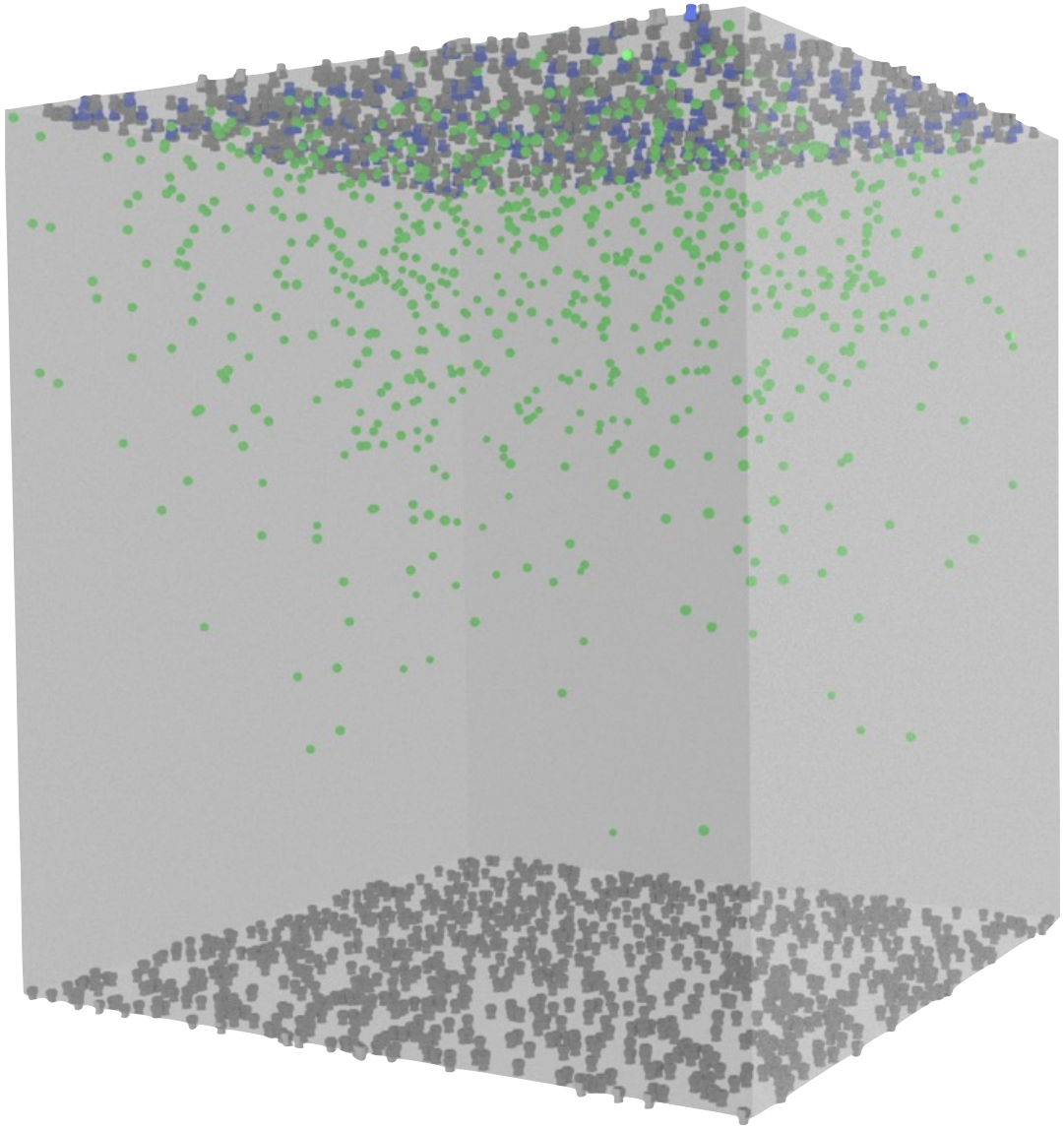

Figure 14: **Toy Model Geometry.** This toy system has receptors at the top and bottom of a cubical "cell". The receptors at the top are initially bound by ligands, that are free to unbind and diffuse around the cell, and bind to receptors at the bottom.

We use the geometry shown in Fig. 15, which is derived from three-dimensional images of HeLa cells using CellOrganizer. This geometry contains topologically distinct partitions: the extracellular region, the cytoplasm, the nucleus, and approximately 500 endosomes. The geometry also includes the membranes that partition these compartments, through which molecules must be transported when appropriate. Further details are included in the Supporting Information.

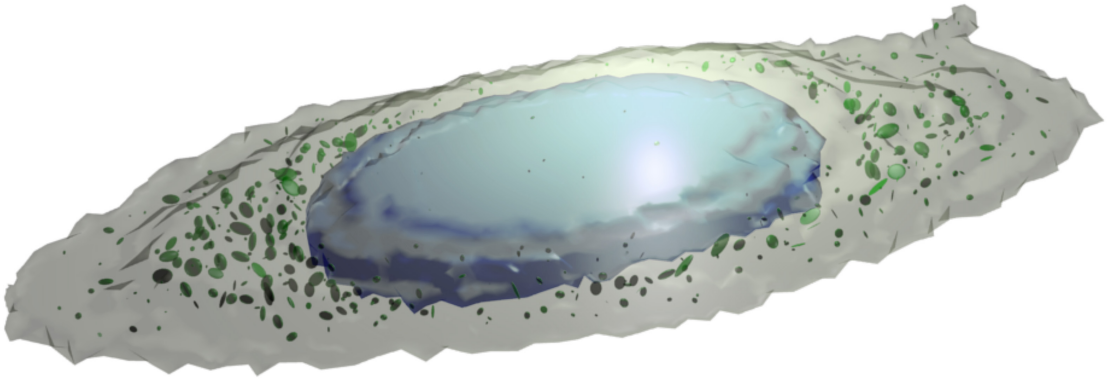

Figure 15: **Cellular Geometry.** Realistic cell geometry generated from microscopy images by CellOrganizer. The geometry explicitly models the compartmentalization of the cell, by forcing molecules to diffuse through membranes to transition from, for example, the cytoplasm (grey) to the nucleus (blue). Also modeled are endosomes (green), and the extracellular environment (transparent).

We use the reaction schema illustrated in Fig. 16 to describe the reaction kinetics of the model. The BioNetGen rules for this model are included in the Supporting Information, and they produce a network of 354 chemical reactions between 78 species [156]. Briefly, the signaling network functions as follows. The system is initialized in a state of unbound receptors, and free extracellular ligands. The extracellular ligand binds to receptors on the cell membrane, facilitating receptor dimerization, which can be internalized to the endosomes. In the endosomes, receptor dimers can become phosphorylated and recruit a transcription factor, which upon phosphorylation can also dimerize and migrate to the nucleus. In the nucleus, the transcription factor initiates the transcription of mRNA1, which, when it migrates to the cytoplasm, produces protein P1. P1 can then migrate to the nucleus and act as a transcription factor for mRNA2, which, when it migrates to the cytoplasm, produces the final species in the cascade, protein P2. Although this reaction network

is idealized, it embodies key aspects of the complexity expected in real signaling processes.

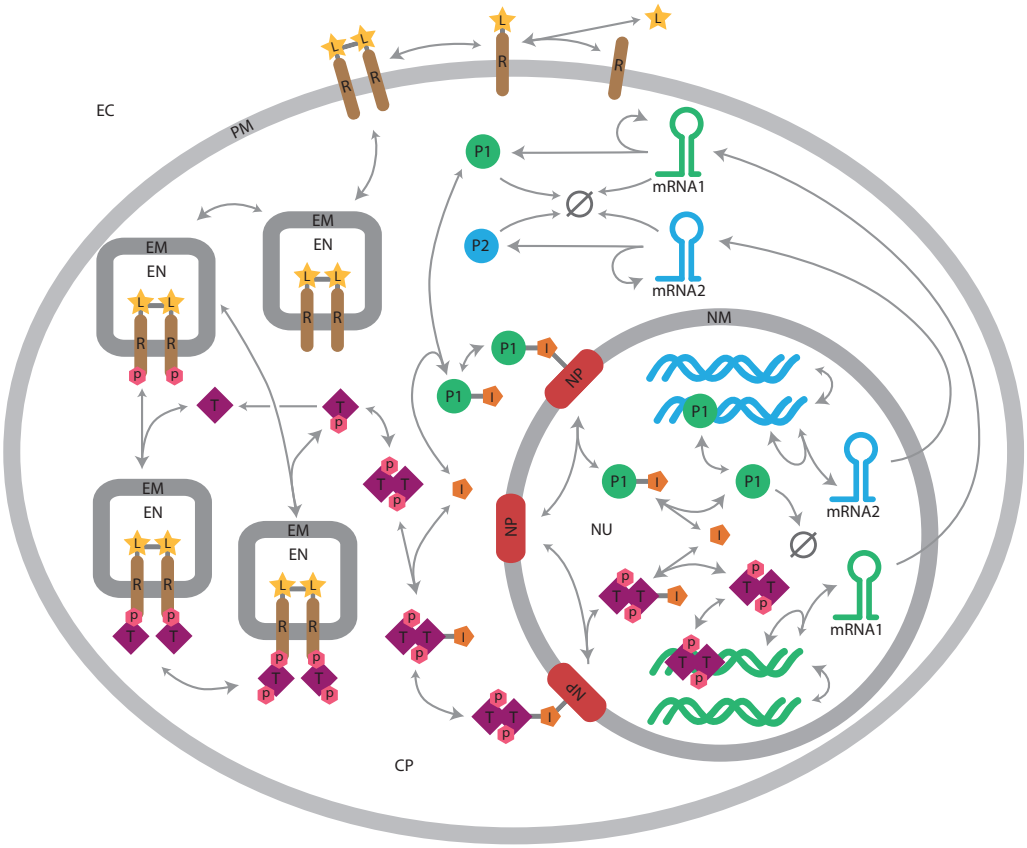

Figure 16: **Signal Transduction Network.** This rule-based model is translated into a system of chemical kinetics reactions by BioNetGen, and then simulated in a spatially realistic geometry by MCell. Figure adapted from [156].

The weighted ensemble simulation of the spatial signaling model has an internal time step 100 microseconds, and we perform weighted ensemble resampling once every second, i.e. every 10^4 internal time steps. We simulate the model for 500 seconds, or 5 million internal MCell time steps, i.e. 500 weighted ensemble iterations. We use a single progress coordinate for this system, the total number of P2 molecules in the system. The bins on this coordinate are integers on [0,25] and one bin from 25 to infinity. We simulate 48 trajectories in the bin containing 0, and 16 trajectory segments in each other bin. Note that many coordinates (e.g., P1, ligands, mRNA1 and mRNA2, etc) are not divided into bins, as is typical of WE simulations of complex systems.

3.3.3 Neuromuscular Junction

The third model we study represents a single active zone of a frog neuromuscular junction (NMJ). Synapses are of crucial physiological importance in neural function, yet their detailed molecular behavior, particularly the way in which calcium triggers synaptic vesicle fusion still lacks a complete, molecular level, characterization. This is mainly due to the lack of experimental approaches that can probe synapses at the required spatial and temporal resolution. Computational models can provide critical microscopic insight into how calcium binding triggers vesicle fusion and release [131].

The geometry of the frog NMJ active zone model is detailed in Fig. 17 and has been described previously [131]. The active zone model consists of a double row of 26 synaptic vesicles and two rows of 26 voltage gated calcium channels (VGCCs) in the space between vesicles (see Fig. 17). Thus each synaptic vesicle is associated with a single VGCC.

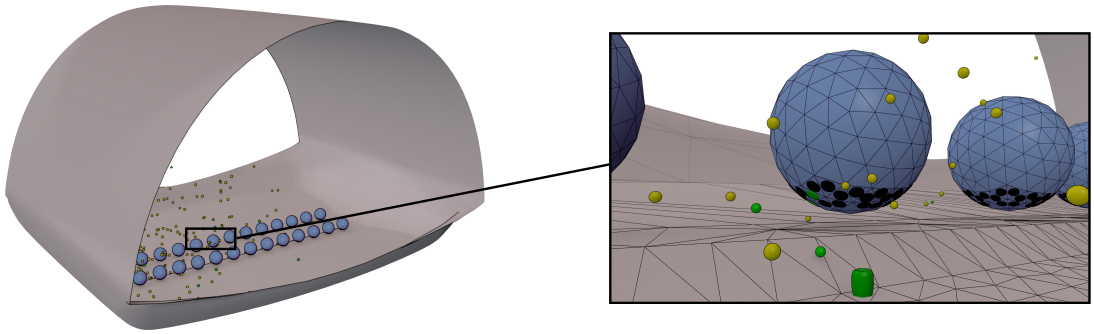

Figure 17: **Schematic of the Model of an Active Zone of a Frog Neuromuscular Junction.** On the left is an example snapshot from a simulation, and on the right is a zoomed-in view of the model. Calcium is released into the presynaptic space and is free to diffuse around the geometry and bind to the synaptic vesicles at the bottom of the active zone.

The system is initialized from a state of no free calcium in the active zone. During a simulation, VGCCs open stochastically, driven by a time-dependent action potential waveform [131]. Once open, VGCCs conduct calcium ions into the presynaptic space. Calcium ions can then freely diffuse and either bind to $\sim 10^6$ static buffer molecules or one of eight calcium sensor proteins (synaptotagmin) on the synaptic vesicles. Since each synaptotagmin protein has five calcium bind-

ing sites, each synaptic vesicle contains a total of 40 calcium binding sites. A synaptotagmin protein is activated after binding at least two calcium ions, and vesicle fusion is triggered once three out of its eight synaptotagmin proteins have been activated. For each simulation we track the calcium binding events to synaptotagmin sites on synaptic vesicles and can thus determine the number of released vesicles and the time of release.

The NMJ model differs crucially from the two other systems studied here in that it possesses rate "constants" that vary in time. Specifically, the rates for the opening of and calcium conduction through VGCCs in the model are time dependent and are parameterized according to an experimentally measured action potential waveform. This time-dependent nature of vesicle release in synapses is critical for their physiological function [131]. Thus, the model, with its time-varying kinetics, can not be treated using steady-state or equilibrium approaches and is only usefully simulated, even with a weighted ensemble, out of equilibrium and for a predetermined period of time.

Weighted ensemble simulation of the NMJ model used an internal time step of 10 nanoseconds, and we performed weighted ensemble resampling at an interval of 6 microseconds for the low calcium conditions. In total, we simulate the model for 3 ms, i.e. 500 weighted ensemble iterations.

The progress-coordinate space for the NMJ system was two dimensional: one dimension was the total number of calcium ions bound to all synaptotagmin molecules on a vesicle, and the other was the number of activated synaptotagmin molecules on that vesicle. Since a vesicle fuses once three synaptotagmin molecules are active, the latter coordinate had integer bins from zero to three. For the coordinate tracking the number of bound calcium ions per synaptotagmin, the bins were integers on the interval [0,20], and one bin from 20 to 40.

The NMJ progress coordinate was chosen to facilitate the observation of fusion events, in a manner that is somewhat complicated but also serves to illustrate the flexibility in the type of progress coordinates that WE accepts. Of the 26 vesicles in the simulation, the one that was closest to fusion was chosen at every WE iteration. That is, the vesicles were sorted in descending order by number of activated synaptotagmin proteins, and then by number of total calcium ions bound; the vesicle at the top of the list was chosen. This ranking was performed at every weighted ensemble resampling event, so in principle the vesicle in question could change during the simulation, but always in favor of progress towards a fusion event.

Due to the time dependent VGCC rate constants in the NMJ model, even weighted ensemble

sampling can have difficulty efficiently filling up bins of state space. This is because some regions that are initially difficult to sample become easy to reach, and time spent populating intermediate bins is in some sense ill-spent – the model is still sampled, but the efficiency can be less than ideal if one attempts to always have all bins full of trajectories. To address this issue, instead of performing a single weighted ensemble run with a large number of trajectories, we perform many, less intensive weighted ensemble runs with fewer trajectories and average the results. Specifically, for the low calcium regimes of 0.5 and 0.3 mM in the Results Section for the NMJ model, we performed 100 independent weighted ensemble runs for each system. The 0.5 mM system maintained a target of 8 trajectory segments per bin, while the 0.3 mM system maintained a target of 16 trajectory segments per bin. As noted above, multiple independent weighted ensemble runs facilitate error estimation.

3.4 RESULTS

We sampled the three spatially resolved cell-scale models of varying complexity using the weighted ensemble approach. The results from all three models demonstrate the ability of WE to sample rare events in models of varying spatial and biochemical complexity. The application of WE sampling to the NMJ model generated novel data about vesicle release in regimes of calcium concentration too difficult to sample well with conventional methods.

3.4.1 Toy Diffusive Binding Model

Our studies of rare event sampling in spatial stochastic systems start with the toy model shown in Fig. 14 and described in detail in the Models section. Briefly, we simulate diffusing ligands unbinding from the top of a cubical volume and binding to the bottom for a short amount of time. In this time-span, it is rare for a large number of the ligands to bind at the bottom of the volume. Indeed, when we simulate the system 611 times via brute-force, we see that in most cases only about 10-20 receptors are bound at the bottom after 10 milliseconds. We simulated 611 brute-force trajectories in order to make a fair comparison of weighted ensemble sampling to a brute-force approach; the single weighted ensemble simulation we performed required computational

resources equivalent to 610.7 brute-force simulations. Looking more closely at Fig. 18 (see inset), we see that it will be impossible to adequately characterize events rarer than $1/611$ via the brute-force ensemble of simulations, since the rarest event one can see with brute-force is equal to the inverse of the number of trajectories. On the other hand, the weighted ensemble approach is able to sample the distribution over many orders of magnitude of probability with an equal amount of computational effort as the brute-force ensemble.

Since a toy model even this simple is too complex to solve exactly, we compare the data from both the single weighted ensemble simulation and the equivalent brute-force simulations to a more authoritative estimate of the probability distribution obtained by exhaustive (weighted ensemble) simulation. To obtain this reference value, we performed 64 independent weighted ensemble simulations with the same parameters as the single "test" weighted ensemble run (blue circles, Fig. 18), except that each of the 64 runs had 32 trajectory segments per bin, rather than 16 for the test run (i.e. approximately 128 times the sampling power of the single run). From the 64 independent runs (gray circles, Fig. 18), we then computed the 95% confidence interval for the mean probability distribution using 10,000 bootstrap samples at each progress coordinate, from 0 to 70. Even though the exhaustive weighted ensemble runs and the single test run use different weighted ensemble parameters (i.e trajectories per bin), this difference does not substantially affect the sampling quality of the ensembles. Note that the 95% confidence interval for the mean of the true distribution is significantly tighter than the variance of the distribution of weighted ensemble samples of that distribution; the fact that the single run falls outside this interval is typical of the stochastic noise inherent in a single WE sample.

As explained in the Methods section, weighted ensemble is able to sample more of the complete distribution by efficiently spreading out the sampling power of the ensemble of trajectories, allowing the characterization of rare-events by sacrificing some accuracy in the regime where brute-force samples well (see Fig. 12). Examining Fig. 18, we see that the brute-force distribution is smoother at the peak of the distribution – indicating less uncertainty – but only marginally so; the weighted ensemble estimate of the peak of the distribution is also reasonably smooth. By sacrificing unneeded resolution at the peak, WE is able to instead spread that sampling power more evenly throughout the state-space of the model, using it to sample the full probability distribution more comprehensively.

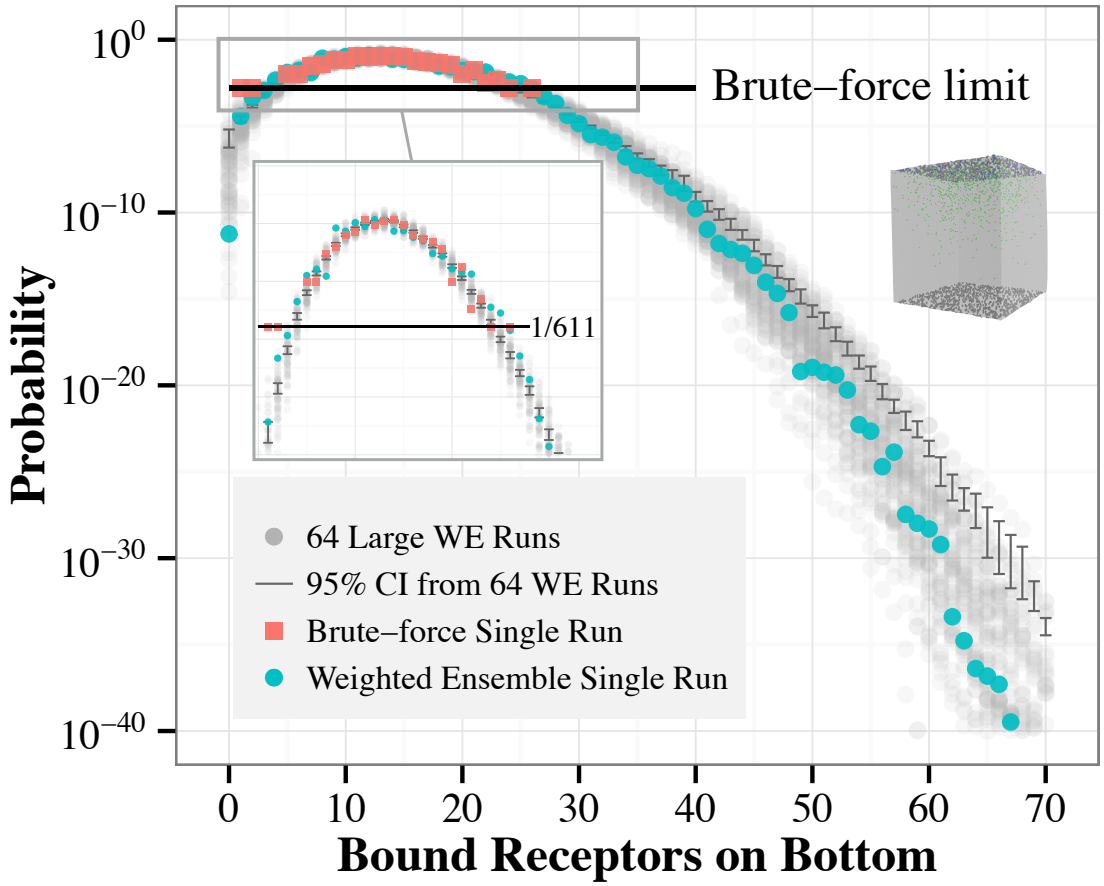

Figure 18: **Sampling Rare States of the Toy Binding Model.** Shown is the probability distribution of the number of bound receptors on the target side of the cell after 10 milliseconds of simulation. The weighted ensemble data (blue circles) is plotted with brute-force data (red squares) generated using equal computational effort, i.e. 611 brute-force runs. Brute-force sampling is confined to the peak of the distribution, whereas weighted ensemble sampling captures more of the full probability distribution. To compare both approaches to an authoritative value, an exhaustive set of 64 large weighted ensemble simulations was performed (grey circles), from which a bootstrapped 95% confidence interval for the mean probability distribution was calculated (dark grey bars).

3.4.2 Cross-Compartmental Signaling Network in a Realistic Cell Geometry

The model of cellular signal transduction shown in Figs. 15 and 16 contains $\sim 10^5$ reactive molecules in a realistic geometry, and demonstrates the ability of the weighted ensemble sampling approach to scale to large, complex systems. We focus on characterizing the synthesis of protein P2. The production of P2, the last step in the cascade shown in Fig. 16, is challenging to sample via brute-force. Nonetheless, it is a crucial quantity to calibrate if one is interested in the effects of spatial heterogeneity on the model, and we do so using weighted ensemble.

To begin our exploration of the signaling model, we initially examine the production of the protein P2 after 400 seconds of simulation (see Fig. 19). The weighted ensemble data was produced by two independent runs, and the two resulting independent histograms are shown together. The independent runs allow us to roughly characterize the uncertainty in the estimated probability distribution by simply inspecting the vertical spread in the results.

Detailed exploration of the tail of a probability distribution, as shown in Fig. 19, can be interesting in its own right, for instance to detect multimodality, or otherwise explore the state-space for rare but important events. We are also interested in using the high resolution characterization of the tail of the P2 distribution as leverage with which to facilitate estimation of the *mean* time to the production of five P2 molecules. The target of five P2 molecules was chosen to represent a modest but non-trivial level of P2 production.

To extract information about average P2 production time from short simulations, we work in a steady-state framework, as described in the Methods section. Using this methodology, we are able to infer the mean time to the creation of five P2 molecules, a relatively long timescale, from a weighted ensemble of short simulations. Shown in Fig. 20 is probability flux arriving at the target state of five P2 molecules at each WE iteration, as well as a running average of those instantaneous measurements, made using the most recent half of the data up to that time. When the system reaches a steady-state, the inverse of the probability flux into the target state, shown for on the right vertical axis of Fig. 20, is equal to the mean time to reach the target state. In Fig. 20, we see that the estimated time to the production of five P2 molecules is on the order of 5,000 seconds. This estimate will converge, within stochastic noise, to the true MFPT of the system when the flow of probability induced by the recycling process has relaxed to a steady state; see the Methods section

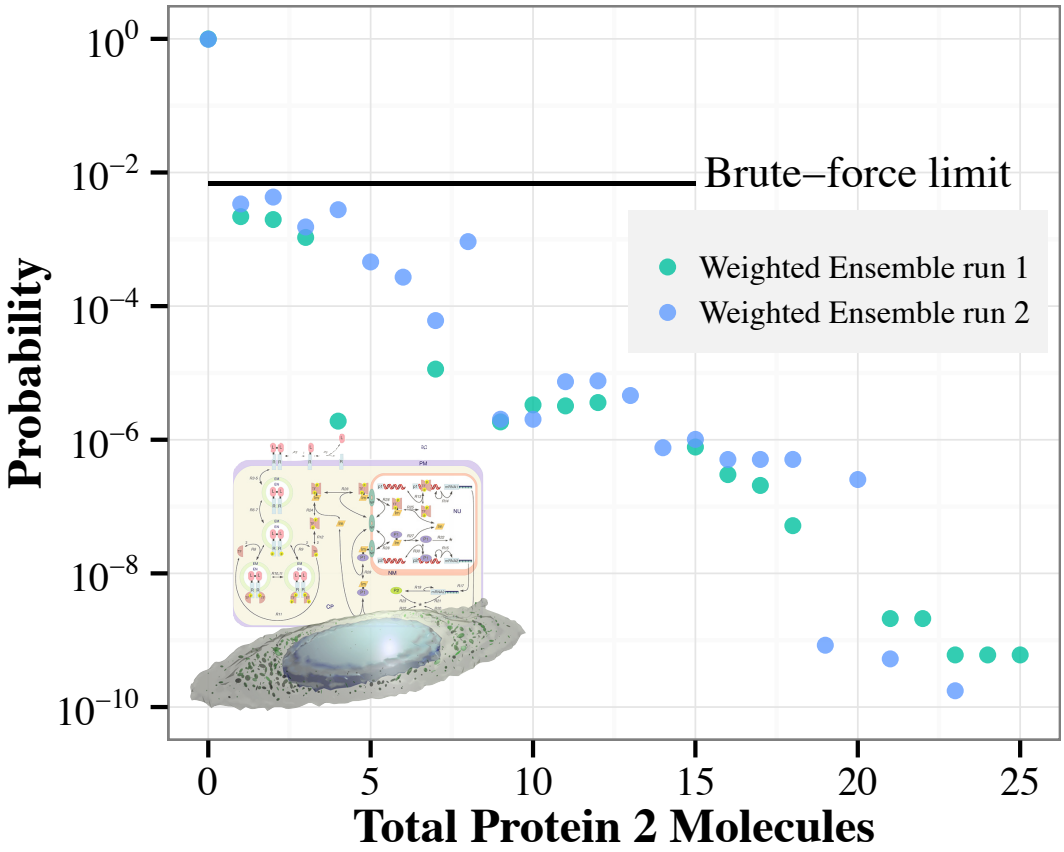

Figure 19: **Accelerated Sampling of High P2 Levels.** After 400 simulated seconds (~1 week of wall time for one trajectory), we plot the histogram of the number of P2 molecules in the cell. The blue and green circles are the result of two independent weighted ensemble simulations. Note that some data points are missing, because not all weighted ensemble bins are necessarily populated by trajectory segments at all times.

for details.

Although WE is extremely efficient at characterizing the P2 distribution (Fig. 19), its performance for estimating the MFPT is not exceptional in this case. The two WE runs require 31,328 seconds (run 1) and 27,408 seconds (run 2) of aggregate simulation to reach the relatively steady estimation shown in Fig. 20 at $t = 400$ seconds. By comparison, to obtain five to ten events for estimating the MFPT by brute-force sampling would require ~25,000 to ~50,000 seconds based on the estimated MFPT of ~5,000 seconds. Note that such long runs would not be able to benefit from parallelization.

The efficiency of the steady-state approach to measuring the mean first passage time depends on the time to convergence, and the noise of the sampling, once converged. The noise of the sampling can be reduced by a more densely sampled weighted ensemble, but the time to convergence is more difficult to characterize. In the approach used here, the latter timescale depends on the waiting time to typical transition events (e.g. about 200 seconds in Fig. 20), and the time it takes the system to relax to a steady-state. If these timescales (multiplied by the number of WE trajectories) are close to the timescale of the mean first passage time, then the estimate may not be particularly efficient. It will, however be less variable than a brute-force estimate of equivalent sampling power, and more convenient, in that it explores events of very different likelihood, and efficiently explores the state-space while estimating a key observable.

3.4.3 Time Dependent Kinetics: Neuromuscular Junction

Finally, we apply weighted ensemble sampling to a model of the active zone of a frog neuromuscular junction. This system, shown in Fig. 17, and described in detail in the Models section, simulates the dynamics of vesicle fusion in the presynaptic terminal. The MCell model used in this study is identical to the one described previously [131]. Briefly, calcium molecules are released into the active zone, and are free to diffuse and bind to the calcium binding sites on the synaptic vesicles in response to an action potential. When enough calcium binds to a vesicle in the proper arrangement, the vesicle is considered to have fused.

Calibrating and validating the response of the model against experimental data is of crucial importance, but at low calcium concentrations, it becomes highly inefficient to perform brute-

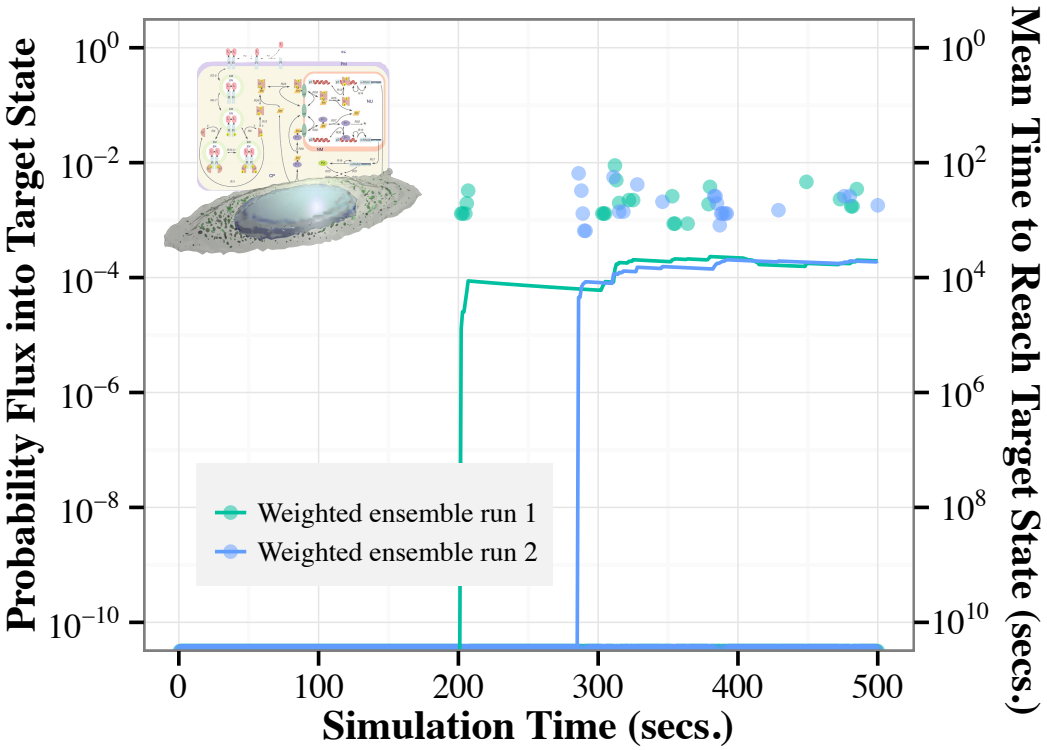

Figure 20: **Steady-State Estimate of Time to Produce Five P2.** The last event in the complex signaling network of Fig. 16 is the production of P2. Using a steady-state approach, weighted ensemble is able to estimate the mean time to producing 5 molecules of P2 as approximately 5,000 seconds. The graph shows the probability flux arriving at the target state (left axis) in each iteration (points), and a running average of that flux computed from the most recent 50% of the data (lines). The mean time to reach the target state (right axis) is obtained via the Hill relation (Eq. 3.1), as the inverse of the steady-state flux. Note that during most iterations, zero weight reaches the target state, as evidenced by the nearly continuous band of points at the bottom of the figure. The running average of the flux is dominated by these uneventful iterations, and hence is less than the nonzero instantaneous values.

force simulation to gather good statistics. In the neuromuscular junction system, the probability of vesicle fusion depends on the external calcium concentration and falls off sharply as the calcium concentration is decreased.

Fig. 21 shows the distribution of times to first fusion in the model, or first passage time (FPT) distribution to fusion, when the external calcium concentration is 0.5 mM and 0.3 mM. At each concentration, we plot the averaged results of 100 weighted ensemble runs, each of which was performed as specified in the Models section, as well as the averaged results of brute-force simulations, which in total required the same computational effort to simulate as the 100 weighted ensemble simulations (7545 brute-force simulations for the 0.3 mM system, 3513 for the 0.5 mM system). The difference with which the two approaches – weighted ensemble and brute-force – are able to capture the shape of the distribution, and the uncertainty in the estimation of it, is striking. We are unaware of any definitive methods of estimating error when the sample yield is extremely low, and hence have omitted error bars when only one or two samples were obtained.

At low calcium concentrations, the overwhelming majority of simulations do not result in a vesicle release, which is why brute-force sampling is so ineffective. Notice that the total area (i.e. the total probability of vesicle fusion) in the histogram for the 0.3 mM condition is only on the order of 10^{-4}. One would have to perform on the order of $100/10^{-4} = 10^6$ simulations to start gathering meaningful statistics (100 samples) with which to compute the fusion time distribution. This amount of computing (~20 years running in serial, if each simulation only takes a minute, or ~20 weeks, running in parallel on a 48-core machine) is unfeasible to perform even once, let alone at all the different settings of model parameters of interest. Using weighted ensemble, however, it becomes practical to sample this model in the low-calcium regime, providing critical information for model validation and fitting purposes. The weighted ensemble sampling for the 0.3 mM condition shown in Fig. 21 took time equivalent to 7545 brute-force simulations, and runs in matter of hours in parallel on 48 cores.

Fig. 22 summarizes NMJ results at five different experimentally relevant calcium concentrations. The data are a striking recapitulation of an experimentally demonstrated power-law dependence of probability to fuse as a function of calcium ion concentration [162]. Validating the model in low calcium regimes has been intractable with traditional sampling approaches. Using weighted ensemble, we are able to sample the model at all concentrations of interest.

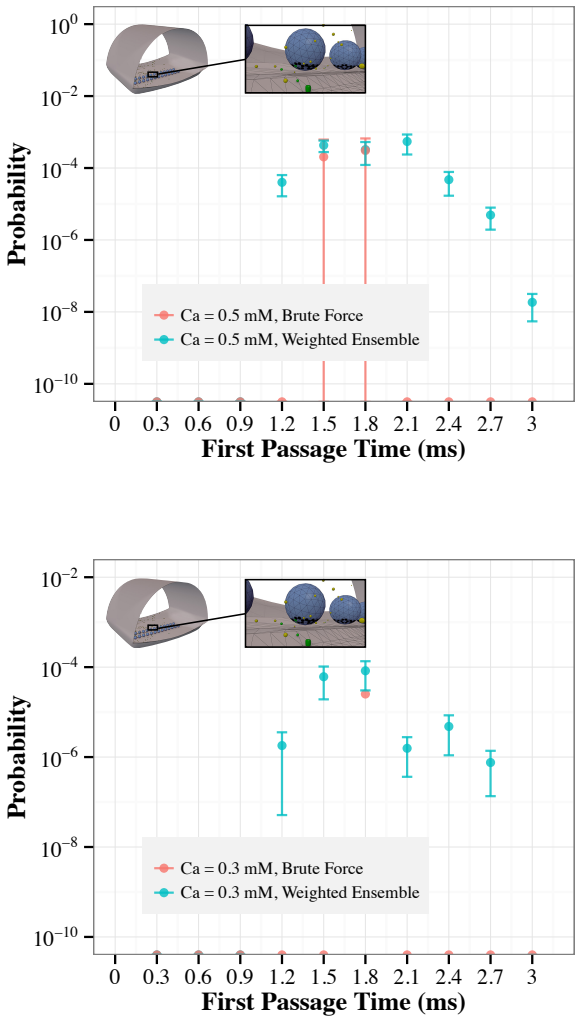

Figure 21: **Enhanced Sampling of the First Fusion Time Distribution in the NMJ Model in Low Calcium Conditions.** Shown are measurements of the first fusion time distribution for calcium concentrations of 0.5 mM (left), and 0.3 mM (right). In both plots, weighted ensemble estimate of the distribution of first fusion times for the NMJ model (blue), are compared to brute-force estimates (red) made using the same computational power as the weighted ensemble estimate. Points at the bottom of the plot indicate no fusion events in that time period. Single points with no error bars indicate only one sample, yielding no ability to estimate uncertainties. Brute-force sampling sees very few events, and gives a poor estimate of the shape of the distribution and yields poor confidence intervals (it is unable to exclude zero from any time point at one standard error). Weighted ensemble is able to capture the shape of the fusion time distribution, as well as providing good estimates in the uncertainty of the measured values.

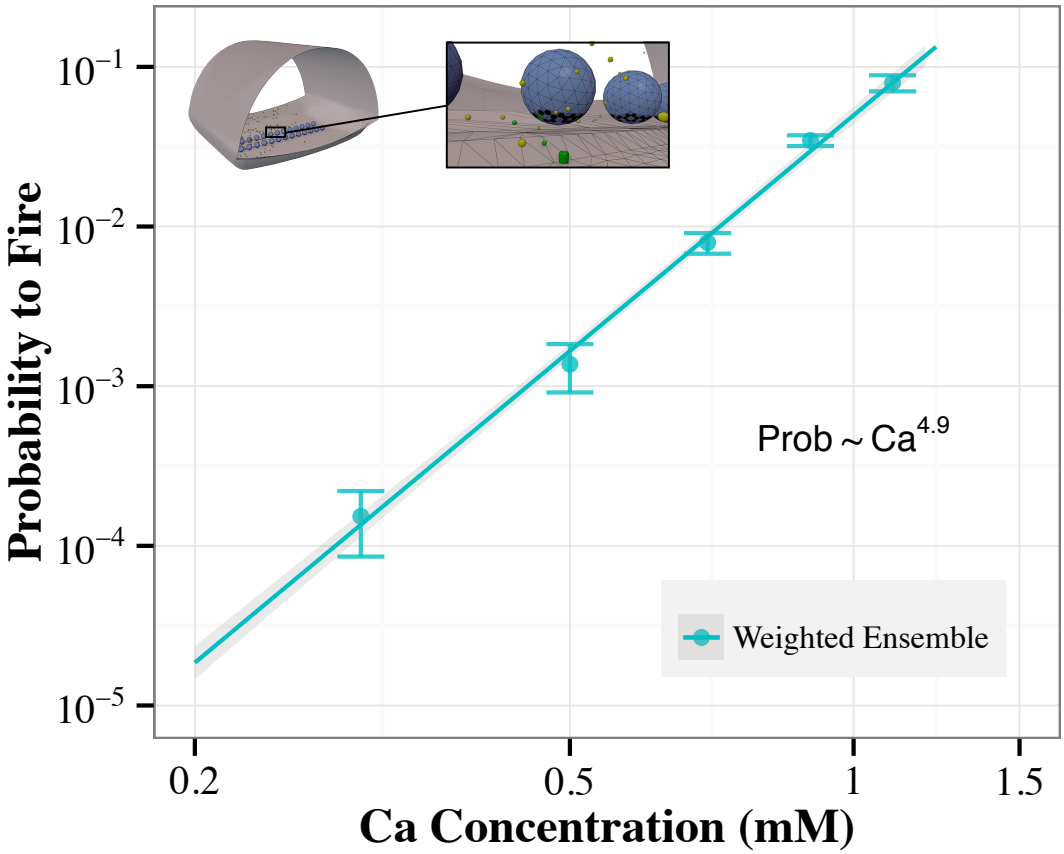

Figure 22: **Verification of Empirical Fusion Rate Law Extended to Low Calcium Regime.** The probability for the model to release a synaptic vesicle in the simulation window is plotted vs. the calcium concentration in the simulation. Weighted ensemble is able to efficiently estimate these probabilities in the low calcium regime (0.5 mM and below). WE data points and the power-law fit are shown with 1-σ confidence intervals.

3.5 DISCUSSION

Spatial models of stochastic reaction-diffusion processes have found widespread use as tools in understanding the mechanics of biological processes on the cellular level and beyond [163, 164, 165, 166, 167]. Unfortunately, the effective sampling of large, realistic models, and the extraction of well-sampled values of experimentally relevant quantities are often beyond the realm of computational feasibility. We use a weighted ensemble approach to overcome this impediment and demonstrate speedups of orders of magnitude in sampling some observables in complex models of cellular behavior with spatial dependence. Weighted ensemble is an ideal approach to employ in addressing the issue of difficult to sample stochastic systems, and because of its efficiency and ease of use, we anticipate many further applications.

3.5.1 Strengths and Weaknesses of WE

Weighted ensemble is one of many enhanced sampling methods, and one of a smaller number that provides rigorous kinetics [46]. However, WE stands out from comparable approaches in its modularity, flexibility, and ease of use. Because weighted ensemble only performs resampling at fixed time intervals, and only when a trajectory transitions from one state-space bin to another, there is no need to catch trajectories in the act of crossing a state-space interface. This facilitates the implementation of weighted ensemble as a lightweight "wrapper code" around any number of simulation engines. A weighted ensemble approach also parallelizes trivially, as all trajectories are uncoupled while running, and are only compared intermittently during resampling. This efficiency in scaling has been demonstrated on simulations using over 2000 cores across many nodes on the Ranger supercomputer [136]. Additionally, a weighted ensemble of trajectories always follows the exact dynamics of the system; no biasing potentials, altered rate constants, change of measure, or other "hands on" tactics are necessary for efficient sampling.

A significant benefit of the WE approach is the ability to quickly find behaviors of a system that are very rare, or to detect the presence of multiple stable states of a system with high crossing barriers. As seen in our study of the cellular signaling model in a realistic geometry, efficient sampling via WE permits estimation of previously unknown long timescales using short simulations.

All unbiased enhanced sampling methods that sample systems preferentially along a set of progress coordinates, including weighted ensemble, are useful only insofar as the state space has been divided along progress coordinates sufficient to characterize processes of interest. This limitation amounts to employing all of the slow, uncorrelated, degrees of freedom in the system as progress coordinates. Fortunately, an exhaustive use of all slow degrees of freedom is not required, as most will be correlated, and thus redundant descriptors of slow processes. Hence a "curse of dimensionality" does not cripple these approaches, and exists only to the extent that a system has important slow degrees of freedom which are uncorrelated with binned coordinates, but sufficient sampling is never guaranteed.

Sampling coordinates orthogonal to the progress coordinate will, by definition, not happen at an enhanced rate, which places a lower limit on the shortest useful simulations that can be performed. For instance, the toy model we investigate has only one effective degree of freedom, and displays an enormous amount of speed-up in sampling along this coordinate, because there are no slow orthogonal degrees of freedom being sampled on a slow, "native" timescale. On the other hand, the signaling model in the realistic cellular geometry shows less enhancement, a factor of about 10^5 in sampling large amounts of P2, and less than that in estimating the mean time to production of five P2. This is because there are degrees of freedom in the system orthogonal to our progress coordinate that must relax to steady-state at an unenhanced rate, a process which occurs on a timescale uncoupled to weighted ensemble resampling.

A potential difficulty is that of correlation between trajectories. Since most WE trajectories share some history by construction, judging the degree to which related trajectories are independently sampling the space requires special care [45, 48]. Estimating observables within a single WE run requires careful consideration of time correlation. Alternatively, as in the present study, multiple independent WE runs directly provide unambiguous information on statistical uncertainty.

Weighted ensemble is not guaranteed to enhance sampling for all observables. In essence, WE will be most useful for the observables that occur with low probabilities on the time scales of interest. For less challenging quantities, such as the mean first passage time of Fig. 20, or the high calcium concentrations of Fig. 22, WE may primarily offer the advantage of simple parallelization.

3.5.2 Summary and Outlook

The multi-scale modeling problem posed by constructing accurate, physically realistic models of cellular level processes is considerable. We have demonstrated the utility of sampling spatially inhomogeneous stochastic simulations of cellular processes using a weighted ensemble (WE) approach. Although WE cannot estimate every quantity with high efficiency, estimates for some observables were obtained using orders of magnitude less overall computing than would have been required with conventional parallelization. We hope that these initial results will facilitate the study of more realistic and physically accurate spatial models of biological systems. As an ambitious example, integrating spatial models of stochastic processes with microscopy data of protein localization to predict phenotypic response to the perturbations of interactome networks is an attractive prospect for in silico drug development and personalized medicine. Currently, the bottlenecks in such a scheme are the lack of accurate models and the computational resources with which to simulate them. We hope that this work will contribute to the development of truly physiological computational models.

3.6 SUPPORTING INFORMATION

4.0 GRAPHICAL MODEL FREE ENERGIES OF PEPTIDES AND PROTEINS

4.1 INTRODUCTION

There is immense interest in the computational estimation of biomolecular free energies, for purposes ranging from drug-design to the understanding of fundamental biology [63, 168, 169, 170, 171, 172, 173]. Unfortunately, calculating these free energy estimates is incredibly computationally intense using traditional means such as molecular dynamics [174, 175, 176, 177, 178].

A popular alternative to time consuming simulation-based approaches such as molecular dynamics is to compute a free energy of binding using an empirical scoring function [179, 180]. Scoring-based methods focus on protein-ligand interactions, and are fast enough to be suitable for screening studies [181, 182], but since they do not sample the full configurational space of the system, they have difficulty estimating the entropic contributions to the free energy [183, 184, 185, 186, 187, 188].

Also of note is the polymer growth technique for estimating free energies, a stochastic algorithm that is statistically exact when well sampled. Polymer growth free energy estimates employing fragment-based libraries were used in previous work by Zhang, Mamonov, and Zuckerman [195] and Lettieri, Mamonov, and Zuckerman [196] to estimate the free energies of peptides. The polymer growth approach has trouble scaling beyond modest peptide length, but gives excellent statistics for free energies when enough samples are used in the computation. Where brute-force methods are intractable, I employ polymer growth estimates of the free energy as reference standard.

Over the past few years, work by Langmead and coworkers has established the use of graphical models as an attractive alternative to both simulation-based methods or scoring functions [54, 55, 56, 57, 58, 59, 60, 61]. Their work using loopy belief propagation on pairwise Markov Random

Fields achieves impressively accurate estimates of protein conformational entropies and binding free energies at orders of magnitude lower computational cost than simulation-based methods [54, 57].

In this chapter I explore an intriguing question raised by the work of Langmead and coworkers, of how BP free energy estimates behave as the number of states used to build the Markov Random Field is increased. I also provide some minor insight regarding how the state-space of these model can be sampled, and some exposition, from a statistical physics point of view, of the origin of the logarithmic correction term bridging the physical and Shannon entropies [57, 189]. I also take the opportunity to compare the belief propagation free energy estimates to exact computations in a subset of models, and confirm prior assessments of the accuracy of belief propagation[64, 57].

There are two main concerns with using belief propagation: on graphs with loops, the algorithm may not converge, and if it does converge, it is not guaranteed to converge to the correct marginal probability distribution. Extensive work has been done investigating the accuracy and convergence of loopy BP and its variants [64, 190, 68, 191, 67], including the use of upper and lower bounds based on mean-field and tree-reweighted variations of BP and their application in the realm of protein structure [55, 192]. As a compliment to these approaches, instead of bounding the worst case performance of belief propagation, I compare the belief propagation approximation of the free energy to exact methods for some particular examples, and observe that in physically realistic situations, the agreement between the two is striking.

Instead of using the backbone-dependent Dunbrack side-chain libraries [193] as in prior work [57], I generate my own side-chain conformations sampled on a uniform grid in dihedral space. The Dunbrack side-chain libraries contain 3 states per χ-angle degree of freedom, optimized to represent the low energy side-chain conformations as observed in the protein data bank. To more densely and evenly sample the configurational space, I generate my own side-chain conformations by sampling the side-chain dihedral degrees of freedom on a uniform angular grid. Sampling states on a uniform grid has the benefit of being manifestly statistically exact, facilitating rigorous statistical mechanics calculations at different sampling densities, while using weighted samples presents difficulties, as discussed in Appendix B. There is also compelling evidence that as the number of samples is increased, uniform sampling provides startlingly fast rates of convergence for integrating periodic functions similar to those in the MRFs under investigation here [194].

In the context of modeling peptides and proteins, the accuracy the free energy of a Markov random field varies as a function of both the density of samples taken to construct the MRF, and the algorithm used estimate its free energy. Unfortunately, a comprehensive survey along both of these dimensions for each model I investigate is prohibitive, due to the exorbitant run-times of the statistically exact free energy methods. Instead, I use an iterative approach, first taking advantage of the speed of belief propagation to get a sense for what an appropriately dense sample space is, and then working in that regime of sample density to investigate more complex models where comparisons to exact free energies is arduous but feasible to compute for a small set of models.

4.2 OVERVIEW OF GRAPH GENERATION

The Markov random fields (MRFs) used to encode the protein or peptide structure are composed of a graph, and potential functions on the nodes and edges of that graph, as illustrated schematically in Fig. 4, and explained in Chapter 1. A high level overview of the construction and use of the MRFs in this work is depicted in Fig. 23.

4.2.1 Choosing Edges

The connectivity of the graphs in the MRFs specifies which residues in the peptide/protein (which are nodes in the graph) directly influence the state of other residues. In a maximally dense graph, all nodes can influence all other nodes, though in practice, constructing such graphs is undesirable and unnecessary. Putting an edge between nodes in the graph that represent residues in the structure which are very far apart alters the properties of the graph only minutely, since the interaction energies of residues that are far apart are so weak. As discussed below and in [54, 57], including edges between nodes only when the connecting node is within a specified distance is a reasonable approximation. I use the distance between α-carbons of the residues as the input to my cutoff criteria. Other, more sophisticated cutoffs are possible, for instance longer cutoffs for the residues that are physically larger, but I have found that an α-carbon cutoff distance of about 0.8–1.0 nanometers is appropriate for the systems I consider here. Another reason for restricting the number of edges

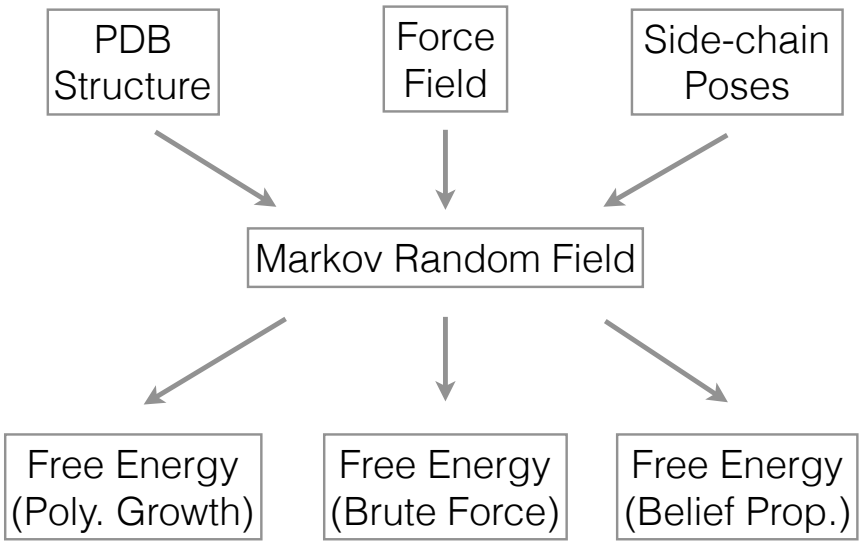

Figure 23: Graphs are constructed from a PDB structure, with node states specified by a set of poses per side-chain, and node and edge energies given by the Amber99SB forcefield. Once the graph is constructed, the free energy and other statistics can be computed by a variety of means. Here we apply belief propagation, and compare its performance to brute-force and polymer growth.

in a graph is that since constructing the interaction energy tables for the edges of the graph is a bottleneck for the process, keeping the time spent on unimportant edges low is desirable from a practical point of view.

In my work, the graph is constructed from a PDB structure file, based on a C_α-distance cut-off. Once the connectivity of the graph is determined, the potentials in the MRF are constructed according to how many states each node (i.e. residue) can take.

4.2.2 Node States from Dihedral Degrees of Freedom

Since the backbone is fixed for each graph, the state-space of each node, and thus the graph as a whole, is in turn determined by the states each dihedral angle in each node can take. The convention that I follow is that each dihedral angle in a residue is allowed to take a set number of states k, evenly sampled around a full rotation of that angle. This number k is the same for each dihedral angle in each residue, though in theory this does not necessarily need to be the case. This uniform sampling does have the advantage of simplifying the free energy formula; non-uniform sampling would entail some form of unweighting the samples back to a uniform distribution in order to compute the correct integrals. This issue is discussed in more detail in Appendix A.

Dihedral angles involving only heavy atoms are treated slightly differently than dihedral angles involving terminal methyl groups. Since the methyl groups possess a three-fold symmetry, they only need to be rotated through one third of a full rotation in order to sample all conformations uniformly. This is consistent with the convention that the contribution to the partition function of symmetrically indistinguishable states is reduced by a factor given by the symmetry.

Although uniform sampling in dihedral space guarantees correctness of the partition function/free energy, it does entail a high cost for residues with a large number of dihedral angles. For instance, computing ten states per dihedral angle is quite quick for a residue with only one dihedral angle, but for a residue with four dihedral angles, ten states per angle means computing 10^4 states for that residue. Computing the energies for 10^4 states takes a while, but the computational cost is tolerable; the real cost is in computing the pairwise energies for the edges in the graph between these large nodes. If two nodes have 10^4 states each, the edge between those nodes has 10^8 pairwise combinations of states, and computing ten billion states for each such edge is not feasible in

my implementation.

Since this work is largely exploratory, the solution we took to the state-space problem was to avoid using pdb structures with residues containing too many dihedral angles. In practice, the residue with the largest state space that I was able to use was Leucine, with two heavy atom dihedrals and two methyl group dihedrals. Sampled at a density of about 10 states per heavy atom dihedral and 2–3 states per methyl group dihedral, yielding about 500 states for the nodes and 25,000 states per edge between two Leucines (computing such edges took on the order of hours to days).

4.2.3 Node and Edge Potentials

To compute the node and edge potentials of the Markov random field, it is necessary to be able to manipulate protein structures, and evaluate the potential energies of the structures in different conformations. The other necessary ingredient is the ability to "turn off" or "ignore" large portions of the structure, and only evaluate the energetics of one or two residues (for nodes and edges respectively. Once the energy for a conformation is computed, the Boltzmann factor of the energy gives the element of the potential function. All Boltzmann factors in this work are computed at 298 K.

To calculate the potential for a single node, the residue corresponding to that node is manipulated to take on all desired conformations (which is a set number per dihedral degree of freedom), and at each of these conformations, the potential energy contributions from atoms only in that residue are tabulated. The Boltzmann factor of these potential energies is then the node potential.

The computation of the potentials for the edges is only slightly more complicated. All pairwise combinations of conformations for the two residues must be considered, recording the potential energy contributions from all atoms in both residues. Importantly, these potential energies must be modified by subtracting off the contributions internal to each node, leaving only the energetics arising from inter-residue interactions. After determining the inter-residue potential energy for each pairwise combination of residue conformations, the Boltzmann factor of that energy is taken, and this matrix is the edge potential.

Since determining the potentials on the Markov random field involves selectively ignoring

large portions of the structure, sophisticated solvent models are not easily applied. In our studies, we used a uniform (relative) dielectric constant of 60.0 as a simple solvent model, as in [195].

The time spent generating the edges of the MRF between nodes with a large number of states is the primary bottleneck in the process of extracting a free energy from the graph; the belief propagation algorithm itself runs in s small fraction of that time. I was able to take some rudimentary steps towards mitigating that bottleneck, though since the emphasis of this work not on the efficient construction of the graphs themselves, it was not a strong priority. Since the calculation of each edge and each node potential can be performed entirely independently of all other nodes and edges, the process parallelizes trivially, and my Python implementation does take advantage of this fact to run the graph construction in parallel on up to 48 cores. I also note that the energy calls and geometric manipulation routines I employed for tabulating the potentials were through a Python interface (OpenMM), and thus very slow compared to, say, the optimized code used in most MD engines. While this led to slow graph generation times in my case, there is no reason why a more optimized implantation could not mitigate this issue, especially considering the parallelizable nature of the task.

4.3 OVERVIEW OF FREE ENERGY CALCULATIONS OF GRAPHS

4.3.1 Brute-Force

The natural point of comparison in evaluating the accuracy of the belief propagation approximation to the partition function is to compare to the exact value, though this is only feasible in certain limited cases. When this gold standard of comparison is practical, I employ a brute-force calculation of the free energy via an exponentially large sum over the partition function, a simplified version of which is shown in listing C.1. This approach is simply a naïve sum over an exponentially large number of terms, and is only practical when the graph has very few nodes, and few states per node (in practice, ~5 nodes, and ~10–100 of states per node). The log of this partition function then gives the free energy as in equation A.28.

4.3.2 Polymer Growth

In more ambitious situations, I employ a "bronze standard" of a polymer-growth estimate of the free energy. The polymer growth algorithm proceeds by sequentially adding nodes and edges to a graph, until it is fully constructed. After each node is added, the change in the free energy of the graph due to the addition of that node (and all its incident edges) is computed. After all the nodes and edges have been added, the sum of these changes in free energy is found to be the total free energy of the MRF.

Polymer growth has been previously applied to small systems, such as peptides of length ~10 residues [195, 196] in the considerably more challenging setting of a totally flexible backbone. Details of the method can be found in [195, 196], though I will briefly sketch out the procedure as implemented in my work, a simplified version of which is detailed in listing C.2. The procedure is illustrated schematically in Fig. 24. The polymer growth free energy estimates are a necessary point of comparison in quantifying the accuracy of belief propagation, because brute-force calculations are not feasible in systems of even modest size.

Whereas both the brute-force and the belief propagation calculations are deterministic, the polymer growth procedure, as I have employed it, is a stochastic algorithm. This is because after each node is added, and the free energies are computed, the number of states of the graph retained for estimation purposes is down-sampled randomly according the Boltzmann factor of the energy of the state of the graph. Another point of difference is that as opposed to end-point methods like brute-force and belief propagation, polymer growth is a perturbative algorithm, which estimates of the free energy of the graph by iteratively adding nodes to the graph and computing changes in free energy.

For example, I might start with an empty graph, and add a node to it containing 1000 states. After computing the energy of each state, and finding a free energy difference from the empty graph (taken to have a free energy of 0) via a sum of Boltzmann factors, the state-space is then down-sampled to a smaller number, say 50. In the next round of growth, when I add another node, with say 200 states, I would then calculate the energies of each pairwise combination of old global configurations of the graph (the ones I down-sampled to last time) with all the new states, so in this case 50×200. In this manner, the combinatoric explosion of state combinations is avoided, and

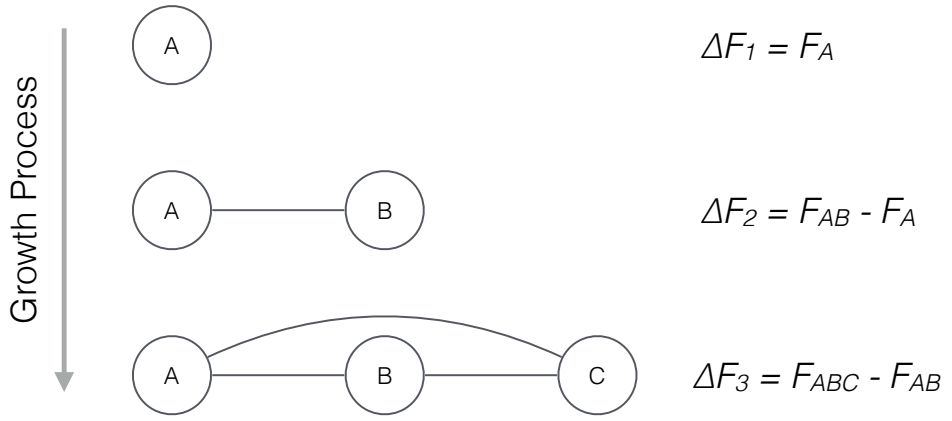

$$F_{tot} = \Delta F_1 + \Delta F_2 + \Delta F_3$$
$$= (F_{ABC} - F_{AB}) + (F_{AB} - F_A) + (F_A)$$
$$= F_{ABC}$$

Figure 24: Polymer growth procedure for a graph with three nodes. Nodes are added successively, and at each step the free energy is computed from an ensemble of states sampled in the previous step. The total free energy is then calculated using the sum of the free energy differences tabulated during the growth process.

one only pays a cost proportional to the size of the state-space of the individual nodes, multiplied by the number of nodes to which one down-samples.

However, a further cost is also due: since the algorithm is stochastic, one must perform multiple runs in order to obtain converged estimates of the free energy. A last caveat of the polymer growth estimate is that as noted in [197], at finite sample-size, a nonlinear estimate such as for the free energy is confounded not only by random noise but by systematic bias. This systematic bias is difficult to predict; in practice I kept increasing the number of states retained until the estimate of the free energy stabilized.

4.3.3 Belief Propagation

Belief propagation [198] is an algorithm for efficiently computing the exact free energy on graphs without cycles. Unfortunately, cycles (or "loops") are essential to modeling the interactions between multiple neighboring amino acids in a folded structure. The variant of Pearl's algorithm [199] that I employ, loopy belief propagation [64], essentially iteratively applies the belief propagation algorithm even though it has no guarantee of working "correctly". However, it has been shown [200], that this naïve procedure, when it converges to a stable estimate, is in fact identical to the Bethe approximation [201, 202] of the free energy, a well-known method in statistical physics. The Bethe approximation of the free energy comes with no strict guarantees of accuracy in loopy graphs, and the convergence of the algorithm in the general case is still an open problem. However, there is evidence that graphs representing protein structure may be significantly more tractable for the BP algorithm than a hypothetical worst case [57].

4.3.3.1 Message Passing The (loopy) belief propagation algorithm algorithm that I implemented is given in listing C.3.

At a high level, the algorithm passes messages around a graph until they stop changing. The messages are sent from nodes to their neighbors, and convey each node's belief about what state it thinks its neighbors should be in.

The way in which these beliefs are calculated is fairly straightforward. The messages (or node beliefs) all are initialized to the uniform distribution, i.e. if a node has k states, the node belief is set

to $1/k$ for each state. Other initializations are possible, but in practice using random initializations had no discernible effect. In each round of belief propagation, messages are sent from each node to all of its neighbors (thus $2E$ messages are sent each round, where E is the number of edges in the graph).

Each message from a sending node to a receiving node is computed as follows. The node sending the message, n_s, initializes its message as its node potential, which is a vector of length k_{n_s}. The node then looks for all of its neighbors that aren't the node receiving the message, n_r. From each of these neighbor nodes, the sending node gathers all messages incoming to it. These incoming messages are all of the same length k_{n_s}, where k_{n_s} is the number of states of the sending node. The sending node then takes those incoming messages, and multiplies them in an element-wise fashion, to construct a sort of vector version of the geometric mean of the incoming messages. Once the sending node has collated the incoming messages by multiplying them together, it is ready to send a message of its own to the receiving node, by taking this collated message and multiplying it by the edge potential between itself and the receiving node. This edge potential has dimension $k_{n_r} \times k_{n_s}$, where k_{n_r} and k_{n_s} are the number of states of the receiving node and sending node, respectively. Since the outgoing message from the sending node is of length k_{n_s}, and can be though of as a column vector, the matrix multiplication of the edge potential and the column vector results in a new vector of length k_{n_r}. This product is then normalized, and can be thought of as a probability distribution over k_{n_r} states. This is the final message that is sent to the receiving node; note that it has the same length as the number of states in the receiving node. This process of gathering incoming messages, processing them, and sending outgoing messages is iterated for each node in the graph, and then the process starts over again if the messages haven't stopped changing.

The message passing process is terminated if the messages are within a threshold distance of what they were in the previous round of belief propagation. In particular, for each message I took the sum of the absolute differences of each message, and then took the sum of those sums to define a global change in all of the messages. If that global change was less than a threshold value, the belief propagation was considered to have converged. The default value of the threshold I used was 10^{-12}, which I considered to be fairly stringent. The stringency of the stopping condition can be put into context by noting that each message is a probability distribution over $1/k$ states, and

thus always has an entry of size greater than or equal to $1/k$, and k was never more than about 10^3.

4.3.3.2 Computing Final Beliefs Once the set of messages to and from all the nodes has converged, the beliefs of each node and edge can be computed, and used to approximate the free energy of the Markov random field. Formally, these beliefs are the marginal probabilities of the nodes or edges.

The node beliefs are computed in a manner almost identical to that of the message passing algorithm, with one slight difference. Since there is no receiving node in this computation of a single node's marginal probability, the incoming messages from all the node's neighbors are used, and none are omitted. Otherwise, the process is identical: the node belief is initialized as the node potential, and then messages from all neighbors are multiplied together element-wise, with the node potential, and the resulting vector is normalized.

Computing the edge beliefs is similar, but slightly more complicated, since there are two nodes contributing beliefs to each edge belief. Say the edge in question, e_{ab}, connects nodes n_a and node n_b. Then the edge belief is initialized as the edge potential ϕ_{ab}, which is a matrix of dimension $k_{n_a} \times k_{n_b}$, where k_{n_a} and k_{n_b} are the number of states in nodes k_{n_a} and k_{n_a}, respectively. Once the edge belief is initialized, the messages from all nodes incident to nodes n_a and n_b are collated, as in the message passing algorithm. That is, for node n_a, messages from all its neighbors other than n_b are multiplied together and then normalized, and similarly for node n_b, omitting the message from node n_a. These modified node beliefs for n_a and n_b are then combined in an outer product, forming another matrix of size $k_{n_a} \times k_{n_b}$. This matrix is then multiplied element-wise by the edge potential. If $\mathbf{x}_a$ and $\mathbf{x_b}$ are the beliefs in the states that nodes n_a and n_b take, this element-wise matrix multiplication can be thought of as evaluating a normalized version of the node potential for these states $\phi_{ab}(\mathbf{x}_a, \mathbf{x}_b)$.

4.3.3.3 Computing Free Energies from Beliefs The free energy of the Markov random field is computed by separately computing the entropy and average energy of the graph. In turn the nodes and edges contribute independently to the entropy and average energy. Let ϕ_n be the node potential of node n, and b_n the node belief, and similarly for the edge potentials ϕ_e and b_e. As a reminder, the beliefs b_n and b_e are the final estimated marginal probability distributions for the nodes and

edges, respectively. Then the formula for the contribution of nodes to the average energy is

$$\langle U_{\text{nodes}} \rangle = -k_B T \sum_{n \in \text{nodes}} b_n \cdot \log \phi_n \tag{4.1}$$

where the log is taken element-wise, and "$\cdot$" indicates a dot product. Similarly, the contribution of edges to the average energy is

$$\langle U_{\text{edges}} \rangle = -k_B T \sum_{e \in \text{edges}} b_e \cdot \log \phi_e \tag{4.2}$$

The total average energy is then simply

$$\langle U_{\text{total}} \rangle = \langle U_{\text{nodes}} \rangle + \langle U_{\text{edges}} \rangle \tag{4.3}$$

Appropriately enough, these formulae can be interpreted as taking the expectation of the energy, since

$$\phi_i = e^{-E_i / k_B T} \implies E_i = -k_B T \log \phi_i \tag{4.4}$$

and summing over the dot product of this quantity with the beliefs is precisely taking its expectation with respect to the probability density given by the beliefs.

Computing the entropies is similar to computing the average energy, but instead of taking the expectation of the energies of the nodes and edges, we take the expectation of the log of the probability densities, or beliefs. Additionally, there is a somewhat subtle issue in estimating the entropy of a continuous system using a discrete number of samples that must be addressed. The formulae for the node and edge entropies are then

$$S_{\text{nodes}} = -k_B \sum_{n \in \text{nodes}} b_n \cdot \log b_n \tag{4.5}$$

where the log is taken element-wise, and "$\cdot$" indicates a dot product. Similarly, the contribution of edges to the average energy is

$$S_{\text{edges}} = -k_B \sum_{e \in \text{edges}} b_e \cdot \log b_e \tag{4.6}$$

However, as pointed out in [57], the naïve sum of these entropy terms is not the a valid estimate of the entropy of the system

$$S_{\text{naïve}} = S_{\text{nodes}} + S_{\text{edges}} \neq S_{\text{total}} \tag{4.7}$$

The correction factor due to discretizing the state-space turns out to be fairly simple: if every dihedral degree of freedom d in the graph is sampled using k samples,

$$S_{\text{Total}} = S_{\text{nodes}} + S_{\text{edges}} - d \log \frac{k}{2\pi} \tag{4.8}$$

This result is re-derived in appendix A, where the issue is addressed in more depth.

4.4 INTERACTIVE GRAPH VISUALIZATION

Visualizing the graphs in the Markov random fields is extremely helpful in evaluating the interactions in the model. Since the graphs for the Markov random fields are constructed from three-dimensional structures, standard two dimensional visualizations are not particularly informative. The approach I took was to instead just visualize the graph in three dimensions. Additionally, I found it useful to not only inspect the graph topology, but also the physical layout, by superimposing the graph on the physical structure it represents.

To accomplish a simultaneous visualization of the graph and biomolecule structure in three dimensions, I built on the open-source 3dmol.js framework, implementing a simple graph layout superimposed on a pdb structure. The visualization tool is web-based, and available at `http://pitt.edu/~donovanr/MRF_visualization_3dmol.html`. A screenshot of the web interface is shown in Fig. 25.

4.5 IMPLEMENTATION DETAILS

All three inference algorithms were implemented by me in Python. The graph construction routines were also implemented by me in Python, building on the NetworkX graph library and the Python interface to OpenMM. The MRFs are implemented as annotated undirected graphs using the NetworkX library in Python. Side-chain configurations are generated programmatically on an even grid in dihedral space, and the elements of the node and edge potentials are computed for each side-chain configuration using energy calls to OpenMM. The node and edge potentials are stored

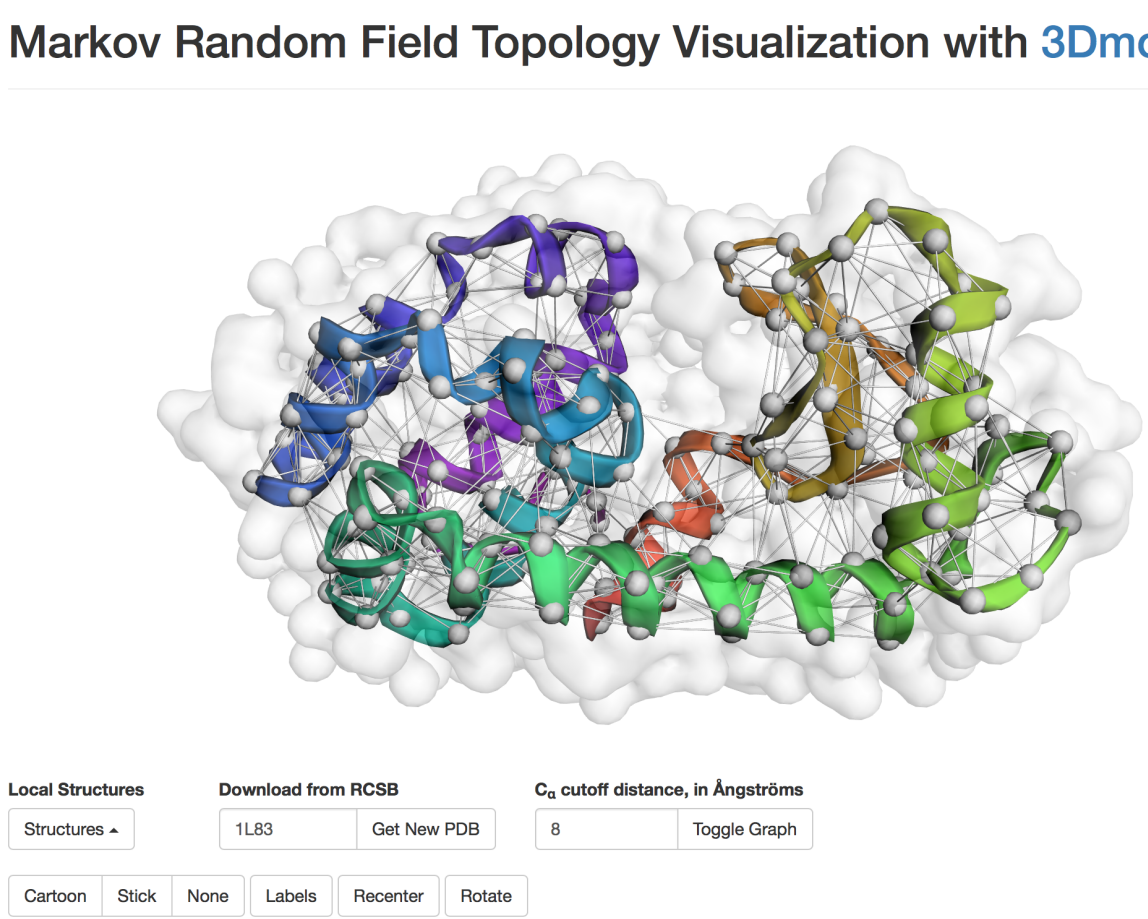

Figure 25: Web-based 3D visualization of the graph structure of the Markov random fields used in my computations. The interface allows the visualization of graphs for arbitrary pdb structures, with a user-determined cutoff distance between residues. The user is able to zoom, pan, and rotate the structure, as well as specify different visualization options.

as NumPy arrays and accessed as attributes of their corresponding node or edge in the NetworkX graph.

The graph visualization code was implemented by me in JavaScript, with the kind assistance of David Koes, building on his work on 3Dmol.js.

All code is available as source at http://gitlab.csb.pitt.edu/donovanr/protGM.

4.6 SYSTEMS AND RESULTS

4.6.1 Agreement of Belief Propagation, Polymer Growth, and Brute-Force Free Energies in a Simple Molecular System

When the systems are small enough to compute the free energy of the Markov random field by brute-force, it is straightforward to compare the performance of belief propagation to the gold standard of the brute-force value. However, most systems are too large to compute via brute-force, and in these situations, the belief propagation result needs to be validated against other methods. Here, I use the polymer growth approach, as described in section 4.3.2. Since the polymer growth algorithm is a stochastic algorithm, in this section I provide evidence that in a simple but realistic setting, BP yields results that are effectively identical with brute-force.

The test system I use to compare brute-force, polymer growth and BP is a threonine-4 peptide, which is the largest system for which I was able to calculate the free energy via brute-force. This peptide contains four threonines joined by peptide bonds, and capped at the C-terminus with N-methyl amide, and at the N-terminus with an acetyl group. I allow the peptide to relax and fold on itself, in order to mimic the potential for clashes in a real structure. After relaxing the structure for 1.0 nanoseconds, the structure is sampled as a single pdb file.

Once the test structure is determined, the graph is constructed using a fixed backbone, leaving only the side-chain degrees of freedom to vary. Each threonine has one heavy atom χ-angle dihedral degree of freedom, and one terminal methyl group dihedral degree of freedom. The capping groups each have one methyl group dihedral degree of freedom.

For this test system, I set the inter-residue cutoff to be 1.0 nanometers, which yields a fully

connected graph between six nodes. Each node was sampled at 11 states per heavy atom χ-angle dihedral degree of freedom, and 3 states per methyl group dihedral degree of freedom. This results in four nodes with 33 states, and two nodes with 3 states, as well as one edge with 9 states, eight edges with 99 states, and six edges with 1089 states. For reference, the naïve size of the state space (as in brute-force) is thus $33^4 \cdot 3^2$, or about ten million states.

This graph is the largest for which I was able to obtain a brute-force estimate of the free energy. The Brute-force value I obtained was 176.49554277, in units of k_BT. I report these values to an excessive number of decimal places: not because they are physically relevant to this level of detail, but because *in this model* (as we will see), the agreement between brute-force and belief propagation is so accute.

This system was also useful for validating the accuracy of the polymer growth estimate of the free energy. In using the polymer growth algorithm for this graph, I set the number of states kept in each round of growth to be 100, and also performed 100 independent repetitions of the growth algorithm, adding the nodes in a different random order each time. The results for these polymer growth runs are displayed in Fig. 26. The median of the 100 runs was 176.51809563, and the 95% bootstrapped confidence interval for the median was (176.47527585, 176.55376641), all in units of k_BT.

The brute-force value is within in the confidence interval for the polymer growth median, yielding some confidence in the polymer growth approach. Moreover, the polymer growth estimate produces fairly tight bounds for the confidence interval, with the 95% confidence interval spanning only about 0.1 k_BT.

In addition to validating the polymer growth calculation, we can evaluate the performance of belief propagation against both brute-force and polymer growth in the small system. The belief propagation algorithm is deterministic, and yields a value of 176.495544382 k_BT. Remarkably, this estimate is agrees to the brute-force value to six decimal places; as such, it is also within the bounds of the polymer growth estimate.

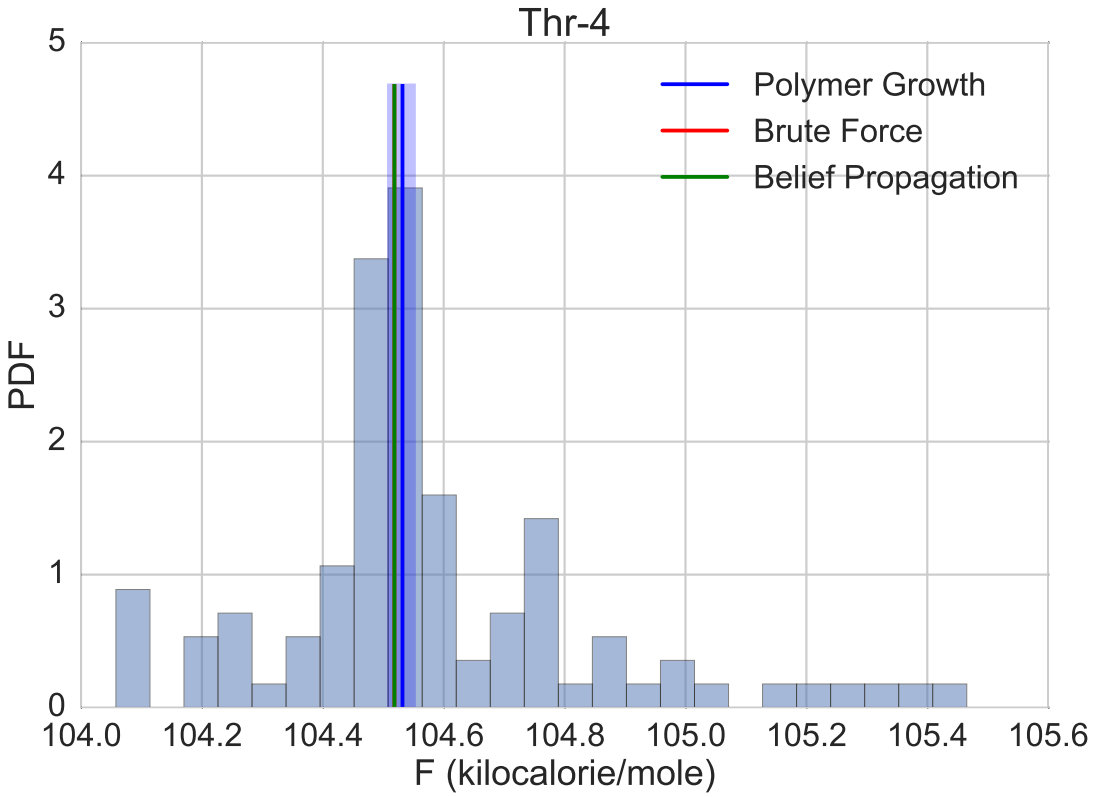

Figure 26: The results of estimating the free energy of the Thr-4 test system using 100 rounds of polymer growth. The median of the polymer growth estimates is shown as a vertical blue line, the brute-force value as a red line, and the belief propagation value as a green line. The brute-force and belief propagation values are close enough that the brute-force value is masked by the belief propagation value. The 95% confidence interval of the polymer growth median is shown as a blue band around the median.

4.6.2 Determining Adequate Sampling Density in a Small Test System

The Threonine-4 peptide is also a useful system for investigating the dependence of the Markov random field free energy estimate upon the sample size used for the nodes and edges. The number of states k per node is a free parameter, and we expect that the free energy estimate will converge to a steady value as $k \to \infty$, just as the value of a Riemann sum converges to the area under a curve as the number of rectangles becomes large. The art of choosing k, then, is finding a large enough value that the free energy estimate has stabilized, but not so large that either constructing the graph or running belief propagation on the graph becomes prohibitively time or memory intensive. Although the choice of k will always be system dependent, it is useful to get a sense for reasonable values of this parameter by using a small system like Threonine-4 that can be sampled systematically. The results of my exploration of state-space are shown in Fig. 27. One fairly striking result from Fig. 27 that is the free energy estimate in this system is largely insensitive to the number of states per methyl-group degree of freedom, as long as that number is greater than one. Another nice result illustrated in the figure is that the free energy estimate seems to converge to a fairly steady value after somewhere around 7-11 states per heavy atom χ-angle degree of freedom.

These numbers are encouraging: a fairly small sample of the each dihedral degree of freedom seems to yield a reasonable estimate for the free energy; prohibitively exhaustive sampling does not appear to be necessary to obtain a reasonably converged result. However, this result should be taken with some healthy skepticism, for a few reasons. The foremost concern is that while each node represented one heavy atom and one methyl-group dihedral degree of freedom, there is no reason to believe that convergence at small sample density in this small system implies convergence in more difficult systems. Another concern is that the values for these free energy estimates were produced using belief propagation. While the previous section demonstrated that belief propagation was impressively accurate in the Threonine-4 system when using 11 states per heavy atom χ-angle dihedral degrees of freedom and 3 states per methyl group dihedral degree of freedom, a skeptic might be concerned that this level of agreement doesn't generalize to other sampling densities. Unfortunately, exploring the parameter space of even this small model with anything other than belief propagation is prohibitively time-intensive. Since these exploratory results are not meant to provide authoritative free energy estimates, but rather give a sense for reasonable starting points in

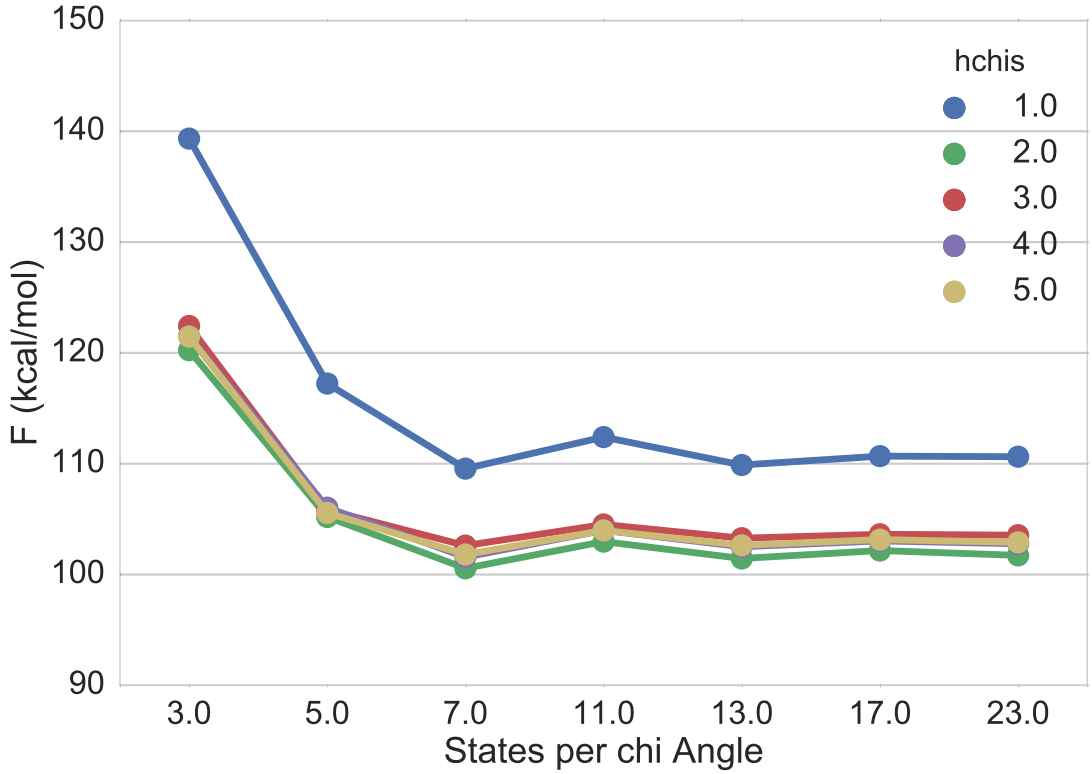

Figure 27: Free energy estimates in Threonine-4, for different numbers of states per degree of freedom. The horizontal axis indexes the number of states per heavy atom chi angle degree of freedom, while the colors correspond to different choices of the number of states per methyl-group dihedral angle degree of freedom ("hchis", for short).

further investigations of more complicated systems, they find their use as a guide the exploration of more complex models in the following section.

4.6.3 Exploring Sampling Density in Larger Test Systems

Exploring a full pairwise grid of sample sizes for each combination of heavy atom and methyl group dihedral angle degrees of freedom is prohibitive in larger systems. Informed by the relative insensitivity of the free energy estimates in the previous section to more than two samples per methyl group degree of freedom, I explored primarily along the heavy atom dihedral degrees of freedom. I studied ten more peptides in order to assess the effect of both peptide length and side-chain size on the convergence of the energy and entropy estimates. Specifically, I examined capped peptides consisting of four or eight identical amino acids (either Alanine, Threonine, Valine, Leucine, or Tyrosine), after allowing them to relax for 1.0 nanoseconds of molecular dynamics. For each peptide, I constructed a Markov random fields at different sampling densities. The notation I employ of (m, n) indicates the number of samples per heavy atom and methyl group dihedral, respectively. The results of these studies are presented in the following figures, with the total free energy of the Markov random field broken down into the energetic and entropic contributions, i.e. $F = \langle U \rangle - TS$.

It is important to note that the convergence of the free energy estimates based on the number of samples per node in the graph will always be system dependent, so the figures depicting the convergence (or lack thereof) of these estimates for the test systems must be taken as largely exploratory, and not an authoritative assessment of adequate sample size. Nonetheless, some broad trends are visible in the data. The first trend is that the energetic contribution to the free energy dominates the entropic contribution (at 298 K). This is sensible, as the backbone is kept fixed in these studies, freezing out otherwise important contributions to the entropy (a justification for doing so might be that in larger protein structures, the backbone is relatively stable, though of course further quantification of the effects of backbone flexibility on these estimates is desirable). Another trend visible in the data is that the estimate of the average energy seems to stabilize more quickly than the estimate of the entropy, at least in relative terms. Finally, the convergence of the entropy estimate seems to be worse for the peptides the larger they are, and the larger their

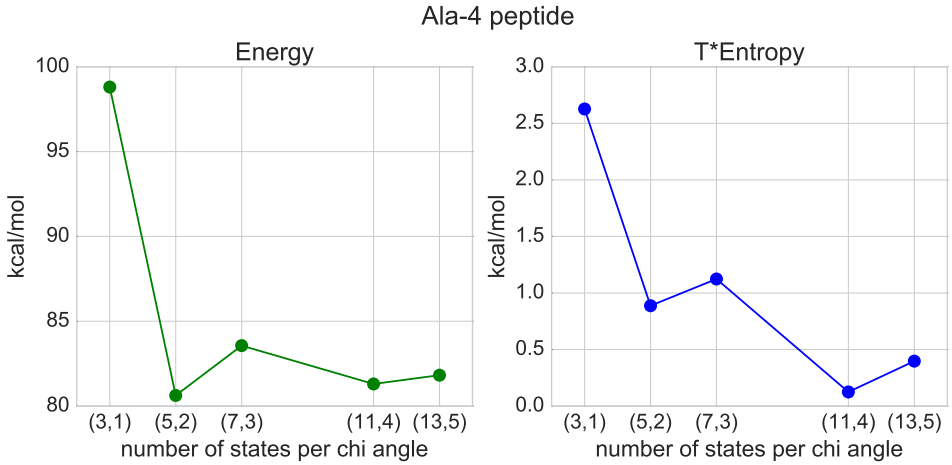

(a) Alanine-4

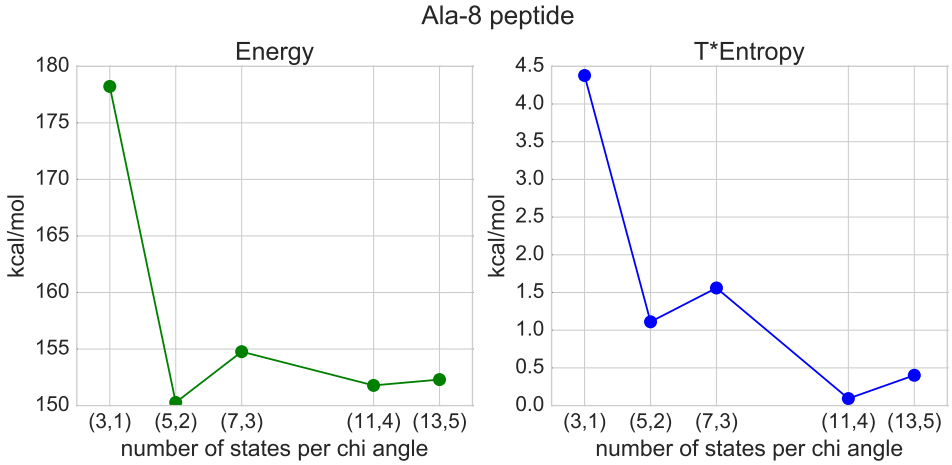

(b) Alanine-8

Figure 28: Belief propagation estimates of the free energy for Alanine-4 Alanine-8 at different sampling densities, broken down into the energetic and entropic contributions. The indices for the heavy atom χ-angle sampling density are irrelevant, as neither Alanine nor the methyl caps possess any. As the number of states per methyl group dihedral degree of freedom increases from one to five, both the energy and entropy estimates converge to a stable value ($\pm$ $\sim$1 kcal/mol).

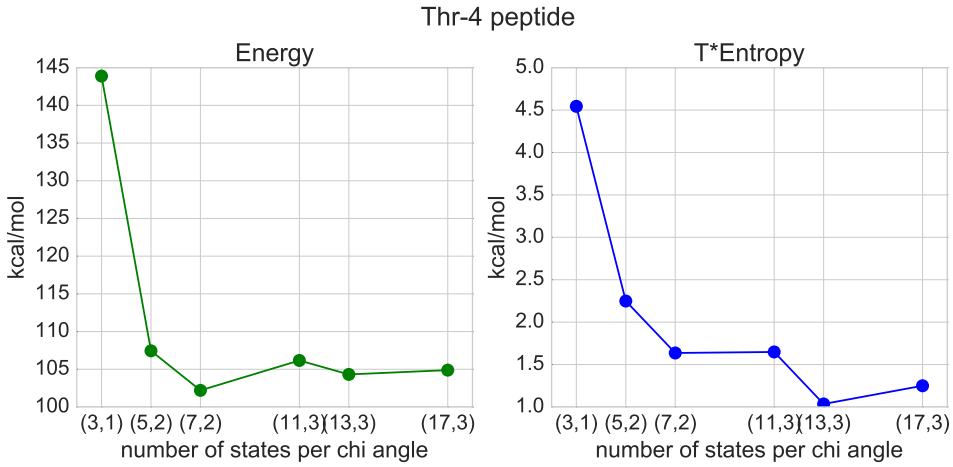

(a) Threonine-4

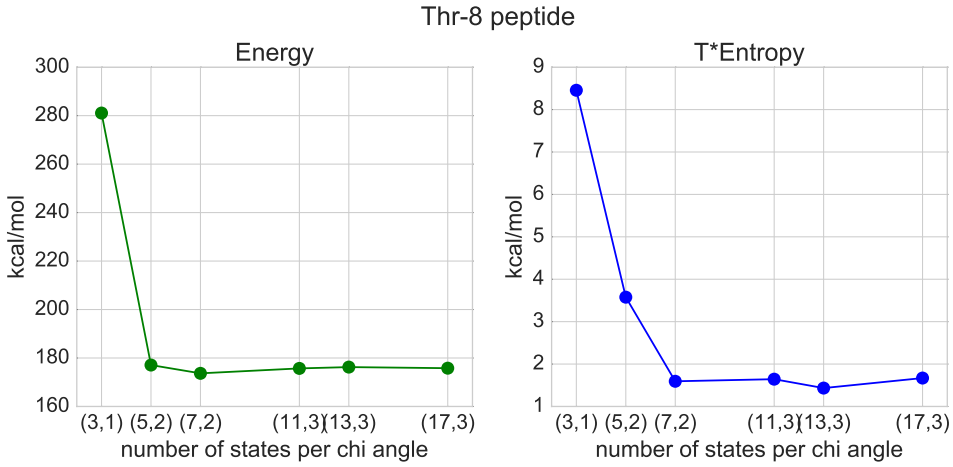

(b) Threonine-8

Figure 29: Belief propagation estimates of the free energy for Threonine-4 and Threonine-8 at different sampling densities, broken down into the energetic and entropic contributions. As the number of states per heavy atom χ-angle and methyl group dihedral degree of freedom increase together, both the energy and entropy estimates seem to converge to a stable value ($\pm$ $\sim$1 kcal/mol).

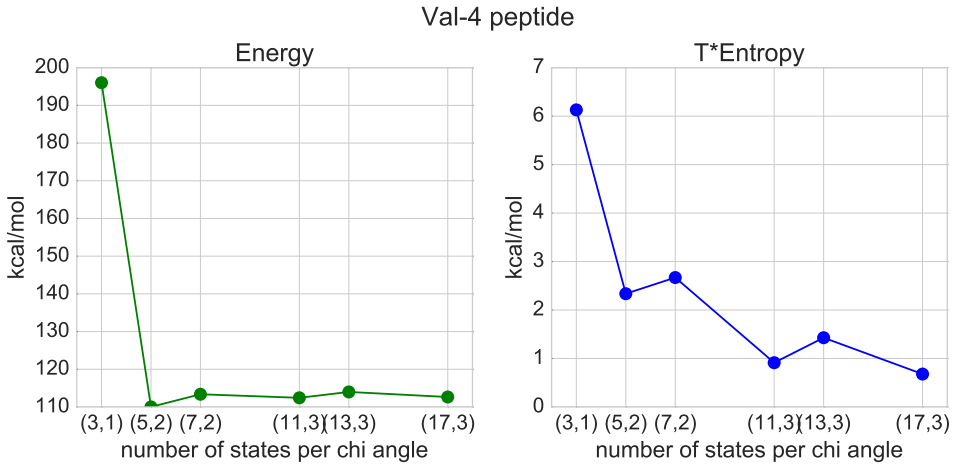

(a) Valine-4

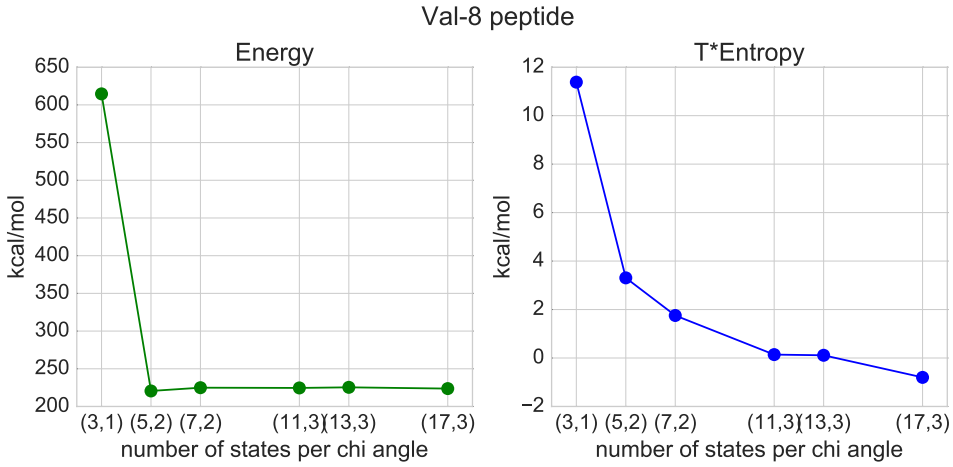

(b) Valine-8

Figure 30: Belief propagation estimates of the free energy for Valine-4 and Valine-8 at different sampling densities, broken down into the energetic and entropic contributions. As the number of states per heavy atom χ-angle and methyl group dihedral degree of freedom increase together, both the energy and entropy estimates seem to converge to a stable value ($\pm$ $\sim$1 kcal/mol).

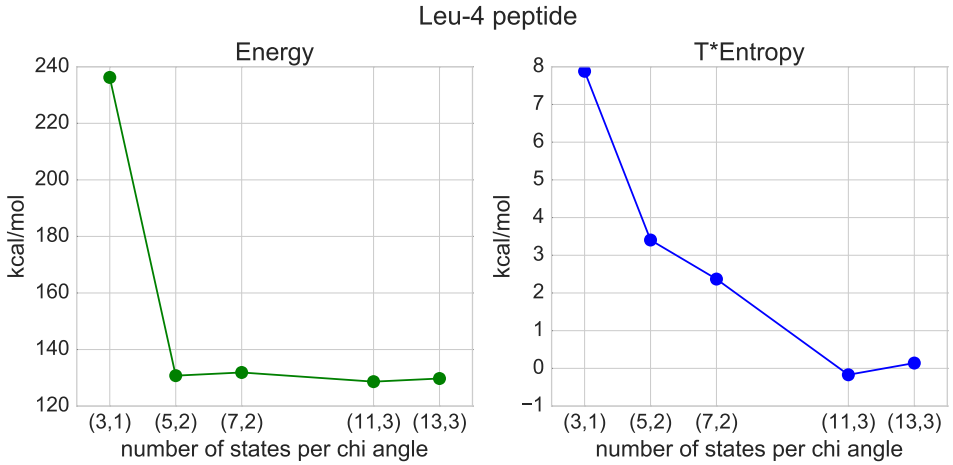

(a) Leucine-4

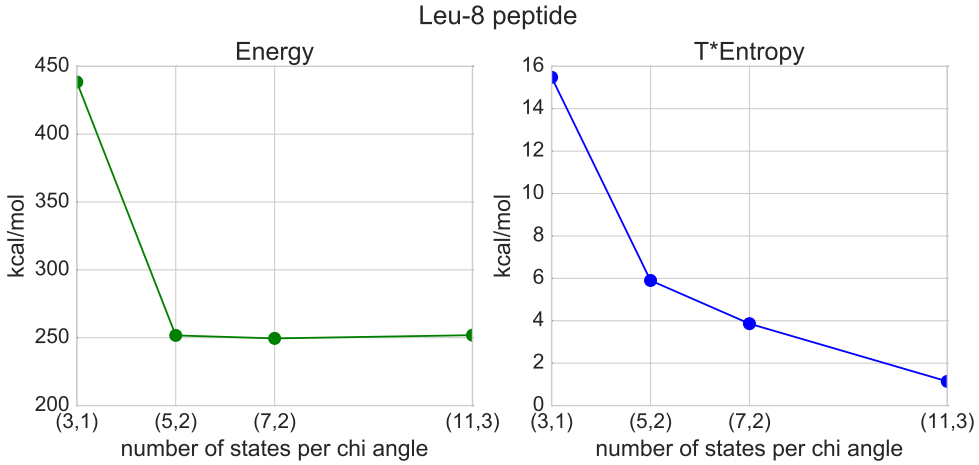

(b) Leucine-8

Figure 31: Belief propagation estimates of the free energy for Leucine-4 and Leucine-8 at different sampling densities, broken down into the energetic and entropic contributions. As the number of states per heavy atom χ-angle and methyl group dihedral degree of freedom increase together, the energy estimates seem to converge to a stable value ($\pm$ ~1 kcal/mol), though the entropy estimates do not display convincing tendencies toward convergence at this level of sampling.

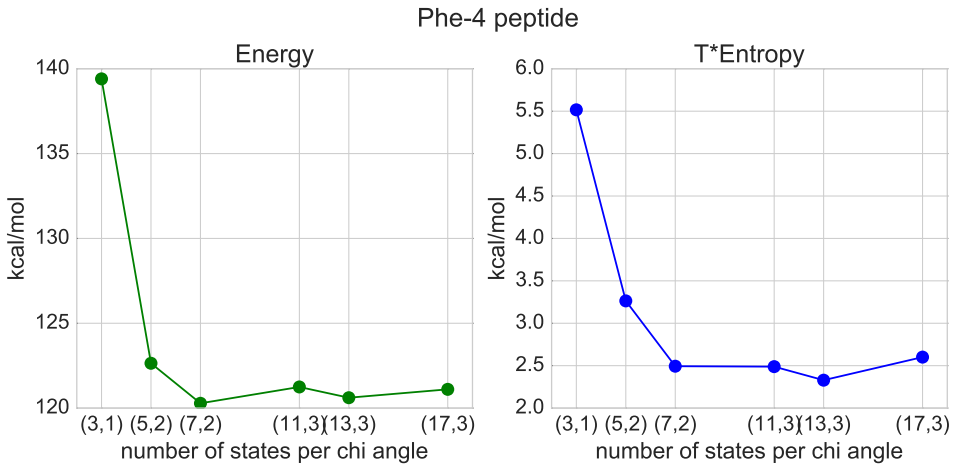

(a) Phenylalanine-4

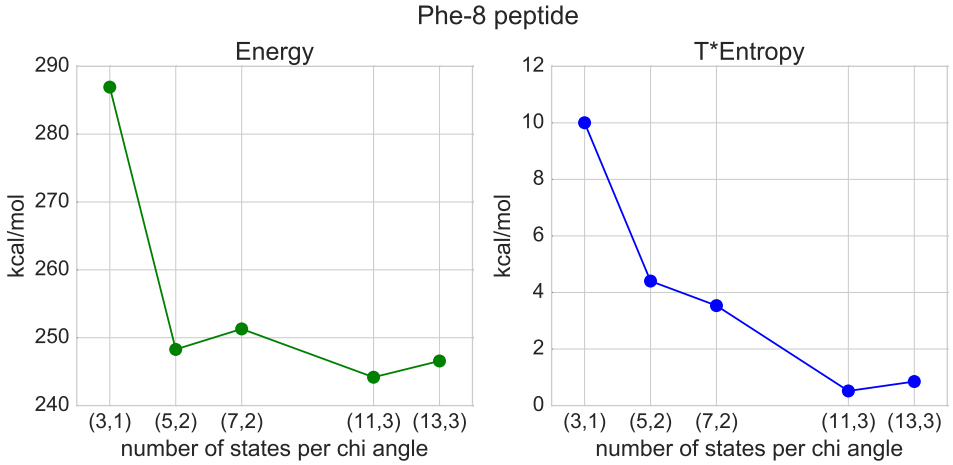

(b) Phenylalanine-8

Figure 32: Belief propagation estimates of the free energy for Phenylalanine-4 and Phenylalanine-8 at different sampling densities, broken down into the energetic and entropic contributions. As the number of states per heavy atom χ-angle and methyl group dihedral degree of freedom increase together, both the energy and entropy estimates seem to converge to a stable value ($\pm$ $\sim$1 kcal/mol), though the convergence of the entropy estimate in Phenylalanine-8 is less than fully convincing.

side-chains are, though the convergence is only indisputably absent for the Leucine-8 system.

These heuristics provide some evidence that sampling at 11 states per heavy atom χ-angle degree of freedom and 2 states per methyl group dihedral degree of freedom might provide a reasonably accurate picture of the physics involved. In turn, this assessment of the Markov random fields permits a reasonable assumption that in larger systems, constructing Markov random fields at this sampling density might provide a realistic setting in which to quantify the performance of the belief propagation against exact methods.

4.6.4 Comparing belief propagation free energies to statistically exact estimates in the binding pocket of a Protein: T4 Lysozyme Mutant

The binding pocket of a cavity-containing mutant of T4 Lysozyme, with the RSCB id of 1L83 [203], provides an ideal system in which to investigate the speed and accuracy of belief propagation in a larger system. 1L83 is composed of 164 amino acids, a significantly larger structure than the small peptides used previously. However, the larger structure, which is conformationally stable, provides a setting in which freezing the backbone when constructing the Markov random field is more reasonable. Eventually, one would want to sample multiple backbone conformations, as in [57], to capture the effects of the backbone degrees of freedom.

The binding pocket of 1L83, where benzene can dock, has 11 amino acids whose α-carbons are within 0.5 nanometers of the benzene position: Ile78, Leu84, Val87, Tyr88, Leu91, Ala99, Val103, Val111, Leu118, Leu121, Phe153. Working in the interior of a protein is a fairly challenging environment in which to find favorable side-chain conformations due to tight packing, a situation largely absent in the peptide systems investigated previously.

In order to tease apart the effects of the side-chain packing on the combinatorics of the state-space of the different side-chains, I created an artificial test system: a peptide composed of the amino acids in the binding pocket. This allowed me to work in a slightly "easier" setting while still exploring parameters relevant to the lysozyme system.

4.6.4.1 Results for Artificial "Binding Pocket" Peptide

The peptide is shown in Fig. 33, and has sequence ACE0,ILE1,VAL2,TYR3,LEU4,ALA5,VAL6,VAL7, LEU8, LEU9, PHE10, NME11.

The careful reader will note that it differs from the binding pocket sequence very slightly, in that it includes two methyl caps, and omits one of the four Leucines in the binding pocket. Nevertheless, the global state-space of the Markov random field is quite similar to that of the binding pocket. Generating the edge potentials for the Markov random field was the bottleneck in investigating this

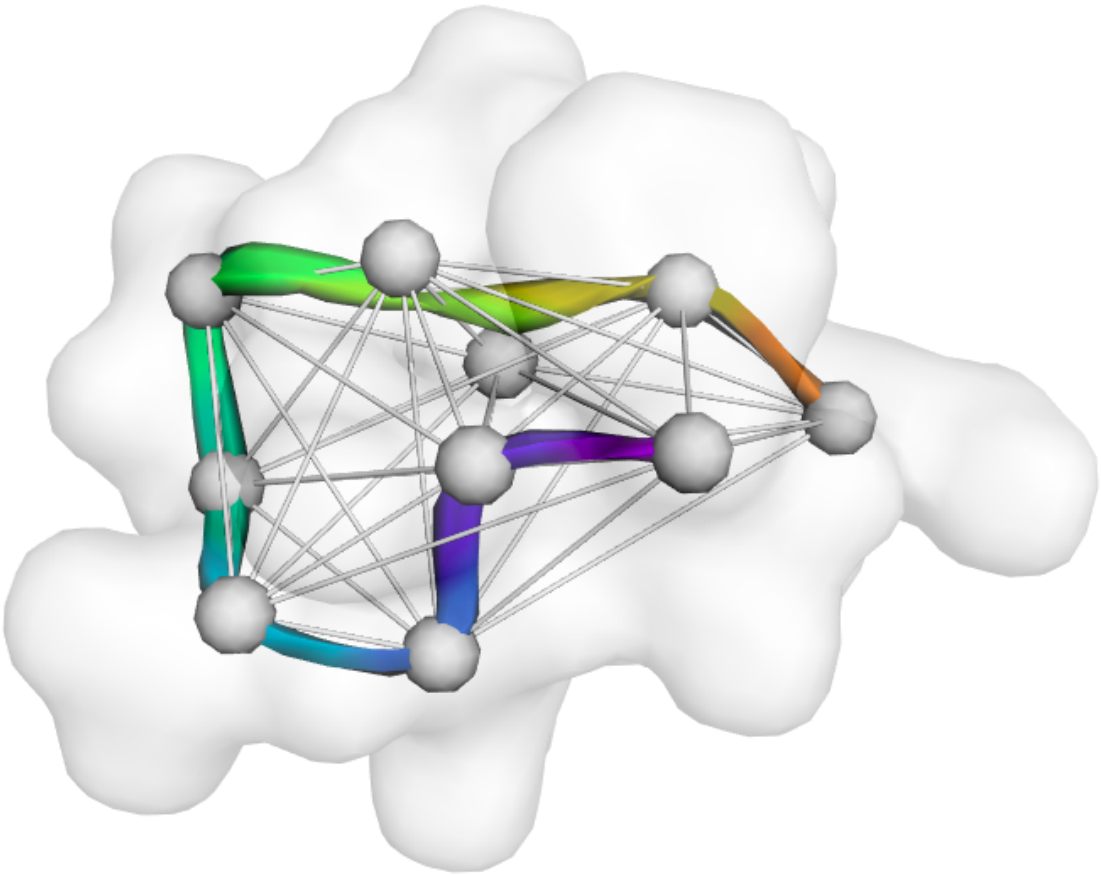

Figure 33: The structure of the binding pocket surrogate peptide. The graph is highly connected, containing 54 out of 66 possible edges.

system: sampled at 11 states per heavy atom χ-angle degree of freedom, and 2 states per methyl group degree of freedom, it took approximately five days to generate the full Markov random field, running in parallel on eight cores.

Since this model is too large for a brute-force computation, the polymer growth sampling algorithm was employed as a bronze standard to which belief propagation results can be compared. The polymer growth algorithm took approximately 12 hours to run 100 replicates in serial, retain-

ing 1000 states per round of growth; for larger or smaller numbers of states kept per round, the run-time scaling is linear.

One difficulty in using the polymer growth approach in a reasonably complex system such as this one is that, as noted in section 4.3.2, polymer growth is systematically biased at finite sample size. Here I keep increasing the number of samples kept per round of growth until the estimates converge, but even at sample sizes that entail a week running polymer growth, the estimate is still changing slightly as the sample size increases. Fortunately, since atomic force fields are not believed to be accurate to much more than $\sim$ 1 kcal/mole ($1 k_B T \approx 0.6$ kcal/mol) [204], and as long as the polymer growth estimate converges to significantly within that tolerance, it can be considered adequate for our purposes.

A last difficulty with the polymer growth algorithm in this system is that at low numbers of samples per round of growth, it often fails to produce any estimate at all. Specifically, the algorithm reaches a dead-end where it can't add any states from a new node that aren't clashes with any of the global configurations from the last round of growth. This is a general difficulty common sequential importance sampling methods such as polymer growth [205]. For instance, when ten states kept per round of growth, only 65 of the 100 polymer growth replicates completed growing the entire structure, though by the time 500 states are kept per round, 99% or greater of the replicates complete the growth process. In calculating the statistics in the figure below, these incomplete runs are omitted, though they do imply that the statistics for the growth runs with smaller numbers of states should be viewed with some skepticism.

The belief propagation free estimates for the entropy and average energy of this system take approximately one second to compute, and they agree with the converged polymer growth estimate to at least $\pm 0.1\ k_B T$. This is a striking indication that similar to previous results using smaller state-spaces [57], peptide or protein graphs large state-spaces pose no difficulties for the belief propagation algorithm. In the next section I will investigate the additional effect of a highly constrained environment in the interior of a protein on the agreement of belief propagation and polymer growth estimates.

4.6.4.2 Results for Lysozyme

While the results for the binding pocket surrogate peptide are encouraging, a more honest evaluation of the accuracy of the belief propagation algorithm in the

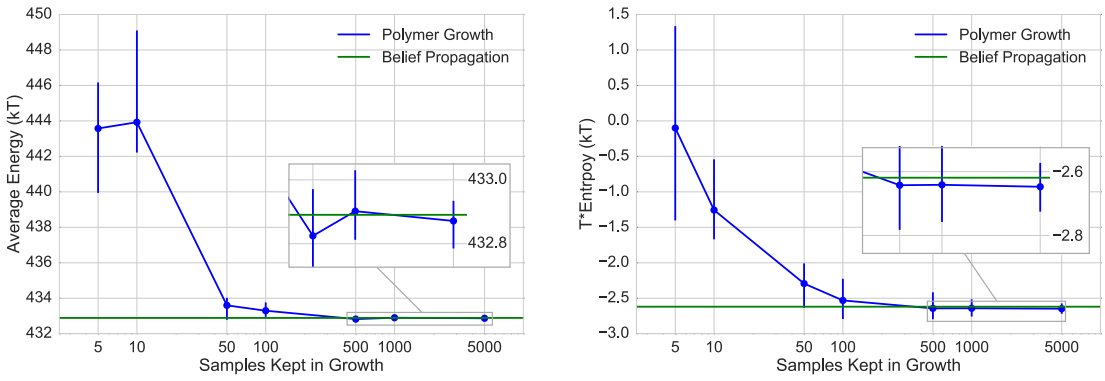

Figure 34: Free energy estimates of the binding pocket surrogate peptide, broken up into the constituent entropy and average energy estimates. The value of the polymer growth estimate converges to within $\pm 0.1\ k_B T$ of the belief propagation value of 435.51 $k_B T$ by the time 500 states per round of growth are kept, with better convergence as the number of states kept per round increases.

context of densely sampled protein structures should involve some explicit difficulty in side-chain positioning, as protein side-chain Side-Chain torsional entropies are known to affect protein ligand interactions [206]. The binding pocket of a mutant lysozyme protein (PDB id 1L83) provides a convenient test-bed in which to evaluate the agreement of belief propagation and exact methods in such a situation. The structure of the lysozyme protein is shown in Fig. 35. The Markov random field for this structure was constructed with a 1.0 nanometer cutoff between the α-carbons of the residues, and used 11 states per heavy atom χ-angle dihedral degree of freedom, and 2 states per methyl group dihedral degree of freedom.

In this initial of study, I restricted the system to a graph containing just the residues in the binding pocket: Ile78, Leu84, Val87, Tyr88, Leu91, Ala99, Val103, Val111, Leu118, Leu121, Phe153. The binding pocket is defined as anything within 0.5 nm of the benzene molecule that is docked in the cavity of the 1L83 crystal structure [203]. The free energy of this system was estimated using both polymer growth and belief propagation, in a process identical to the one described above for the binding pocket surrogate peptide.

In this more realistic environment, the polymer growth algorithm had more difficulty completing the growth process without dead-ending in a set of clash states. With 10 states kept per round of

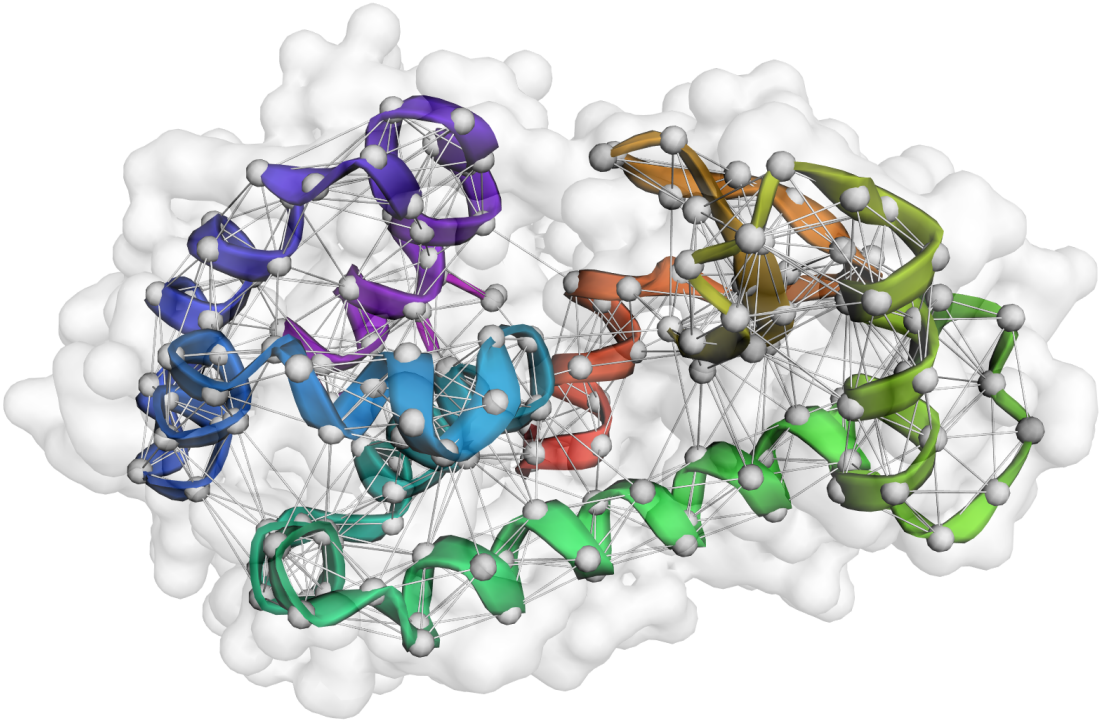

Figure 35: Structure of the Lysozyme mutant used in this study. The binding pocket is between the two domains, at the center of the figure. For clarity, the graph is shown with a 0.8 nanometer cutoff, though in all calculations a 1.0 nanometer cutoff was used, resulting in a denser graph.

growth, only 65% of the 100 replicates completed, increasing to 90% at 500 states kept per round, and 95% at 5000 states per round. Nevertheless, the polymer growth did converge to a reasonably steady result when 500 or more states per round of growth were kept, as shown in Fig. 36. As in the binding pocket peptide calculations, the polymer growth algorithm took approximately 12 hours running in serial to perform 100 replicates of growth, when set to retain 1000 states per round, and the belief propagation algorithm took approximately one second to compute its free energy estimate. Both calculations use the same pre-constructed Markov random field as input, and so the cost of constructing the energy tables in the MRF, which can be considerable, is not included in this run time.

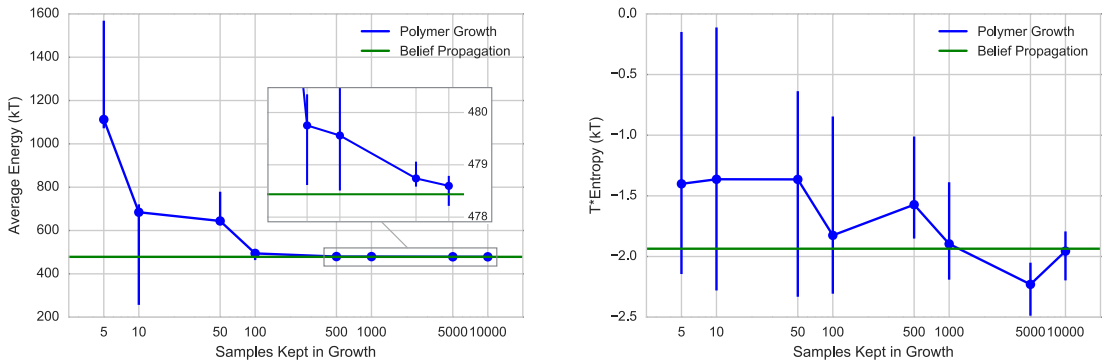

Figure 36: Free energy estimates of the binding pocket of the lysozyme protein, broken up into the constituent entropy and average energy estimates. The value of the polymer growth estimate of the average energy converges to within $\pm 1.0\ k_B T$ of the belief propagation value of 478.4 $k_B T$ using 500 states per round of growth, though the belief propagation value is slightly outside the 95% confidence interval for the estimates until 10,000 states are used per round of growth.

The agreement between polymer growth and belief propagation is more difficult to achieve in this system than in the less tightly constrained peptide surrogate system. The polymer growth algorithm required extensive sampling, necessitating 10,000 states per round of growth in its computation, demanding a week-long run-time for this estimate. At this level of sampling, though, we do see agreement between the polymer growth values and the belief propagation values.

If we take the converged polymer growth estimates to probabilistically bound the exact answer, the margin of error by which belief propagation misses this exact answer is impressively small.

Though the tightness of such bounds is by nature system-dependent, these excellent results for the lysozyme binding pocket are very encouraging, and confirm both the received wisdom that loopy BP is uncannily accurate even when it is not guaranteed to be so [64], and that the Bethe approximation to the free energy for peptides and proteins can be remarkably close to the true free energy [57].

4.6.4.3 ΔF for a Lysozyme Mutant As a last investigation of the effect that sampling density has on free energy estimates, I calculate the change in free energy due to a mutation in the binding pocket of the lysozyme structure. Unlike in the previous section, where I worked with a small subset of the total structure, in this case I incorporate more of the residues to give context to the binding pocket interactions. To do so, I take advantage of the flexibility available in constructing the Markov random field, and include as nodes in the graph all residues which are neighbors of the residues in the binding pocket, but only allow these nodes to take on one state. The nodes in the binding pocket, as before, are sampled with 11 states per heavy atom χ-angle dihedral degree of freedom, and 3 states per methyl group dihedral degree of freedom. This larger Markov random field has the same state-space complexity as the one focused exclusively on the binding pocket, but the extra singleton nodes influence the states that the fully sampled nodes prefer to occupy, removing some of the boundary effects of the previous calculation.

Unfortunately, while the larger MRF posed little difficulty for the belief propagation algorithm, the polymer growth algorithm was not able to sample it due to clashes overwhelming the sampling as the polymer grew, leaving me without a standard against which the performance of belief propagation can be compared for this system. Further work modifying the polymer growth algorithm could perhaps alleviate this issue, but as it stands, these final belief propagation results are presented without any point of comparison, and are of use primarily to illustrate the effect that sampling density has on the BP free energy estimates in a complex calculation.

Fig. 37 shows the belief propagation estimates of the change in free energy of the lysozyme system due to mutating Leucine-111 to a glycine residue, broken up into the constituent changes in entropy and average energy. As the number of samples per dihedral degree of freedom increases, the estimates also continue to change, indicating that not enough samples per degree of freedom have been taken to generate confident estimates of the change in free energy. However, the esti-

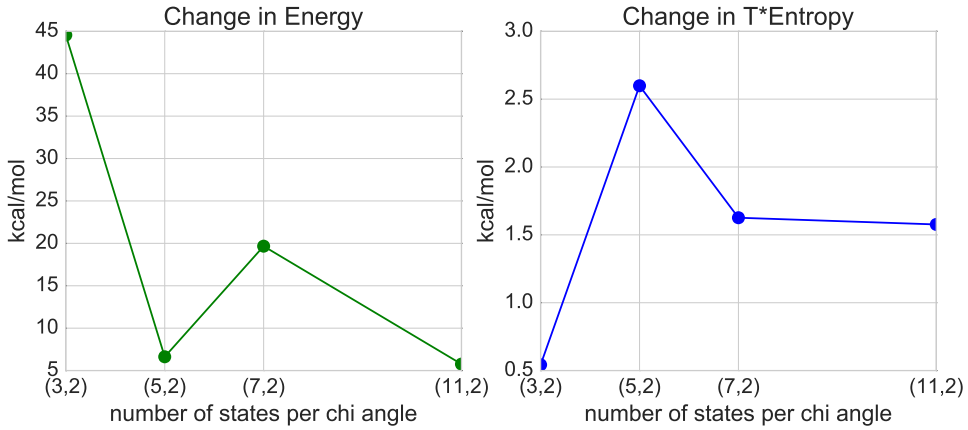

Figure 37: The belief propagation estimate for the change in free energy of the lysozyme structure due to mutating Leucine-111 to a Glycine. The change in free energy is broken down into the change in average energy, and the change in entropy (at 298 K). The computation is performed at four different sampling densities, always with two samples per methyl group dihedral degree of freedom, and between 3 and 11 samples per heavy atom χ-angle dihedral degree of freedom. The fluctuation in the change in average energy computation indicates that more samples are needed in order to reach a realistic estimate. The estimate of the change in entropy displays somewhat better behavior.

mated change in entropy does show some signs of converging, though further sampling would be necessary to confirm this.

4.6.5 Future Work

There are many facets of this work that could be improved or expanded upon. Most practically, the current bottleneck in estimating free energies using Markov random fields is the generation of the Markov random fields themselves. My pipeline uses OpenMM to calculate the interaction energies for the node and edge potentials This library is remarkably flexible, but the Python interface by which I access the energetics information is quite slow compared to state of the art lower-level implementations such as those used in molecular dynamics packages or as implemented in [57]. At the level of sampling used here, this bottleneck is a practical hurdle, not a theoretical one, and there is no reason that implementing a more efficient graph generation pipeline could not result in large speedups in the time expended generating the Markov random fields. Related to speeding up the graph generation process is improving it in quality. The solvent model for the graphs is currently a simple uniform relative dielectric constant of 60.0. While most sophisticated solvent models have difficulty being decomposed into single or pairwise residue components, there is definitely room for improvement in this regard.

Even if generating the Markov random field is not slow enough to be the main bottleneck in the process, at some point the number of states sampled will be too large to hold in memory and perform computations with. This motivates the thought that instead of uniformly sampling states in dihedral space, one could be more be more selective in both generating and retaining samples. States that are explicit clashes and have effectively zero probability of occurring could be pruned away, saving a significant fraction of space. Additionally, one could consider sampling the dihedral degrees of freedom at different densities, depending on their relative importance in generating large conformational changes in the side-chain. That is, the χ_1 angles might be sampled at a higher density that the χ_2 angles, with coarser sampling as one moves down the side-chain. Further reduction in MRF complexity could be achieved by making more extensive use of nodes with singleton, or otherwise severely reduced state-spaces, employed for portions of the structure one has less interest in studying.

More radically, one could consider abandoning uniform sampling, and attempt to use, say, a Boltzmann sampled ensemble of states for the nodes. This approach would require very careful attention to weighting the samples, as it is quite easy to arrive at an incorrect estimate of the partition function when the states account for different proportions of state space. For instance, the logarithmic correction of equation A.24 is no longer entirely accurate, as the states no longer evenly divide up the volume of state space. The advantage to a "hands-off" approach like Boltzmann sampling is appealing though, as it would allow one to include arbitrary degrees of freedom in the samples, and it would be worth investigating.

Lastly, throughout this exploratory work, we have used a fixed backbone in all of the systems. To accurately capture the physics of the system these degrees of freedom need to be incorporated. Drawing samples from a backbone ensemble, and generating graphs for each backbone, as in [57] is an option. Another approach that would account for small flexing motions would be to include in the nodes some amount of flexibility in the backbone degrees of freedom, but not enough to alter the topology of the graph. This would expand the size of the node and edge potentials by a multiplicative factor, so the benefit of doing so would have to be weighed against the cost of generating a larger Markov random field.

4.7 SUMMARY

The goal of this investigation was to explore the performance of belief propagation approximations of the free energy of Markov random fields constructed using the energetic interactions of peptides and proteins, both compared to exact methods on fixed MRFs and in a self-consistent manner as the sampling density of the MRF is increased. In the regime where belief propagation can be compared to an exact brute-force result (small peptides), the belief propagation result agreed with brute-force to a tremendous degree. In larger systems where brute-force approaches fail and a polymer growth estimate must be used as a point of comparison (lysozyme binding pocket and surrogate peptide), the belief propagation estimate is within the fairly tight bounds of the converged polymer growth estimates. In the smaller test systems, it was found that increasing the sampling density to anything above three states per dihedral degree of freedom significantly improved the convergence of the

belief propagation free energy estimates. In larger systems, the situation was more complicated: while BP estimates agreed with polymer growth's exact computations, convergence of the MRFs themselves was unclear, perhaps implying that denser samples are necessary in such situations. In both large and small systems, the belief propagation algorithm takes about a second to compute its estimates, while the brute force and polymer growth estimates take anywhere from hours to days to run. While this is not conclusive proof that belief propagation is always the best method to compute free energies in Markov random fields modeling protein structures, the performance of belief propagation was observed to be impressively accurate compared to exact methods in a nontrivial set of examples.

5.0 CONCLUSIONS

While computational models of biological processes can be incredibly useful tools, unfortunately, most useful models are slow. The unifying theme of this work has been an interest in the expansion of the realm of computationally feasibility in biological simulation. To this end, I have studied two distinct approaches that can be used to more efficiently sample complex biological simulations.

The weighted ensemble methodology is a fairly "hands-off" approach that is agnostic to the nature of the simulation. The efficacy of weighted ensemble sampling in complex models opens the door to integrating genomic-scale data into dynamical systems models. The flexibility of weighted ensemble sampling is also lends itself to simulating models containing processes at different physical scales, and of diverse types. While parameterizing such models will require care, it is no longer unthinkable that it is possible to simulate a stochastic simulation of cell scale processes in detail.

The flexibility of weighted ensemble contrasts strikingly with Markov random fields, which place strong constraints on the structure of the models that can be studied in their formalism. Within their scope, these highly structured models, when coupled with appropriate algorithms, yield otherwise difficult to obtain information at high efficiency. In a way, this is because they are not actually "simulating" anything, in the sense of propagating dynamics. In the creation of the Markov random field, one pre-computes a subset of interactions, and use this cached information to infer the result. Because there are no time-correlations to overcome, as in molecular dynamics, this trade-off of a higher memory footprint for a lower run-time turns out to be immensely beneficial in many cases. It has been known for some time that belief propagation on Markov random fields presents a powerful tool for estimating free energies in bimolecular systems [54, 57]. This present work contributes some small further confirmations of this fact, and presents some evidence that these estimates could be further improved by slightly denser sampling of the side-chain state-space.

While different in nature, both formalisms yield impressive increases in the efficiency of inferring biologically relevant observables. It is hoped that the small gains detailed herein will facilitate the construction of characterization of more detailed and accurate models, and a more comprehensive and integrated study of complex biological systems in general.

APPENDIX A

CORRECTING FOR DISCRETIZATION IN PARTITION FUNCTION ESTIMATES

A.1 DERIVING THE EXACT FORMULA FOR ENTROPY

We start with the standard definition of the free energy:

$$F = \langle E \rangle - TS \implies S/k_B = \beta TS = -\beta F + \beta \langle E \rangle \tag{A.1}$$

$$= \log Z + \langle \beta E \rangle \tag{A.2}$$

$$= \log\left(\hat{Z}/V_0\right) + \langle \beta E \rangle \tag{A.3}$$

where $\beta = 1/k_B T$ is the inverse temperature, and the partition function Z has been decomposed into the configurational partition function $\hat{Z}$ and a volume factor V_0 corresponding to the momentum-space partition function and suitable factors of $\hbar$. The configurational partition function is an integral over all positional degrees of freedom, and as such has dimensions of volume, while the factor V_0, which also has dimensions of volume, makes the quotient $\hat{Z}/V_0$ appropriately dimensionless. This volume factor can further be decomposed into a product of thermal wavelengths, as in [115], but I leave it as an essentially arbitrary fiducial volume whose role is to keep the units of the logarithm correctly dimensionless, since (as we will see) the precise value of V_0 will cancel in any physically relevant calculation, which involves taking a difference of free energies.

We will now focus on the second term in the expression for S/k_B, the expectation of βE. Employing the definition of the normalized probability in terms of the Boltzmann factor of the

energy, we can manipulate the expression to isolate the energy term:

$$\rho(x) = \frac{1}{\hat{Z}} e^{-\beta E(x)} \tag{A.4}$$

$$\iff \beta E(x) = -\log\left(\rho(x)\hat{Z}\right) \tag{A.5}$$

$$= -\log\left(\frac{V_0}{V_0}\rho(x)\hat{Z}\right) \tag{A.6}$$

$$= -\left(\log\left(\hat{Z}/V_0\right) + \log\left(\rho(x)V_0\right)\right) \tag{A.7}$$

where this time I have introduced V_0 entirely artificially, for the sake of keeping the units in the argument of the logarithms dimensionless. Plugging this result into the formal definition of expectation with respect to a probability distribution, over all coordinates x, we have

$$\langle \beta E \rangle = \int_V \rho(x) \beta E(x) dx \tag{A.8}$$

$$= -\int_V \rho(x) \left(\log\left(\hat{Z}/V_0\right) + \log\left(\rho(x)V_0\right)\right) dx \tag{A.9}$$

$$= -\left(\log\left(\hat{Z}/V_0\right) \int_V \rho(x) dx + \int_V \rho(x) \log\left(\rho(x)V_0\right) dx\right) \tag{A.10}$$

$$= -\left(\log\left(\hat{Z}/V_0\right) + \int_V \rho(x) \log\left(\rho(x)V_0\right) dx\right) \tag{A.11}$$

where the first integral in equation A.10 goes to unity by the normalization of $\rho(x)$.

We can now substitute this expression for $\langle \beta E \rangle$ into our original expression for the entropy:

$$S/k_B = \log\left(\hat{Z}/V_0\right) + \langle \beta E \rangle \tag{A.12}$$

$$= \log\left(\hat{Z}/V_0\right) - \left(\log\left(\hat{Z}/V_0\right) + \int_V \rho(x) \log\left(\rho(x)V_0\right) dx\right) \tag{A.13}$$

$$= -\int_V \rho(x) \log\left(\rho(x)V_0\right) dx \tag{A.14}$$

This equation for the entropy is starting to resemble "that awful $\sum p \log p$ formula" [115] formula, but some further manipulations are needed before it's of use in a discretely sampled space.

A.2 DISCRETIZING THE EXACT ENTROPY FORMULA

To discretize the entropy formula so that it is applicable when dealing with a finite number of samples, we approximate it by a Riemann sum:

$$S/k_B = -\int_V \rho(x_i) \log\Big(\rho(x) V_0\Big) dx \tag{A.15}$$

$$\approx -\sum_i^N \rho(x_i) \log\Big(\rho(x) V_0\Big) \Delta x_i \tag{A.16}$$

where the equality holds as $N \to \infty$ and all $\Delta x_i \to 0$. Note that N here is the number of rectangles in the integral, and not the usual statistical mechanics usage of the number of particles in a system.

When using a finite number of samples to represent a distribution, the probability of each sample p_i (that you might get from e.g. a marginal probability in belief propagation) is related to the probability *density* ρ by $p_i = \rho(x_i)\Delta x_i$. That is, the area of a rectangle (in the Riemann sum) is equal to its width times its height. Of course Δx_i here is not just one dimensional, but an arbitrarily dimensioned sub-volume of configuration space. Substituting in, we get

$$S/k_B = -\sum_i^N \left[\left(\frac{p_i}{\Delta x_i}\right) \log\left(\frac{p_i}{\Delta x_i} V_0\right)\right] \Delta x_i \tag{A.17}$$

$$= -\sum_i^N p_i \log\left(\frac{p_i}{\Delta x_i} V_0\right) \tag{A.18}$$

$$= -\sum_i^N p_i \log p_i - \sum_i^N p_i \log \frac{V_0}{\Delta x_i} \tag{A.19}$$

For a uniform discretization, $\Delta x = V/N$, so

$$S/k_B = -\sum_i^N p_i \log p_i - \sum_i^N p_i \log \frac{V_0}{V/N} \tag{A.20}$$

$$= -\sum_i^N p_i \log p_i - \log \frac{V_0}{V/N} \sum_i^N p_i \tag{A.21}$$

$$= -\sum_i^N p_i \log p_i - \log \frac{V_0}{V/N} \tag{A.22}$$

$$= -\sum_i^N p_i \log p_i - \log \frac{N}{V/V_0} \tag{A.23}$$

$$= \boxed{-\sum_i^N p_i \log p_i - \log N + \log V/V_0} \tag{A.24}$$

So we see the logarithmic correction term $(-\log N)$, as used in e.g. [57] for discretizing a continuous system, emerge naturally from a statistical physics treatment of the problem – it's just accounting for bin widths when translating from an integral to a Riemann sum. Lastly, we note that the constant term, $\log V/V_0$, will cancel when computing entropy differences, for example the change in entropy upon binding, even when using entropies computed using a different number of states.

A.3 CORRECTIONS FOR $\hat{Z}$ AND F, BUT NOT E

Similarly, we must correct computations of the configurational partition function $\hat{Z}$ when approximating it using a finite number of samples:

$$\hat{Z} = \int_V e^{-\beta E(x)} dx \tag{A.25}$$

$$\approx \sum_i^N e^{-\beta E(x_i)} \Delta x_i \tag{A.26}$$

where the sum becomes exact in the limit $N \to \infty$ and all $x_i \to 0$. If we use a uniform spatial grid, $\Delta x_i = \Delta x = \frac{V}{N}$ is a constant, and we can factor it out of the sum:

$$\boxed{\hat{Z} = \frac{V}{N} \sum_i^N e^{-\beta E(x_i)}} \tag{A.27}$$

Where again, it is useful to think of $e^{-\beta E(x_i)} \Delta x$ as the area of a box in a Riemann sum.

We can transform into the free-energy picture, using $Z = \hat{Z}/V_0 = e^{-\beta F}$:

$$F = -\frac{1}{\beta} \log\left(\hat{Z}/V_0\right) \tag{A.28}$$

$$= -\frac{1}{\beta} \log\left(\frac{V/V_0}{N} \sum_i^N e^{-\beta E(x_i)}\right) \tag{A.29}$$

$$= -\frac{1}{\beta} \log\left(\sum_i^N e^{-\beta E(x_i)}\right) + \frac{1}{\beta} \log \frac{N}{V/V_0} \tag{A.30}$$

$$= \boxed{-\frac{1}{\beta} \log\left(\sum_i^N e^{-\beta E(x_i)}\right) + \frac{1}{\beta} \log N - \frac{1}{\beta} \log\left(V/V_0\right)} \tag{A.31}$$

and we see the same correction appear here as in the entropy calculation.

It turns out that the average energy formula doesn't need a correction, since the correction terms cancel in a linear average:

$$\langle E \rangle = \frac{1}{\hat{Z}} \int_V E(x) e^{-\beta E(x)} dx \tag{A.32}$$

$$\approx \frac{1}{\hat{Z}} \sum_i^N E(x_i) e^{-\beta E(x_i)} \Delta x \tag{A.33}$$

$$= \frac{1}{\hat{Z}} \frac{V}{N} \sum_i^N E(x_i) e^{-\beta E(x_i)} \tag{A.34}$$

$$= \boxed{\frac{\sum_i^N E(x_i) e^{-\beta E(x_i)}}{\sum_i^N e^{-\beta E(x_i)}}} \tag{A.35}$$

So the only real correction is for the entropy, but when computing the free energy or partition function directly, that same correction must also be included.

The constant term in equations A.24 and A.31 is worth discussing briefly. While the $\log N$ term allows entropy and free energy estimates made using different numbers of samples to be compared to each other, the constant term $\log V/V_0$ renders the overall estimate arbitrary, up to a constant. The value of V in my computations is the volume of configurational space explored in sampling states for the Markov random fields. Since I only explore side-chain dihedral degrees of freedom, this volume is directly proportional to the number of side-chains represented in the MRF. The volume explored for each side-chain dihedral is 2π, so if there are d dihedral degrees of freedom in the graph, $V = (2\pi)^d$. Similarly, if each dihedral in the graph is sampled using k states, then the total number of states is $N = k^d$. Lastly, since V_0 is treated as an arbitrary constant (in some ways similar to the standard 1M concentration needed in calculating binding affinities), we are free to set it to 1 radian, with the foreknowledge that the specific values we assign it will be immaterial in physical calculations. Plugging in these values for the number of states and the volumes, we get

$$-\log N + \log V/V_0 = -\log k^d + \log (2\pi)^d/1 \tag{A.36}$$

$$= -\log \frac{k^d}{(2\pi)^d} \tag{A.37}$$

$$= -d \log \frac{k}{2\pi} \tag{A.38}$$

which is the form of the correction I use, as is equation 4.8.

As a last note, it is worth drawing attention to the negative entropy values that appear at times in the figures in this work. These negative values are solely the result of my choice of 1 radian for V_0, and do not reflect any sort of spooky physics going on. For instance, had I chosen 2π radians instead of one, the entropies would all be positive, but since at the end of the day it is entropy *differences* that matter, the choice of V_0 only affects of the computation by way of numerical stability. For this purpose, any number on the order of 2π is adequate.

APPENDIX B

UNIFORM SAMPLING COMPUTES THE CORRECT PARTITION FUNCTION

In constructing a Markov random field to approximate the free energies of biomolecules, there is considerable freedom in choosing the state space of the model. An immediate simplification is to only consider dihedral degrees of freedom in the side-chains of the amino acids, which is what I have done in this work. In analyzing the correctness of partition function (or equivalently, free energy) computations, it is simplest to ignore belief propagation or polymer growth or other particular algorithms, and focus instead on brute-force computation, since all three converge on the same answer, but brute-force is the simplest to reason about.

In fact, the simplest non-trivial model system to analyze is a graph with just one node, and hence no edges. This one node graph represents a fixed-backbone peptide with one amino acid, and let us further assume that the single side-chain has only one dihedral angle degree of freedom. To find the free energy of the system, we then need only to apply the continuous analogue of the definition of the partition function in equation 1.2 to our system:

$$Z = \int_0^{2\pi} e^{-\beta E(\theta)} d\theta \tag{B.1}$$

Since there is no Jacobian factor for the dihedral angle, uniform sampling over the state space volume ($V = [0, 2\pi)$) is the proper way to construct the integral. A uniform discretization of this integral yields

$$Z \approx \frac{2\pi}{N} \sum_i^N e^{-\beta E(\theta_i)} \tag{B.2}$$

Now consider the situation from the belief propagation point of view: if the states for the node

are sampled uniformly, and plugged in our Markov random field as usual, this is precisely the (correct) answer we will get.

On the other hand, one might be tempted to sample according to, say, a Boltzmann distribution. In this case, in plugging such states into a Markov random field and treating them as usual, we would get the wrong answer. This is most easily illustrated in the integral formulation, where the effect of the Boltzmann weighting of the states, $\rho(\theta)$, can be seen to induce a sort of double-counting of the weights:

$$\begin{aligned} Z_{\text{wrong}} &= \int_0^{2\pi} e^{-\beta E(\theta)} \rho(\theta) d\theta \\ &= \int_0^{2\pi} e^{-\beta E(\theta)} \frac{e^{-\beta E(\theta)}}{Z(\beta)} d\theta \\ &= \frac{1}{Z(\beta)} \int e^{-2\beta E(\theta)} d\theta \\ &= \frac{Z(2\beta)}{Z(\beta)} \end{aligned}$$

It might be possible to correct for this effect, but the simple approach taken here is to eschew sophisticated sampling techniques and use a uniform sampling of states.

APPENDIX C

CODE EXCERPTS

```
def brute_force_Z(graph):

    all_var_inds = nx.get_node_attributes(graph, 'node_state_indices')
    all_node_pots = nx.get_node_attributes(graph, 'node_potential')
    all_edge_pots = nx.get_edge_attributes(graph, 'edge_potential')

    Z = 0.0
    for global_state in it.product(*all_var_inds.itervalues()):
        z = 0.0

        z_node = 1.0
        for node in graph.nodes_iter():
            z_node *= all_node_pots[node][global_state[node], 0]

        z_edge = 1.0
        for edge in graph.edges_iter():
            n_a, n_b = edge
            z_edge *= all_edge_pots[edge][global_state[n_a]][global_state[n_b]]

        z = z_node * z_edge
        Z += z

    return Z
```

Listing C.1: Brute Force Algorithm

```
def polymer_growth(graph, samples=100):

    # initialize array of delta beta*F values
    delta_betaF = np.zeros(len(g.nodes()))

    # initialize 'polymer': each state is a list, saved_states is a list of lists
    saved_states = [[]]
    saved_ens = [0.0]
```

```
    # successively add each node, calculate delta F, and downsample
    nodes = [n for n in g.nodes_iter()]
    for node in nodes:

        # h is a temp graph with nodes/edges > i removed
        h = g.copy()
        h.remove_nodes_from(nodes[node + 1:])

        new_states = []
        delta_ens = []

        # check all the new states we get by adding in a new node to the old states
        for node_state in h.node[node]['node_state_indices']:
            for i, old_state in enumerate(saved_states):
                new_state = old_state + [node_state]
                new_states.append(new_state)
                new_en = get_betaU_for_state(h, new_state)

                delta_en = new_en - saved_ens[i]
                delta_ens.append(delta_en)

        # compute tthe change in free energy
        delta_betaF[node] = calc_betaF(delta_ens, len(saved_states))

        # downsample according the the boltzmann factor of the change in F
        saved_states = sample_states(new_states, delta_ens, samples=samples)
        saved_ens = [get_betaU_for_state(h, state) for state in saved_states]

    # after all the nodes are added and the graph is rebuilt, compute our stats:
    betaF = np.sum(delta_betaF)
    betaU = np.mean([get_betaU_for_state(h, state) for state in saved_states])
    betaTS = betaU - betaF

    return betaF, betaU, betaTS
```

Listing C.2: Polymer Growth Algorithm

```
def runBP(some_graph, N_BPiters=100, epsilon=1e-12):

  deltas = []
  converged = False

  # initialize all messages as ones
  new_messages, old_messages = initialize_messages(some_graph)

  for N_BPiter in xrange(N_BPiters):
    for node_from in some_graph.nodes_iter():
      for node_to in some_graph.neighbors(node_from):
        nodes_gather = [n for n in some_graph.neighbors(node_from) if n != node_to]

        i, j = node_to, node_from
```

```
        # start out with node potential as message;
        # if no neighbors other than target node, this is what gets passed
        x = copy.deepcopy(some_graph.node[j]['node_potential'])

        # if the node passing the message only has one state, short circuit
        # the message gathering etc, and just pass the 1x1 identity.
        if x.shape == (1,1):
          new_messages[j][i] = np.ones_like(x)

        # if the node has neighbors, other than the receiving node, gather incoming
        # messages to the sending node and ready a new message for the receiving node
        else:
          if nodes_gather:
            for k in nodes_gather:
              x *= old_messages[k][j]  # messages are [from][to]

          # hit node i's info with the ij edge potential and pass to j
          psi_ij = copy.deepcopy(some_graph.edge[i][j]['edge_potential'])
          if j < i:
            psi_ij = psi_ij.T

          # messages are now col vectors
          new_messages[j][i] = psi_ij.dot(x)

          # normalize the new message
          new_messages[j][i] = new_messages[j][i] / np.sum(new_messages[j][i])

    # check for convergence
    delta = compute_delta(old_messages, new_messages, verbose=verbose)
    deltas.append(delta)

    if delta < epsilon:
      converged = True
      break

    # get ready for the next iteration of BP, if needed
    old_messages = copy.deepcopy(new_messages)

  node_beliefs = calculate_node_beliefs(some_graph, new_messages)
  edge_beliefs = calculate_edge_beliefs(some_graph, new_messages)

  return node_beliefs, edge_beliefs, new_messages, converged, deltas
```

Listing C.3: Belief Propagation Algorithm

BIBLIOGRAPHY

[1] Rory M Donovan, Andrew J Sedgewick, James R Faeder, and Daniel M Zuckerman. Efficient stochastic simulation of chemical kinetics networks using a weighted ensemble of trajectories. *The Journal of chemical physics*, 139(11):115105, September 2013.

[2] Manel Esteller. Epigenetics in cancer. *The New England journal of medicine*, 358(11):1148–59, March 2008.

[3] H H McAdams and A Arkin. Stochastic mechanisms in gene expression. *Proceedings of the National Academy of Sciences of the United States of America*, 94(3):814–9, February 1997.

[4] A Arkin, J Ross, and H H McAdams. Stochastic kinetic analysis of developmental pathway bifurcation in phage lambda-infected Escherichia coli cells. *Genetics*, 149(4):1633–48, August 1998.

[5] William J Blake, Mads Kaern, Charles R Cantor, and J J Collins. Noise in eukaryotic gene expression. *Nature*, 422(6932):633–7, April 2003.

[6] Jonathan M Raser and Erin K O'Shea. Control of stochasticity in eukaryotic gene expression. *Science (New York, N.Y.)*, 304(5678):1811–4, June 2004.

[7] Leor S Weinberger, John C Burnett, Jared E Toettcher, Adam P Arkin, and David V Schaffer. Stochastic gene expression in a lentiviral positive-feedback loop: HIV-1 Tat fluctuations drive phenotypic diversity. *Cell*, 122(2):169–82, July 2005.

[8] Murat Acar, Jerome T Mettetal, and Alexander van Oudenaarden. Stochastic switching as a survival strategy in fluctuating environments. *Nature genetics*, 40(4):471–5, April 2008.

[9] Long Cai, Nir Friedman, and X Sunney Xie. Stochastic protein expression in individual cells at the single molecule level. *Nature*, 440(7082):358–62, March 2006.

[10] Michael B Elowitz, Arnold J Levine, Eric D Siggia, and Peter S Swain. Stochastic gene expression in a single cell. *Science*, 297(5584):1183–6, August 2002.

[11] Arjun Raj and Alexander van Oudenaarden. Nature, nurture, or chance: stochastic gene expression and its consequences. *Cell*, 135(2):216–26, October 2008.

[12] Narendra Maheshri and Erin K O'Shea. Living with noisy genes: how cells function reliably with inherent variability in gene expression. *Annual review of biophysics and biomolecular structure*, 36:413–34, January 2007.

[13] Benjamin B Kaufmann and Alexander van Oudenaarden. Stochastic gene expression: from single molecules to the proteome. *Current opinion in genetics & development*, 17(2):107–12, April 2007.

[14] Vahid Shahrezaei and Peter S Swain. The stochastic nature of biochemical networks. *Current opinion in biotechnology*, 19(4):369–74, August 2008.

[15] Arjun Raj and Alexander van Oudenaarden. Single-molecule approaches to stochastic gene expression. *Annual review of biophysics*, 38:255–70, January 2009.

[16] Daniel T Gillespie. Stochastic simulation of chemical kinetics. *Annual review of physical chemistry*, 58:35–55, January 2007.

[17] Darren James Wilkinson. *Stochastic Modelling for Systems Biology, Second Edition*, volume 2011. CRC Press, 2011.

[18] Michael L Blinov, James R Faeder, Byron Goldstein, and William S Hlavacek. BioNetGen: software for rule-based modeling of signal transduction based on the interactions of molecular domains. *Bioinformatics (Oxford, England)*, 20(17):3289–91, November 2004.

[19] Daniel T Gillespie. A general method for numerically simulating the stochastic time evolution of coupled chemical reactions. *Journal of Computational Physics*, 22(4):403–434, December 1976.

[20] Daniel T. Gillespie. Exact stochastic simulation of coupled chemical reactions. *The Journal of Physical Chemistry*, 81(25):2340–2361, December 1977.

[21] Rosalind Allen, Patrick Warren, and Pieter ten Wolde. Sampling Rare Switching Events in Biochemical Networks. *Physical Review Letters*, 94(1):018104–, January 2005.

[22] Wen Zhou, Xinjun Peng, Zhenglou Yan, and Yifei Wang. Accelerated stochastic simulation algorithm for coupled chemical reactions with delays. *Computational biology and chemistry*, 32(4):240–2, August 2008.

[23] Eric Mjolsness, David Orendorff, Philippe Chatelain, and Petros Koumoutsakos. An exact accelerated stochastic simulation algorithm. *The Journal of chemical physics*, 130(14):144110, April 2009.

[24] David D. Jenkins and Gregory D. Peterson. AESS: Accelerated Exact Stochastic Simulation. *Computer Physics Communications*, 182(12):2580–2586, December 2011.

[25] Abhijit Chatterjee, Kapil Mayawala, Jeremy S Edwards, and Dionisios G Vlachos. Time accelerated Monte Carlo simulations of biological networks using the binomial tau-leap method. *Bioinformatics (Oxford, England)*, 21(9):2136–7, May 2005.

[26] Basil Bayati, Philippe Chatelain, and Petros Koumoutsakos. D-leaping: Accelerating stochastic simulation algorithms for reactions with delays. *Journal of Computational Physics*, 228(16):5908–5916, September 2009.

[27] Daniel T. Gillespie and Linda R. Petzold. Improved leap-size selection for accelerated stochastic simulation. *The Journal of Chemical Physics*, 119(16):8229, October 2003.

[28] Haokai Lu and Peng Li. Stochastic projective methods for simulating stiff chemical reacting systems. *Computer Physics Communications*, 183(7):1427–1442, July 2012.

[29] Michael A. Gibson and Jehoshua Bruck. Efficient Exact Stochastic Simulation of Chemical Systems with Many Species and Many Channels. *The Journal of Physical Chemistry A*, 104(9):1876–1889, March 2000.

[30] Hiroyuki Kuwahara and Ivan Mura. An efficient and exact stochastic simulation method to analyze rare events in biochemical systems. *The Journal of chemical physics*, 129(16):165101, October 2008.

[31] Dan T Gillespie, Min Roh, and Linda R Petzold. Refining the weighted stochastic simulation algorithm. *The Journal of chemical physics*, 130(17):174103, May 2009.

[32] Min K Roh, Dan T Gillespie, and Linda R Petzold. State-dependent biasing method for importance sampling in the weighted stochastic simulation algorithm. *The Journal of chemical physics*, 133(17):174106, November 2010.

[33] Bernie J Daigle, Min K Roh, Dan T Gillespie, and Linda R Petzold. Automated estimation of rare event probabilities in biochemical systems. *The Journal of chemical physics*, 134(4):044110, January 2011.

[34] Min K Roh, Bernie J Daigle, Dan T Gillespie, and Linda R Petzold. State-dependent doubly weighted stochastic simulation algorithm for automatic characterization of stochastic biochemical rare events. *The Journal of chemical physics*, 135(23):234108, December 2011.

[35] Rosalind J Allen, Daan Frenkel, and Pieter Rein ten Wolde. Simulating rare events in equilibrium or nonequilibrium stochastic systems. *The Journal of chemical physics*, 124(2):024102, January 2006.

[36] Rosalind J Allen, Daan Frenkel, and Pieter Rein ten Wolde. Forward flux sampling-type schemes for simulating rare events: efficiency analysis. *The Journal of chemical physics*, 124(19):194111, May 2006.

[37] Rosalind J Allen, Chantal Valeriani, and Pieter Rein ten Wolde. Forward flux sampling for rare event simulations. *Journal of physics: Condensed matter*, 21(46):463102, November 2009.

[38] Alex Dickson, Aryeh Warmflash, and Aaron R Dinner. Nonequilibrium umbrella sampling in spaces of many order parameters. *The Journal of chemical physics*, 130(7):074104, February 2009.

[39] Aryeh Warmflash, Prabhakar Bhimalapuram, and Aaron R Dinner. Umbrella sampling for nonequilibrium processes. *The Journal of chemical physics*, 127(15):154112, October 2007.

[40] Daniel M. Zuckerman and Thomas B. Woolf. Dynamic reaction paths and rates through importance-sampled stochastic dynamics. *The Journal of Chemical Physics*, 111(21):9475, December 1999.

[41] Anton K Faradjian and Ron Elber. Computing time scales from reaction coordinates by milestoning. *The Journal of chemical physics*, 120(23):10880–9, June 2004.

[42] Christoph Dellago, Peter G. Bolhuis, FeÌĄlix S. Csajka, and David Chandler. Transition path sampling and the calculation of rate constants. *The Journal of Chemical Physics*, 108(5):1964, February 1998.

[43] Titus S. van Erp, Daniele Moroni, and Peter G. Bolhuis. A novel path sampling method for the calculation of rate constants. *The Journal of Chemical Physics*, 118(17):7762, May 2003.

[44] G A Huber and S Kim. Weighted-ensemble Brownian dynamics simulations for protein association reactions. *Biophysical journal*, 70(1):97–110, January 1996.

[45] Bin W Zhang, David Jasnow, and Daniel M Zuckerman. Efficient and verified simulation of a path ensemble for conformational change in a united-residue model of calmodulin. *Proceedings of the National Academy of Sciences of the United States of America*, 104(46):18043–8, November 2007.

[46] Bin W Zhang, David Jasnow, and Daniel M Zuckerman. The "weighted ensemble" path sampling method is statistically exact for a broad class of stochastic processes and binning procedures. *The Journal of chemical physics*, 132(5):054107, February 2010.

[47] Divesh Bhatt, Bin W Zhang, and Daniel M Zuckerman. Steady-state simulations using weighted ensemble path sampling. *The Journal of chemical physics*, 133(1):014110, July 2010.

[48] Matthew C. Zwier, Joseph W. Kaus, and Lillian T. Chong. Efficient Explicit-Solvent Molecular Dynamics Simulations of Molecular Association Kinetics: Methane/Methane, Na + /Cl âĹŠ , Methane/Benzene, and K + /18-Crown-6 Ether. *Journal of Chemical Theory and Computation*, 7(4):1189–1197, April 2011.

[49] Joshua L Adelman and Michael Grabe. Simulating rare events using a weighted ensemble-based string method. *The Journal of chemical physics*, 138(4):044105, January 2013.

[50] Steven Lettieri, Matthew C. Zwier, Carsen A. Stringer, Ernesto Suarez, Lillian T. Chong, and Daniel M. Zuckerman. Simultaneous computation of dynamical and equilibrium information using a weighted ensemble of trajectories. *e-print*, October 2012.

[51] Matthew C Zwier, Joshua L Adelman, Joseph W Kaus, Adam J Pratt, Kim F Wong, Nicholas B Rego, Ernesto Suárez, Steven Lettieri, David W Wang, Michael Grabe, et al.

Westpa: An interoperable, highly scalable software package for weighted ensemble simulation and analysis. *Journal of chemical theory and computation*, 11(2):800–809, 2015.

[52] Matthew C Zwier and Lillian T Chong. Reaching biological timescales with all-atom molecular dynamics simulations. *Current opinion in pharmacology*, 10(6):745–52, December 2010.

[53] James R Faeder, Michael L Blinov, and William S Hlavacek. Rule-based modeling of biochemical systems with BioNetGen. *Methods in molecular biology*, 500:113–67, January 2009.

[54] H. Kamisetty, E.P. Xing, and C.J. Langmead. Free Energy Estimates of All-atom Protein Structures Using Generalized Belief Propagation. *J. Comp. Bio.*, 15(7):755–766, 2008.

[55] C.J. Kamisetty, H.and Langmead. Conformational Free Energy of Protein Structures: Computing Upper and Lower bounds. In *Proc. Structural Bioinformatics and Computational Biophysics (3DSIG)*, pages 23–24, 2008.

[56] S. Balakrishnan, H. Kamisetty, J.C. Carbonell, S.I. Lee, and Langmead C.J. Learning Generative Models for Protein Fold Families. *Proteins: Structure, Function, and Bioinformatics*, 79(6):1061–1078, 2011.

[57] Hetunandan Kamisetty, Arvind Ramanathan, Chris Bailey-Kellogg, and Christopher James Langmead. Accounting for conformational entropy in predicting binding free energies of protein-protein interactions. *Proteins*, 79(2):444–62, February 2011.

[58] Narges Sharif Razavian, Hetunandan Kamisetty, and Christopher J Langmead. Learning generative models of molecular dynamics. *BMC genomics*, 13 Suppl 1(Suppl 1):S5, January 2012.

[59] Narges Sharif Razavian. Continuous graphical models for static and dynamic distributions: Application to structural biology. *Ph.D. Dissertation, Carnegie Mellon University*, 2013.

[60] Christopher James Langmead. *Generative Models of Conformational Dynamics*, pages 87–105. Springer International Publishing, Cham, 2014.

[61] Hetunandan Kamisetty, Bornika Ghosh, Christopher James Langmead, and Chris Bailey-Kellogg. Learning sequence determinants of protein: Protein interaction specificity with sparse graphical models. *Journal of Computational Biology*, 22(6):474–486, 2015.

[62] Huan-Xiang Zhou and Michael K Gilson. Theory of free energy and entropy in noncovalent binding. *Chemical reviews*, 109(9):4092–4107, 2009.

[63] Michael K Gilson and Huan-Xiang Zhou. Calculation of protein-ligand binding affinities*. *Annual review of biophysics and biomolecular structure*, 36(1):21, 2007.

[64] Kevin P Murphy, Yair Weiss, and Michael I Jordan. Loopy belief propagation for approximate inference: An empirical study. In *Proceedings of the Fifteenth conference on Uncertainty in artificial intelligence*, pages 467–475. Morgan Kaufmann Publishers Inc., 1999.

[65] Sekhar C Tatikonda and Michael I Jordan. Loopy belief propagation and gibbs measures. In *Proceedings of the Eighteenth conference on Uncertainty in artificial intelligence*, pages 493–500. Morgan Kaufmann Publishers Inc., 2002.

[66] Martin J Wainwright, Tommi S Jaakkola, and Alan S Willsky. A new class of upper bounds on the log partition function. *IEEE Transactions on Information Theory*, 51(7):2313–2335, 2005.

[67] Joris M Mooij and Hilbert J Kappen. Sufficient conditions for convergence of the sum–product algorithm. *IEEE Transactions on Information Theory*, 53(12):4422–4437, 2007.

[68] Sekhar C Tatikonda. Convergence of the sum-product algorithm. In *Information Theory Workshop, 2003. Proceedings. 2003 IEEE*, pages 222–225. IEEE, 2003.

[69] Steffen L Lauritzen. *Graphical models*, volume 17. Clarendon Press, 1996.

[70] Michael Irwin Jordan. *Learning in graphical models*, volume 89. Springer Science & Business Media, 1998.

[71] Martin J Wainwright and Michael I Jordan. Graphical models, exponential families, and variational inference. *Foundations and Trends® in Machine Learning*, 1(1-2):1–305, 2008.

[72] Daphne Koller and Nir Friedman. *Probabilistic graphical models: principles and techniques*. MIT press, 2009.

[73] Ross Kindermann and J. Laurie Snell. *Markov Random Fields and Their Applications*, volume 1 of *Contemporary Mathematics*. American Mathematical Society, Providence, Rhode Island, 1980.

[74] J.S. Yedidia, W.T. Freeman, and Y. Weiss. Constructing Free-Energy Approximations and Generalized Belief Propagation Algorithms. *IEEE Transactions on Information Theory*, 51(7):2282–2312, July 2005.

[75] Nils B Becker, Rosalind J Allen, and Pieter Rein ten Wolde. Non-stationary forward flux sampling. *The Journal of chemical physics*, 136(17):174118, May 2012.

[76] Nils B. Becker and Pieter Rein ten Wolde. Rare switching events in non-stationary systems. *e-print*, January 2012.

[77] Ambarish Nag, Michael I Monine, James R Faeder, and Byron Goldstein. Aggregation of membrane proteins by cytosolic cross-linkers: theory and simulation of the LAT-Grb2-SOS1 system. *Biophysical journal*, 96(7):2604–23, April 2009.

[78] Ofer Feinerman, Garrit Jentsch, Karen E Tkach, Jesse W Coward, Matthew M Hathorn, Michael W Sneddon, Thierry Emonet, Kendall A Smith, and Grégoire Altan-Bonnet. Single-cell quantification of IL-2 response by effector and regulatory T cells reveals critical plasticity in immune response. *Molecular systems biology*, 6:437, November 2010.

[79] Haijun Gong, Paolo Zuliani, Anvesh Komuravelli, James R Faeder, and Edmund M Clarke. Analysis and verification of the HMGB1 signaling pathway. *BMC bioinformatics*, 11 Suppl 7:S10, January 2010.

[80] Ty M Thomson, Kirsten R Benjamin, Alan Bush, Tonya Love, David Pincus, Orna Resnekov, Richard C Yu, Andrew Gordon, Alejandro Colman-Lerner, Drew Endy, and Roger Brent. Scaffold number in yeast signaling system sets tradeoff between system output and dynamic range. *Proceedings of the National Academy of Sciences of the United States of America*, 108(50):20265–70, December 2011.

[81] Dipak Barua, William S Hlavacek, and Tomasz Lipniacki. A computational model for early events in B cell antigen receptor signaling: analysis of the roles of Lyn and Fyn. *Journal of immunology*, 189(2):646–58, July 2012.

[82] Terrell L. Hill. *Free Energy Transduction And Biochemical Cycle Kinetics*. Dover Publications, 2004.

[83] Bojan Zagrovic and Vijay Pande. Solvent viscosity dependence of the folding rate of a small protein: distributed computing study. *Journal of computational chemistry*, 24(12):1432–6, September 2003.

[84] Michael Samoilov, Sergey Plyasunov, and Adam P Arkin. Stochastic amplification and signaling in enzymatic futile cycles through noise-induced bistability with oscillations. *Proceedings of the National Academy of Sciences of the United States of America*, 102(7):2310–5, February 2005.

[85] Aryeh Warmflash, David N Adamson, and Aaron R Dinner. How noise statistics impact models of enzyme cycles. *The Journal of chemical physics*, 128(22):225101, June 2008.

[86] Boris N Kholodenko. Cell-signalling dynamics in time and space. *Nature reviews. Molecular cell biology*, 7(3):165–76, March 2006.

[87] Liming Wang and Eduardo D Sontag. On the number of steady states in a multiple futile cycle. *Journal of mathematical biology*, 57(1):29–52, July 2008.

[88] F. Schlögl. Chemical reaction models for non-equilibrium phase transitions. *Zeitschrift für Physik*, 253(2):147–161, April 1972.

[89] Daniel T. Gillespie. *Markov Processes: An Introduction for Physical Scientists*. Gulf Professional Publishing, 1992.

[90] Melissa Vellela and Hong Qian. Stochastic dynamics and non-equilibrium thermodynamics of a bistable chemical system: the Schlögl model revisited. *Journal of the Royal Society, Interface / the Royal Society*, 6(39):925–40, October 2009.

[91] David Roma, Ruadhan O'Flanagan, Andrei Ruckenstein, Anirvan Sengupta, and Ranjan Mukhopadhyay. Optimal path to epigenetic switching. *Physical Review E*, 71(1):011902, January 2005.

[92] Rory Donovan. Supplementary Material.

[93] James R. Faeder, William S. Hlavacek, Ilona Reischl, Michael L. Blinov, Henry Metzger, Antonio Redondo, Carla Wofsy, and Byron Goldstein. Investigation of Early Events in Fc{epsilon}RI-Mediated Signaling Using a Detailed Mathematical Model. *J. Immunol.*, 170(7):3769–3781, April 2003.

[94] Weinan E, Weiqing Ren, and Eric Vanden-Eijnden. Transition pathways in complex systems: Reaction coordinates, isocommittor surfaces, and transition tubes. *Chemical Physics Letters*, 413(1-3):242–247, September 2005.

[95] Peter G Bolhuis, David Chandler, Christoph Dellago, and Phillip L Geissler. Transition path sampling: throwing ropes over rough mountain passes, in the dark. *Annual review of physical chemistry*, 53:291–318, January 2002.

[96] A Sali, E Shakhnovich, and M Karplus. How does a protein fold? *Nature*, 369(6477):248–51, May 1994.

[97] Ken A. Dill and Hue Sun Chan. From Levinthal to pathways to funnels. *Nature Structural Biology*, 4(1):10–19, January 1997.

[98] Divesh Bhatt and Ivet Bahar. An adaptive weighted ensemble procedure for efficient computation of free energies and first passage rates. *The Journal of chemical physics*, 137(10):104101, September 2012.

[99] Daniel M. Zuckerman and Thomas B. Woolf. Transition events in butane simulations: Similarities across models. *The Journal of Chemical Physics*, 116(6):2586, February 2002.

[100] Bin W Zhang, David Jasnow, and Daniel M Zuckerman. Transition-event durations in one-dimensional activated processes. *The Journal of chemical physics*, 126(7):074504, February 2007.

[101] JR Stiles and TM Bartol. Computational neuroscience: Realistic modeling for experimentalists. In E De Schutter, editor, *Computational Neuroscience: Realistic Modeling for Experimentalists*, chapter Monte Carl, pages 87–127. CRC Press, Boca Raton, 2001.

[102] Rex A Kerr, Thomas M Bartol, Boris Kaminsky, Markus Dittrich, Jen-Chien Jack Chang, Scott B Baden, Terrence J Sejnowski, and Joel R Stiles. FAST MONTE CARLO SIMULATION METHODS FOR BIOLOGICAL REACTION-DIFFUSION SYSTEMS IN SOLU-

TION AND ON SURFACES. *SIAM journal on scientific computing*, 30(6):3126, October 2008.

[103] J R Stiles, D Van Helden, T M Bartol, E E Salpeter, and M M Salpeter. Miniature endplate current rise times less than 100 microseconds from improved dual recordings can be modeled with passive acetylcholine diffusion from a synaptic vesicle. *Proceedings of the National Academy of Sciences of the United States of America*, 93(12):5747–52, June 1996.

[104] Steven S Andrews. Spatial and stochastic cellular modeling with the Smoldyn simulator. *Methods in molecular biology*, 804:519–42, January 2012.

[105] Leonard A Harris and Paulette Clancy. A "partitioned leaping" approach for multiscale modeling of chemical reaction dynamics. *The Journal of chemical physics*, 125(14):144107, October 2006.

[106] Tianhai Tian and Kevin Burrage. Binomial leap methods for simulating stochastic chemical kinetics. *The Journal of chemical physics*, 121(21):10356–64, December 2004.

[107] Yang Cao, Daniel T Gillespie, and Linda R Petzold. Efficient step size selection for the tau-leaping simulation method. *The Journal of chemical physics*, 124(4):044109, January 2006.

[108] Daniel T. Gillespie. Approximate accelerated stochastic simulation of chemically reacting systems. *The Journal of Chemical Physics*, 115(4):1716, July 2001.

[109] Ulrich H.E. Hansmann. Parallel tempering algorithm for conformational studies of biological molecules. *Chemical Physics Letters*, 281(1-3):140–150, December 1997.

[110] Yuji Sugita and Yuko Okamoto. Replica-exchange molecular dynamics method for protein folding. *Chemical Physics Letters*, 314(1-2):141–151, November 1999.

[111] David J. Earl and Michael W. Deem. Parallel tempering: Theory, applications, and new perspectives. *Physical Chemistry Chemical Physics*, 7(23):3910, November 2005.

[112] Edmund M. Clarke, Orna Grumberg, and Doron A. Peled. *Model Cheking*. MIT Press, 1999.

[113] Edmund M. Clarke, James R. Faeder, Christopher J. Langmead, Leonard A. Harris, Sumit Kumar Jha, and Axel Legay. Statistical Model Checking in BioLab: Applications to the Automated Analysis of T-Cell Receptor Signaling Pathway. *Computational Methods in Systems Biology*, 5307:231–250, 2008.

[114] Sumit K. Jha, Edmund M. Clarke, Christopher J. Langmead, Axel Legay, Andre Platzer, and Paolo Zuliani. A Bayesian Approach to Model Checking Biological Systems. *Computational Methods in Systems Biology*, 5688:218–234, 2009.

[115] D.M. Zuckerman. *Statistical Physics of Biomolecules: An Introduction*. Taylor & Francis, 2010.

[116] Brian Munsky, Gregor Neuert, and Alexander van Oudenaarden. Using gene expression noise to understand gene regulation. *Science*, 336(6078):183–7, April 2012.

[117] Melanie I Stefan, Thomas M Bartol, Terrence J Sejnowski, and Mary B Kennedy. Multi-state modeling of biomolecules. *PLoS computational biology*, 10(9):e1003844, September 2014.

[118] David E. Shaw, J.P. Grossman, Joseph A. Bank, Brannon Batson, J. Adam Butts, Jack C. Chao, Martin M. Deneroff, Ron O. Dror, Amos Even, Christopher H. Fenton, Anthony Forte, Joseph Gagliardo, Gennette Gill, Brian Greskamp, C. Richard Ho, Douglas J. Ierardi, Lev Iserovich, Jeffrey S. Kuskin, Richard H. Larson, Timothy Layman, Li-Siang Lee, Adam K. Lerer, Chester Li, Daniel Killebrew, Kenneth M. Mackenzie, Shark Yeuk-Hai Mok, Mark A. Moraes, Rolf Mueller, Lawrence J. Nociolo, Jon L. Peticolas, Terry Quan, Daniel Ramot, John K. Salmon, Daniele P. Scarpazza, U. Ben Schafer, Naseer Siddique, Christopher W. Snyder, Jochen Spengler, Ping Tak Peter Tang, Michael Theobald, Horia Toma, Brian Towles, Benjamin Vitale, Stanley C. Wang, and Cliff Young. Anton 2: Raising the Bar for Performance and Programmability in a Special-Purpose Molecular Dynamics Supercomputer. In *SC14: International Conference for High Performance Computing, Networking, Storage and Analysis*, pages 41–53. IEEE, November 2014.

[119] Ron O Dror, Robert M Dirks, J P Grossman, Huafeng Xu, and David E Shaw. Biomolecular simulation: a computational microscope for molecular biology. *Annual review of biophysics*, 41:429–52, January 2012.

[120] Jonathan R Karr, Jayodita C Sanghvi, Derek N Macklin, Miriam V Gutschow, Jared M Jacobs, Benjamin Bolival, Nacyra Assad-Garcia, John I Glass, and Markus W Covert. A whole-cell computational model predicts phenotype from genotype. *Cell*, 150(2):389–401, July 2012.

[121] G.M. Torrie and J.P. Valleau. Nonphysical sampling distributions in Monte Carlo free-energy estimation: Umbrella sampling. *Journal of Computational Physics*, 23(2):187–199, February 1977.

[122] Shankar Kumar, John M. Rosenberg, Djamal Bouzida, Robert H. Swendsen, and Peter A. Kollman. THE weighted histogram analysis method for free-energy calculations on biomolecules. I. The method. *Journal of Computational Chemistry*, 13(8):1011–1021, October 1992.

[123] Giovanni Bussi, Alessandro Laio, and Michele Parrinello. Equilibrium Free Energies from Nonequilibrium Metadynamics. *Physical Review Letters*, 96(9):090601, March 2006.

[124] Daniele Moroni, Titus S. van Erp, and Peter G. Bolhuis. Investigating rare events by transition interface sampling. *Physica A: Statistical Mechanics and its Applications*, 340(1-3):395–401, September 2004.

[125] Robert H. Swendsen and Jian-Sheng Wang. Replica Monte Carlo Simulation of Spin-Glasses. *Physical Review Letters*, 57(21):2607–2609, November 1986.

[126] Edward Lyman, F. Marty Ytreberg, and Daniel M. Zuckerman. Resolution Exchange Simulation. *Physical Review Letters*, 96(2):028105, January 2006.

[127] Harold A Scheraga, Mey Khalili, and Adam Liwo. Protein-folding dynamics: overview of molecular simulation techniques. *Annual review of physical chemistry*, 58:57–83, January 2007.

[128] Daniel M Zuckerman. Equilibrium sampling in biomolecular simulations. *Annual review of biophysics*, 40:41–62, January 2011.

[129] Divesh Bhatt and Daniel M Zuckerman. Heterogeneous path ensembles for conformational transitions in semi-atomistic models of adenylate kinase. *Journal of chemical theory and computation*, 6(11):3527–3539, October 2010.

[130] Ernesto Suárez, Steven Lettieri, Matthew C. Zwier, Carsen A. Stringer, Sundar Raman Subramanian, Lillian T. Chong, and Daniel M. Zuckerman. Simultaneous Computation of Dynamical and Equilibrium Information Using a Weighted Ensemble of Trajectories. *Journal of Chemical Theory and Computation*, 10(7):2658–2667, July 2014.

[131] Markus Dittrich, John M Pattillo, J Darwin King, Soyoun Cho, Joel R Stiles, and Stephen D Meriney. An excess-calcium-binding-site model predicts neurotransmitter release at the neuromuscular junction. *Biophysical journal*, 104(12):2751–63, June 2013.

[132] Michael W Sneddon, James R Faeder, and Thierry Emonet. Efficient modeling, simulation and coarse-graining of biological complexity with NFsim. *Nature methods*, 8(2):177–83, February 2011.

[133] Won-Ki Huh, James V Falvo, Luke C Gerke, Adam S Carroll, Russell W Howson, Jonathan S Weissman, and Erin K O'Shea. Global analysis of protein localization in budding yeast. *Nature*, 425(6959):686–91, October 2003.

[134] Josefine Sprenger, J Lynn Fink, Seetha Karunaratne, Kelly Hanson, Nicholas A Hamilton, and Rohan D Teasdale. LOCATE: a mammalian protein subcellular localization database. *Nucleic acids research*, 36(Database issue):D230–3, January 2008.

[135] L. P. Coelho, J. D. Kangas, A. W. Naik, E. Osuna-Highley, E. Glory-Afshar, M. Fuhrman, R. Simha, P. B. Berget, J. W. Jarvik, and R. F. Murphy. Determining the subcellular location of new proteins from microscope images using local features. *Bioinformatics*, 29(18):2343–2349, July 2013.

[136] Matthew C. Zwier, Joshua Adelman, Joseph W. Kaus, Adam J. Pratt, Kim F. Wong, Nicholas B. Rego, Ernesto Suárez, Steven Lettieri, David W. Wang, Michael Grabe, Daniel M Zuckerman, and Lillian T. Chong. WESTPA: An interoperable, highly scalable software package for weighted ensemble simulation and analysis. *Journal of Chemical Theory and Computation*, 11(2):150113180903008, January 2015.

[137] Justin P. Kinney, Josef Spacek, Thomas M. Bartol, Chandrajit L. Bajaj, Kristen M. Harris, and Terrence J. Sejnowski. Extracellular sheets and tunnels modulate glutamate diffusion in hippocampal neuropil. *Journal of Comparative Neurology*, 521(2):448–464, February 2013.

[138] Annalisa Scimemi and Jeffrey S Diamond. The number and organization of Ca2+ channels in the active zone shapes neurotransmitter release from Schaffer collateral synapses. *The Journal of neuroscience : the official journal of the Society for Neuroscience*, 32(50):18157–76, December 2012.

[139] James P Dilger. Simulation of the kinetics of neuromuscular block: implications for speed of onset. *Anesthesia and analgesia*, 117(4):792–802, October 2013.

[140] Nicola Fameli, Oluseye A Ogunbayo, Cornelis van Breemen, and A Mark Evans. Cytoplasmic nanojunctions between lysosomes and sarcoplasmic reticulum are required for specific calcium signaling. *F1000Research*, 3:93, January 2014.

[141] Benjamin M Regner, Dejan Vučinić, Cristina Domnisoru, Thomas M Bartol, Martin W Hetzer, Daniel M Tartakovsky, and Terrence J Sejnowski. Anomalous diffusion of single particles in cytoplasm. *Biophysical journal*, 104(8):1652–60, April 2013.

[142] Jay S Coggan, Thomas M Bartol, Eduardo Esquenazi, Joel R Stiles, Stephan Lamont, Maryann E Martone, Darwin K Berg, Mark H Ellisman, and Terrence J Sejnowski. Evidence for ectopic neurotransmission at a neuronal synapse. *Science (New York, N.Y.)*, 309(5733):446–51, July 2005.

[143] Thomas M Bartol, Markus Dittrich, and James R Faeder. MCell. In Dieter Jaeger and Ranu Jung, editors, *Encyclopedia of Computational Neuroscience*, pages 1673–1676. Springer, New York, 2015.

[144] Lily A. Chylek, Leonard A. Harris, Chang-Shung Tung, James R. Faeder, Carlos F. Lopez, and William S. Hlavacek. Rule-based modeling: a computational approach for studying biomolecular site dynamics in cell signaling systems. *Wiley Interdisciplinary Reviews: Systems Biology and Medicine*, 6(1):13–36, January 2014.

[145] Ting Zhao and Robert F Murphy. Automated learning of generative models for subcellular location: building blocks for systems biology. *Cytometry*, 71A(12):978–90, December 2007.

[146] Gustavo K. Rohde, Wei Wang, Tao Peng, and Robert F. Murphy. Deformation-based nonlinear dimension reduction: Applications to nuclear morphometry. In *2008 5th IEEE International Symposium on Biomedical Imaging: From Nano to Macro*, pages 500–503. IEEE, May 2008.

[147] Gustavo K Rohde, Alexandre J S Ribeiro, Kris N Dahl, and Robert F Murphy. Deformation-based nuclear morphometry: capturing nuclear shape variation in HeLa cells. *Cytometry*, 73A(4):341–50, April 2008.

[148] Tao Peng, Wei Wang, Gustavo K Rohde, and Robert F Murphy. Instance-Based Generative Biological Shape Modeling. *Proceedings / IEEE International Symposium on Biomedical Imaging: from nano to macro. IEEE International Symposium on Biomedical Imaging*, 5193141:690–693, January 2009.

[149] Aabid Shariff, Robert F Murphy, and Gustavo K Rohde. A generative model of microtubule distributions, and indirect estimation of its parameters from fluorescence microscopy images. *Cytometry*, 77A(5):457–66, May 2010.

[150] Tao Peng and Robert F Murphy. Image-derived, three-dimensional generative models of cellular organization. *Cytometry*, 79A(5):383–91, May 2011.

[151] Taráz E Buck, Jieyue Li, Gustavo K Rohde, and Robert F Murphy. Toward the virtual cell: automated approaches to building models of subcellular organization "learned" from microscopy images. *BioEssays : news and reviews in molecular, cellular and developmental biology*, 34(9):791–9, September 2012.

[152] Jieyue Li, Aabid Shariff, Mikaela Wiking, Emma Lundberg, Gustavo K Rohde, and Robert F Murphy. Estimating microtubule distributions from 2D immunofluorescence microscopy images reveals differences among human cultured cell lines. *PloS one*, 7(11):e50292, January 2012.

[153] Robert F Murphy. CellOrganizer: Image-derived models of subcellular organization and protein distribution. *Methods in cell biology*, 110:179–93, January 2012.

[154] Devin Sullivan, Jose-Juan Tapia, Rohan Arepally, Robert F Murphy, Markus Dittrich, and James R Faeder. Design Automation for Biological Models: A Pipeline that Incorporates Spatial and Molecular Complexity. In *GLSVLSI*, 2015.

[155] SBML-Spatial Working Group. SBML Spatial Processes Specification, 2015.

[156] Leonard a Harris, Justin S. Hogg, and James R. Faeder. Compartmental rule-based modeling of biochemical systems. *Proceedings of the 2009 Winter Simulation Conference (WSC)*, pages 908–919, December 2009.

[157] Judah Folkman and Anne Moscona. Role of cell shape in growth control. *Nature*, 273(5661):345–349, June 1978.

[158] Rowena McBeath, Dana M Pirone, Celeste M Nelson, Kiran Bhadriraju, and Christopher S Chen. Cell Shape, Cytoskeletal Tension, and RhoA Regulate Stem Cell Lineage Commitment. *Developmental Cell*, 6(4):483–495, April 2004.

[159] Viola Vogel and Michael Sheetz. Local force and geometry sensing regulate cell functions. *Nature reviews. Molecular cell biology*, 7(4):265–75, April 2006.

[160] Chris Bakal, John Aach, George Church, and Norbert Perrimon. Quantitative morphological signatures define local signaling networks regulating cell morphology. *Science (New York, N.Y.)*, 316(5832):1753–6, June 2007.

[161] SR Neves, P Tsokas, and A Sarkar. Cell shape and negative links in regulatory motifs together control spatial information flow in signaling networks. *Cell*, 2008.

[162] F. A. Dodge and R. Rahamimoff. Co-operative action of calcium ions in transmitter release at the neuromuscular junction. *The Journal of Physiology*, 193(2):419–432, November 1967.

[163] Boris M Slepchenko, James C Schaff, John H Carson, and Leslie M Loew. Computational cell biology: spatiotemporal simulation of cellular events. *Annual review of biophysics and biomolecular structure*, 31:423–41, January 2002.

[164] Kevin M Franks, Thomas M Bartol, and Terrence J Sejnowski. A Monte Carlo model reveals independent signaling at central glutamatergic synapses. *Biophysical journal*, 83(5):2333–48, November 2002.

[165] Johan Hattne, David Fange, and Johan Elf. Stochastic reaction-diffusion simulation with MesoRD. *Bioinformatics (Oxford, England)*, 21(12):2923–4, July 2005.

[166] Steven S Andrews, Nathan J Addy, Roger Brent, and Adam P Arkin. Detailed simulations of cell biology with Smoldyn 2.1. *PLoS computational biology*, 6(3):e1000705, March 2010.

[167] James P. Dilger. Monte Carlo Simulation of Buffered Diffusion into and out of a Model Synapse. *Biophysical Journal*, 98(6):959–967, March 2010.

[168] Sanghyun Park, Fatemeh Khalili-Araghi, Emad Tajkhorshid, and Klaus Schulten. Free energy calculation from steered molecular dynamics simulations using Jarzynski's equality. *The Journal of chemical physics*, 119(6):3559–3566, 2003.

[169] Hyung-June Woo and Benoît Roux. Calculation of absolute protein–ligand binding free energy from computer simulations. *Proceedings of the National Academy of Sciences of the United States of America*, 102(19):6825–6830, 2005.

[170] Nidhi Singh and Arieh Warshel. Absolute binding free energy calculations: On the accuracy of computational scoring of protein–ligand interactions. *Proteins: Structure, Function, and Bioinformatics*, 78(7):1705–1723, 2010.

[171] Ron O Dror, Robert M Dirks, JP Grossman, Huafeng Xu, and David E Shaw. Biomolecular simulation: a computational microscope for molecular biology. *Annual review of biophysics*, 41:429–452, 2012.

[172] James C Gumbart, Benoît Roux, and Christophe Chipot. Standard binding free energies from computer simulations: What is the best strategy? *Journal of chemical theory and computation*, 9(1):794–802, 2012.

[173] Niels Hansen and Wilfred F Van Gunsteren. Practical aspects of free-energy calculations: A review. *Journal of chemical theory and computation*, 10(7):2632–2647, 2014.

[174] Shashidhar N Rao, U Chandra Singh, Paul A Bash, and Peter A Kollman. Free energy perturbation calculations on binding and catalysis after mutating asn 155 in subtilisin. *Nature*, 328(6130):551–554, 1987.

[175] Hagai Meirovitch. Recent developments in methodologies for calculating the entropy and free energy of biological systems by computer simulation. *Current opinion in structural biology*, 17(2):181–186, 2007.

[176] Devleena Shivakumar, Joshua Williams, Yujie Wu, Wolfgang Damm, John Shelley, and Woody Sherman. Prediction of absolute solvation free energies using molecular dynamics free energy perturbation and the opls force field. *Journal of chemical theory and computation*, 6(5):1509–1519, 2010.

[177] David W. Borhani and David E. Shaw. The future of molecular dynamics simulations in drug discovery. *Journal of Computer-Aided Molecular Design*, 26(1):15–26, 2012.

[178] Christophe Chipot. Frontiers in free-energy calculations of biological systems. *Wiley Interdisciplinary Reviews: Computational Molecular Science*, 4(1):71–89, 2014.

[179] Marcel L Verdonk, Jason C Cole, Michael J Hartshorn, Christopher W Murray, and Richard D Taylor. Improved protein–ligand docking using gold. *Proteins: Structure, Function, and Bioinformatics*, 52(4):609–623, 2003.

[180] Oleg Trott and Arthur J Olson. Autodock vina: improving the speed and accuracy of docking with a new scoring function, efficient optimization, and multithreading. *Journal of computational chemistry*, 31(2):455–461, 2010.

[181] Dik-Lung Ma, Daniel Shiu-Hin Chan, and Chung-Hang Leung. Drug repositioning by structure-based virtual screening. *Chemical Society Reviews*, 42(5):2130–2141, 2013.

[182] G Madhavi Sastry, Matvey Adzhigirey, Tyler Day, Ramakrishna Annabhimoju, and Woody Sherman. Protein and ligand preparation: parameters, protocols, and influence on virtual screening enrichments. *Journal of computer-aided molecular design*, 27(3):221–234, 2013.

[183] Andrew R Leach, Brian K Shoichet, and Catherine E Peishoff. Prediction of protein-ligand interactions. docking and scoring: successes and gaps. *Journal of medicinal chemistry*, 49(20):5851–5855, 2006.

[184] N Moitessier, P Englebienne, D Lee, J Lawandi, and CR Corbeil. Towards the development of universal, fast and highly accurate docking/scoring methods: a long way to go. *British journal of pharmacology*, 153(S1):S7–S26, 2008.

[185] Sheng-You Huang and Xiaoqin Zou. Advances and challenges in protein-ligand docking. *International journal of molecular sciences*, 11(8):3016–3034, 2010.

[186] SF Sousa, AJM Ribeiro, JTS Coimbra, RPP Neves, SA Martins, NSHN Moorthy, PA Fernandes, and MJ Ramos. Protein-ligand docking in the new millennium–a retrospective of 10 years in the field. *Current medicinal chemistry*, 20(18):2296–2314, 2013.

[187] Robert Rentzsch and Bernhard Y Renard. Docking small peptides remains a great challenge: an assessment using autodock vina. *Briefings in bioinformatics*, page bbv008, 2015.

[188] Yu-Chian Chen. Beware of docking! *Trends in pharmacological sciences*, 36(2):78–95, 2015.

[189] Edwin T Jaynes. Information theory and statistical mechanics. *Physical review*, 106(4):620, 1957.

[190] Tom Heskes. Stable fixed points of loopy belief propagation are local minima of the bethe free energy. In *Advances in neural information processing systems*, pages 343–350, 2002.

[191] Alexander T Ihler, John W Fisher, and Alan S Willsky. Message errors in belief propagation. In *Advances in Neural Information Processing Systems*, pages 609–616, 2004.

[192] M.J. Wainwright, T.S. Jaakkola, and A.S. Willsky. A New Class of Upper Bounds on the Log Partition Function. *IEEE Transactions on Information Theory*, 51(7):2313–2335, July 2005.

[193] Adrian A Canutescu, Andrew A Shelenkov, and Roland L Dunbrack. A graph-theory algorithm for rapid protein side-chain prediction. *Protein science : a publication of the Protein Society*, 12(9):2001–14, September 2003.

[194] J André C Weideman. Numerical integration of periodic functions: A few examples. *The American mathematical monthly*, 109(1):21–36, 2002.

[195] Xin Zhang, Artem B Mamonov, and Daniel M Zuckerman. Absolute free energies estimated by combining precalculated molecular fragment libraries. *Journal of computational chemistry*, 30:1680–1691, 2009.

[196] Steven Lettieri, Artem B Mamonov, and Daniel M Zuckerman. Extending Fragment-Based Free Energy Calculations with Library Monte Carlo Simulation. *Journal of Computational Chemistry*, 32:1135–1143, 2010.

[197] Daniel M Zuckerman and Thomas B Woolf. Theory of a systematic computational error in free energy differences. *Physical Review Letters*, 89(18):180602, 2002.

[198] Jonathan S Yedidia, William T Freeman, and Yair Weiss. Understanding belief propagation and its generalizations. *Exploring artificial intelligence in the new millennium*, 8:236–239, 2003.

[199] Judea Pearl. Fusion, propagation, and structuring in belief networks. *Artificial intelligence*, 29(3):241–288, 1986.

[200] Jonathan S Yedidia, William T Freeman, and Yair Weiss. Bethe free energy, kikuchi approximations, and belief propagation algorithms. *Advances in neural information processing systems*, 13, 2001.

[201] Hans A Bethe. Statistical theory of superlattices. *Proceedings of the Royal Society of London. Series A, Mathematical and Physical Sciences*, 150(871):552–575, 1935.

[202] Ryoichi Kikuchi. A theory of cooperative phenomena. *Physical review*, 81(6):988, 1951.

[203] AE Eriksson, WA Baase, JA Wozniak, and BW Matthews. A cavity-containing mutant of t4 lysozyme is stabilized by buried benzene. *Nature*, 355(6358):371–373, 1992.

[204] George A Kaminski, Richard A Friesner, Julian Tirado-Rives, and William L Jorgensen. Evaluation and reparametrization of the opls-aa force field for proteins via comparison with accurate quantum chemical calculations on peptides. *The Journal of Physical Chemistry B*, 105(28):6474–6487, 2001.

[205] Jun S Liu. *Monte Carlo strategies in scientific computing*. Springer Science & Business Media, 2008.

[206] Kateri H DuBay and Phillip L Geissler. Calculation of proteins' total side-chain torsional entropy and its influence on protein–ligand interactions. *Journal of molecular biology*, 391(2):484–497, 2009.